UNIVERSITY OF CALIFORNIA SAN DIEGO

Spatially Resolved Measurement in Fibers with Arbitrary Chromatic Dispersion

A dissertation submitted in partial satisfaction of the
requirements for the degree Doctor of Philosophy
in
Electrical Engineering (Photonics)
by

Yauheni Myslivets

Committee in charge:

Professor Stojan Radic, Chair

Professor Prabhakar R. Bandaru

Professor Olga K. Dudko

Professor Vitaliy Lomakin

Professor Shayan Mookherjea

2010

The Dissertation of Yauheni Myslivets is approved, and it is acceptable in quality and form for publication on microfilm and electronically:

_____

_____

_____

_____

_____

Chair

University of California San Diego

2010

Table of Contents

List of Figures and Tables

Vita

1994-1999 B.S. in Physics, Belarusian State University, Department of Physics.

2005-2010 Ph.D in Photonics, University of California San Diego, Department of Electrical Engineering.

Publications

1. E. Myslivets, N. Alic, J.R. Windmiller, S. Radic, “A New Class of High-Resolution Measurements of Arbitrary-Dispersion Fibers: Localization of Four-Photon Mixing Process”, Journal of Lightwave Technology, Vol. 27, No. 3, pp. 364–375, 2009.
2. P. Kylemark, J. Ren, E. Myslivets, N. Alic, S. Radic, P.A. Andrekson, M. Karlsson, “Impact of Pump Phase-Modulation on the Bit-Error Rate in Fiber-Optical Parametric-Amplifier-Based Systems”, IEEE Photonics Technology Letters, Vol. 19, No. 2, pp. 79−81, 2007.
3. C.-S. Bres, N. Alic, E. Myslivets, S. Radic, “Scalable Multicasting in One-Pump Parametric Amplifier”, Journal of Lightwave Technology, Vol. 27, No. 3, pp. 356–363, 2009.
4. J.M. Boggio, S. Moro, E. Myslivets, J.R. Windmiller, N. Alic, S. Radic, “155-nm Continuous-Wave Two-Pump Parametric Amplification”, IEEE Photonics Technology Letters, Vol. 21, No. 10, pp. 612–614, 2009.
5. S. Moro, E. Myslivets, J.R. Windmiller, N. Alic, J.M. Chavez Boggio, S. Radic, “Synthesis of Equalized Broadband Parametric Gain by Localized Dispersion Mapping”, IEEE Photonics Technology Letters, Vol. 20, No. 23, pp. 1971–1973, 2008.
6. E. Myslivets, N. Alic, J.R. Windmiller, R.M. Jopson, S. Radic, “400-ns Continuously Tunable Delay of 10-Gb/s Intensity Modulated Optical Signal”, IEEE Photonics Technology Letters, Vol. 21, No. 4, pp. 251–253, 2009.
7. E. Myslivets, N. Alic, S. Radic, “Spatially Resolved Measurement in Waveguides With Arbitrary Chromatic Dispersion”, IEEE Photonics Technology Letters, Vol. 20, No. 21, pp. 1793–1795, 2008.
8. N. Alic, J.R. Windmiller, J.B. Coles, S. Moro, E. Myslivets, R.E. Saperstein, J.M. Chavez Boggio, C.-S. Bres, S. Radic, “105-ns Continuously Tunable Delay of 10-Gb/s Optical Signal”, IEEE Photonics Technology Letters, Vol. 20, No. 13, pp. 1187–1189, 2008.
9. R. Jiang, C.-S. Bres, N. Alic, E. Myslivets, S. Radic, “Translation of Gbps Phase-Modulated Optical Signal From Near-Infrared to Visible Band”, Journal of Lightwave Technology, Vol. 26, No. 1, pp. 131–137, 2008.
10. S. Moro, E. Myslivets, N. Alic, J.X. Zhao, A.J. Anderson, J.M. Aparicio, J.B. Coles, J.M. Chavez Boggio, S. Radic, “720-ns Continuously Tunable Parametric Delay of a 10-Gb/s Optical Signal”, IEEE Photonics Technology Letters, 2009.
11. T. Chan, E. Myslivets, J.E. Ford, “2-Dimensional beam steering using dispersive deflectors and wavelength tuning”, Optics Express, Vol. 16, No. 19, pp. 14617–14628, 2008.

12. E. Myslivets, N. Alic, S. Moro, B.P.-P Kuo, R.M. Jopson, C.J. McKinstrie, M. Karlsson, S. Radic, “1.56-μs continuously tunable parametric delay line for a 40-Gb/s signal”, Optics Express, Vol. 17, No. 14, pp. 11958–11964, 2009.
13. N. Alic, R.M. Jopson, J. Ren, E. Myslivets, R. Jiang, A.H. Gnauck, S. Radic, “Impairments in deeply-saturated optical parametric amplifiers for amplitude- and phase-modulated signals”, Optics Express, Vol. 15, No. 14, pp. 8997–9008, 2007.
14. E. Myslivets, C. Lundstrom, J.M. Aparicio, S. Moro, A. Wiberg, C.-S. Bres, N. Alic, P. Andrekson, S. Radic, "Spatial Equalization of Zero Dispersion Wavelength Profiles in Nonlinear Fibers", IEEE Photonics Technology Letters, Vol. 21, No. 24, pp. 1807–1809, 2009.
15. N. Alic, E. Myslivets, S. Moro, B.P.-P. Kuo, R.M. Jopson, C.J. McKinstrie, S. Radic, "Micro-Second Parametric Optical Delays", Journal of Lightwave Technology, Vol. 28, No. 4, pp. 448–455, 2010.
16. E. Myslivets, N. Alic, S. Radic “Strict Localization of Nonlinear Interactions in Optical Fibers by Subsequent Brillouin Amplification and Attenuation”, IEEE Photonics Technology Letters, Vol. 22, No. 3, pp. 170–172, 2010.

Conference Presentations

1. E. Myslivets, N. Alic, T. Nakanishi, T. Okuno, M. Hirano, M Onishi, S. Radic, “High Resolution Measurement of Nearly Dispersionless Fiber by Localized Four Photon Mixing”, OFC 2008, PDP11, 2008.
2. N. Alic, E. Myslivets, S. Moro, B.P.-P. Kuo, R.M. Jopson, C.J. McKinstrie, S. Radic, “1.83-μs wavelength-transparent all-optical delay”, OFC 2009, post-deadline paper, pp. 1–3.
3. S. Moro, E. Myslivets, N. Alic, J.M. Boggio, J.R. Windmiller, J.X. Zhao, A.J. Anderson, S. Radic, “Synthesis of equalized broadband gain in one-pump fiber-optic parametric amplifiers”, OFC 2009.
4. J.M. Chavez Boggio, S. Moro, E. Myslivets, J.R. Windmiller, N. Alic, S. Radic, “Raman-induced gain distortions in double-pumped parametric amplifiers”, OFC 2009, pp. 1–3.
5. N. Alic, E. Myslivets, S. Radic, “1.0 bit/secHz spectral efficiency in single polarization at 2000km with narrowly filtered intensity modulated signals”, IEEE/LEOS Summer Topical Meetings 2008, pp. 237–238.
6. N. Alic, E. Myslivets, J.B. Coles, R.E. Saperstein, J.R. Windmiller, S. Radic, R. Jiang, P. Firth, C. Clarke, “Equalized 42.8 Gb/s transmission based on a 10Gb/s EML transmitter”, ECOC 2007, Session 10.4.
7. R. Jiang, N. Alic, R.E. Saperstein, E. Myslivets, C.J. McKinstrie, S. Radic, Parametric Translation of a Phase-Coded Signal over a Record Spectral Range”, OFC2007, Post-deadline Paper PDP37.
8. C.-S. Bres, N. Alic, E. Myslivets, S. Radic, “1-to-40 Multicasting and Amplification of 40 Gbps Channels in Wideband Parametric Amplifier”, Post-deadline Paper, OFC 2008.
9. E. Myslivets, N. Alic, S. Radic, “Spatially Resolved Measurements in Waveguides with Arbitrary Chromatic Dispersion”, Laser Optics 2008, Saint Petersburg, FrR 3.22.
10. E. Myslivets, N. Alic, S. Radic, "Localized measurement of linear polarization rotation parameters in short optical fibers", 35th European Conference on Optical Communication, 2009. ECOC 2009, pp. 1–2.
11. E. Myslivets, N. Alic, S. Moro, B.P.-P. Kuo, R.M. Jopson, C.J. McKinstrie, A.H. Gnauck, M. Karlsson, S. Radic, "1.56-μs continuously tunable 40-Gb/s parametric delay", 35th European Conference on Optical Communication, 2009. ECOC 2009, pp. 1–2.
12. E. Myslivets, C. Lundström, S. Moro, A.O.J. Wiberg, C.-S. Bres, N. Alic, P.A. Andrekson, S. Radic; “Dispersion Fluctuation Equalization Nonlinear Fibers by Spatially Controlled Tension”, OFC 2010, OTuA5, 2008.

Abstract of the Dissertation

Spatially Resolved Measurement in Fibers with Arbitrary Chromatic Dispersion

by

Yauheni Myslivets

Doctor of Philosophy in Electrical Engineering (Photonics)

University of California San Diego, 2010

Professor Stojan Radic, Chair

In this dissertation, a new class of measuring techniques for non-destructive spatial mapping of fiber physical parameters was developed and experimentally verified. The proposed method is based on selective localization of four-photon mixing (FPM) obtained by power transfer between the counter-colliding pulses and provides at least one order of magnitude increase in spatial resolution over comparable methods.

The technique was applied to retrieve geometrical, dispersive, stress, and birefringent properties of distributed fiber devices with meter-scale spatial resolution. The method is capable of resolving fluctuations in fiber transversal geometry comparable to a silica molecular diameter.

1. Introduction

1.1 Effect of the Dispersion Variations to the Operational Properties of Parametric Devices

The introduction of highly nonlinear fibers (HNLF) has revolutionized optical parametric processing [1-7], allowing the construction of true continuous-wave (CW), high efficiency devices that have no equivalent in near-infrared band. Having unique properties, these fibers are potentially interesting for a number of practical applications.

Firstly, the HNLF can be used as a nonlinear platform to obtain a parametric amplification. The main advantage of such amplifiers over standard erbium doped fiber amplifiers (EDFA) is that the gain can be achieved in *any* optical window by proper selection of the fiber dispersion properties and pump wavelength positioning. The bandwidth of the EDFAs is typically limited by 40 nm whereas the bandwidth of HNLF-based ones could be extended for more than 100 nm [8-9]. The parametric gain and bandwidth can be programmed by controlling the pump powers. As an example, a record, albeit narrow, band 70 dB-gain in CW mode was achieved in [5] using a parametric amplifier pumped by a single 2 W laser. The alternative two-pump configuration provides spectrally flattened parametric gain response [3]. The amplifiers based on nonlinear effects can be operated in phase-sensitive manner achieving the noise figure values below 3 dB in single quadrature [20]. Secondly, the HNLFs are used in

nonlinear mixers and converters utilizing the fact that if a strong pump and a weak signal are injected into the fiber, the new spectral products (idlers) are created and matched in frequency with the input waves. The mixers can be used to copy the information from the original channel to different carriers, or to replicate the input signals for further processing. For example, the single binary-modulated channel was mapped to 40 carriers [10]. The third useful property is that the phase of the created idler is conjugated to a phase of the input signal. This effect can be used to compensate link dispersion without using dispersion compensating modules. If the phase is inverted in the middle of the transmission link, the dispersion is perfectly compensated at the end [11]. This approach can also be used to construct continuously tuned delay lines. The idea of such device is based on signal wavelength translation to a different carrier (or idler) and propagation in a dispersive waveguide. Delay tuning is obtained by changing the wavelength of the created idler resulting in the desired delay [12-15]. For example, a record-to-date delay-bandwidth product of 62,400 for 40 Gbit/s modulated signal was recently achieved in [15].

The different class of the applications is based on the fact that the Kerr nonlinear response is nearly instantaneous [26]. This property can be used in order to reshape signal waveforms by modulated high-power pump. Specifically, the time-domain multiplexed channel can be gated from the nearest channels by a periodic train of narrow pulses [10], or an analog waveform can be sampled by short pulses generated by external mode-locked laser [17, 18]. The last principle is utilized in photonic-based ADC converters [19]. A spectacular parametric device is a fast equivalent-time sampling oscilloscope [18] allowing to capture signals with picosecond duration. The bandwidth

of such device is far beyond the maximum bandwidth provided by state-of-the-art electronics. Finally, the nonlinear fibers can be easily pigtailed and incorporated into fiber optics networks.

The efficiency of the nonlinear processes critically depends on the phase synchronization of the interacting waves and is recognized as classical phase matching requirement. Dispersion of the nonlinear media causes phase de-synchronization and defines the dependence of the group propagation index as a function of signal wavelength. The typical HNLF characteristics include nearly 10-100 times lower dispersion and at least 10 times larger nonlinear mode index γ than those of conventional single mode fibers (SMF) at standard telecommunication band [22-24]. The precise phase matching in HNLF can be achieved by proper alignment of the signal wavelength relatively to zero dispersion wavelength (ZDW).

The fibers have lower nonlinear coefficient than that of nonlinear crystalline platforms [26]. However, the phase-matched interaction in HNLF can take place over hundreds of meters and have efficiencies exceeding 40 dB. Unfortunately, the microscopic variations in transverse geometry lead to spatially localized dispersion fluctuations. As a result, the phase matching condition varies along the fiber length. This effect is identified as the fundamental obstacle in the construction of wideband parametric devices [28-30].

Recent fabrication advances have reduced transverse HNLF variations to multiples of the SiO_2 molecular ring diameter [24]. The ratio between transverse HNLF dimension fluctuation and its longitudinal scale reaches the value of 10^{-12}, making the HNLF one the most precisely fabricated structures in modern engineering. To match this

ratio, a typical 100-μm-long monolithic waveguide would have to have a transverse tolerance smaller than the diameter of a single atomic nucleus. The remarkable control of the HNLF cross section variances makes further tightening of the fabrication process a difficult proposition, suggesting a need for alternative means for phase matching control over long fiber lengths.

Fig. 1 demonstrates the simulated gain spectra [30] of the two-pump parametric amplifier with 100-m pump separation for a hundred randomly generated spatial ZDW profiles with fixed mean and standard deviation $\sigma_\lambda = 1$ nm. It is clearly seen that only the certain number of realizations provides high spectrally equalized gain. This demonstration implies that by randomly selecting the HNLF sample from a long coil with known 1-nm deviation of ZDW, there is extremely low probability for construction of wideband spectrally equalized amplifier or converter.

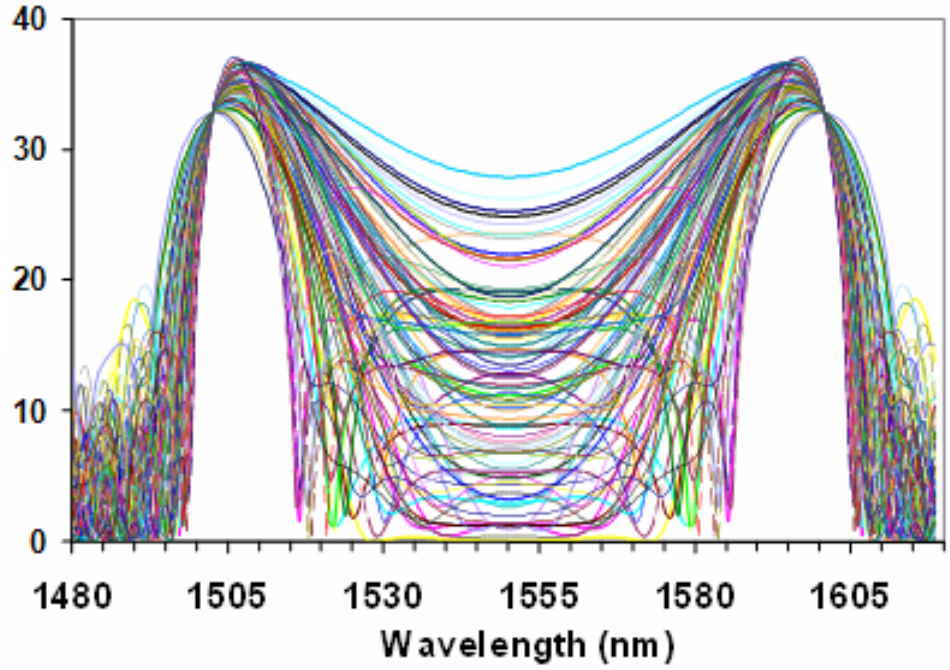

Fig. 1: Simulated gain spectra of the two-pump parametric amplifier. Each trace corresponds to the random realization of the fiber dispersion profile with standard deviation σ_λ = 1 nm. 100 realizations.

In order to quantify the sensitivity of the ZDW to the variations of the waveguide geometry, the mode propagation index n_{eff} was calculated using the transversal refractive index profile $n(r)$ provided by a manufacturer. The dispersion characteristics were obtained by differentiating a phase factor $\beta = n_{\text{eff}} \cdot k_0$ ($k_0 = 2\pi/\lambda$ is an absolute value of propagation coefficient in vacuum). The typical HNLF $n(r)$-profile contains highly GeO_2-doped core (>2%) and depressed fluorine-doped cladding [23, 24]. The details of the used mode calculation algorithm are provided in chapter 4.7. The dispersion characteristics were calculated for the original refractive index profile (center line in Fig. 2). Subsequently, the geometry was changed in both directions by ±1% while keeping refractive index fixed.

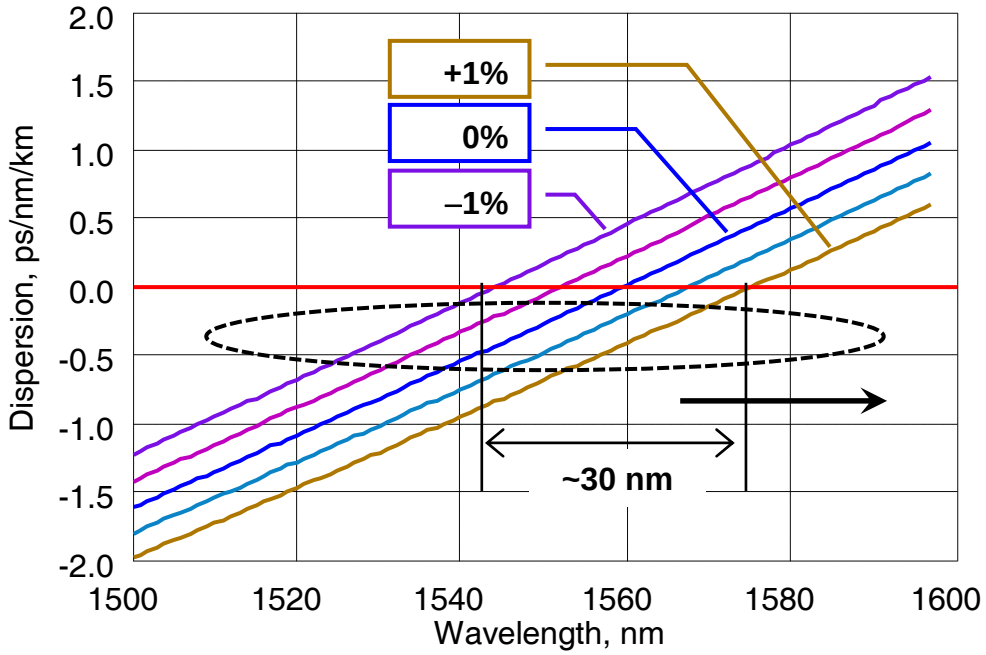

Fig. 2: HNLF chromatic dispersion sensitivity to transversal profile perturbation. Reference (unperturbed) waveguide designed for $\lambda_0 = 1560$ nm; the core radius perturbed by ±0.5% and ±1%.

Fig. 2 demonstrates that the 1% perturbation is translated to the variation of the ZDW by ±15 nm. As shown previously, in order to construct 100-nm-bandwidth parametric amplifier, the accepted variations should be below 1 nm, corresponding to 0.07% variations of the waveguide transverse geometry. The typical mode radius of the HNLF is approximately 1.8 um so that the variations should be below 1.8 nm which is comparable with characteristic 1-nm-dimension of the silica molecular rings shown in Fig. 3 [24].

Rather than insisting on unphysical fabrication tolerances, wideband parametric synthesis can be achieved by obtaining an *exact* HNLF dispersion fluctuation map which can be subsequently used to either select specific waveguide sections, or concatenate fiber segments. Unfortunately, the magnitude of these fluctuations is well below the sensitivity and spatial resolution of existing dispersion measurement techniques [32-39].

Conventional techniques are characterized by sub-km spatial resolution and are designed to analyze fiber types such as conventional single mode fiber (SMF) or non-zero dispersion shifted fiber (NZ-DSF) that possess high chromatic dispersion. In contrast, wideband parametric synthesis requires ***meter-scale*** longitudinal spatial resolution in nearly dispersionless fiber such as HNLF.

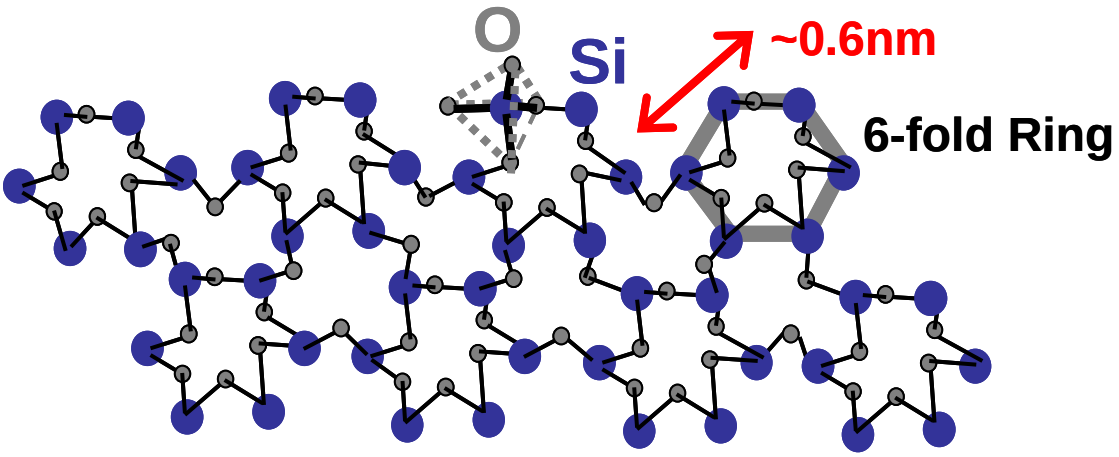

Fig. 3: Molecular structure of silica (SiO_2) glass.

This thesis describes a new class of dispersive measurements based on strict localization of four-photon mixing (FPM) with the main application of dispersion measurement in HNLFs. The FPM localization is achieved by counter-colliding power delivery to a weak probe pulse and is used for high resolution dispersion retrieval along the fiber length. The dispersion fluctuation map was validated by destructive HNLF characterization and mixer response measurements.

This text is organized as follows: chapter 1 briefly describes the ZDW fluctuations, their origin, and existing methods used in order to characterize these fluctuations. In chapter 2, the new localization concept and physical mechanism of the counter-colliding power delivery are introduced, as well as the application of this method

to measure ZDW fluctuations. Chapter 3 concentrates on the experimental construction of a counter-colliding Brillouin scanner and practical measurement requirements. The numerical algorithms and physics of the inverse dispersion solver are presented in chapter 4 and 5. These chapters also describe the validation of the measuring technique for low-dispersion characterization of HNLF samples. In chapter 6, a problem of polarization gain dependence is resolved using a polarization locking scheme. In the last part of the thesis, a chapter 7, the further applications based on the new localization method are demonstrated.

Several distinct methods for processing of the observables obtained by counter-colliding dispersion measuring technique are presented. The validity these methods are verified the by solving inverse problem for experimentally obtained and numerically generated profiles and ultimately proven in practical devices.

1.2 Overview of the Existing Methods for Dispersion Measurements

Intense propagating waves modify refractive index of the nonlinear media causing the transfer of energy among participating frequencies. In optical fibers possessing third order nonlinearity, two propagating waves beat creating a moving periodic pattern by modulating the refractive index. The third wave scatters on this grating and transfers energy to the forth wave. This process is known as four wave mixing (FWM) [40]. In order to provide an effective power transferring process, the phases of four interacting waves should be synchronized. As an illustration, if the phases of the index grating, scattered and generated waves are matched, the power of the later wave will grow. Conversely, if they are out of phase, the energy can be transferred back and forth

mapping the phase mismatch factor along the waveguide coordinates [40]. This inherent property of nonlinear interaction efficiency can be used to acquire the spatially resolved dispersion.

Most sensitive methods for spatially resolved dispersion characterization are based on observing of evolution of generated FWM sidebands or measuring the nonlinear conversion efficiency. Roughly, all algorithms can be divided into two main groups. For the algorithms from the first group, the spatial localization is achieved physically, i.e. the processed signal quantity is extracted at selected spatial point, or a physical effect takes place within selected spatial interval. The interval length defines the physical resolution of the method. The characteristic property of the methods of this kind is that the signals in pulsed mode are utilized.

Gordon [37] has introduced an important technique to measure zero-dispersion wavelength of conventional fibers. Two short pulses propagate inside a fiber and generate FWM product as shown in Fig. 4. Co-propagating pulses with widely separated wavelengths $\Delta\lambda$ generate FWM light only within the fiber section in which they spatially overlap. The length of this section is defined by the walk-off length

$$L_W = \frac{\tau}{\Delta\left(1/v_g\right)} = \frac{\tau}{D\Delta\lambda} \tag{1.1}$$

where D is the fiber dispersion, τ is the pulse duration, v_g is the mean group velocity. The time/space synchronization of the pulses must be adjusted so that this overlap occurs at the desired point within the fiber. The ZDW is measured by tuning the wavelength of the pulse and looking for the maximum power of the generated idler. As an illustration, assume that two pulses propagate in fiber with dispersion slope of $S = 0.08$ ps/nm^2/km. If

the wavelength of one pulse exactly coincides with ZDW and the wavelength of the second pulse is shifted by $\Delta\lambda = 50$ nm, after propagation of 1 km, the pulses will be delayed by $\frac{1}{2} \cdot S \cdot \Delta\lambda^2 L = 100$ ps. This means that if both pulses are 100-ps length, the maximal achievable resolution is 1 km. A similar estimation for HNLF fiber with the 0.02 ps/nm^2/km-slope gives the resolution of 4 km, which is significantly longer than typical length of the HNLF samples used in practice. In case of nearly dispersionless fibers, such as HNLF, the walk-off length necessarily diverges ($L_W \sim L$) and the technique fails to provide spatially resolved measurements. This deficiency is easily understood by noting that, for nearly equal group velocities, two co-propagating pulses will never separate in case when launched synchronously. Conversely, if their launch is delayed, the pulses will never overlap within the practical length of the fiber under test. While FPM generation will be maximized in the first case, it can only be used to obtain a *global*, rather than a spatially localized dispersion measurement.

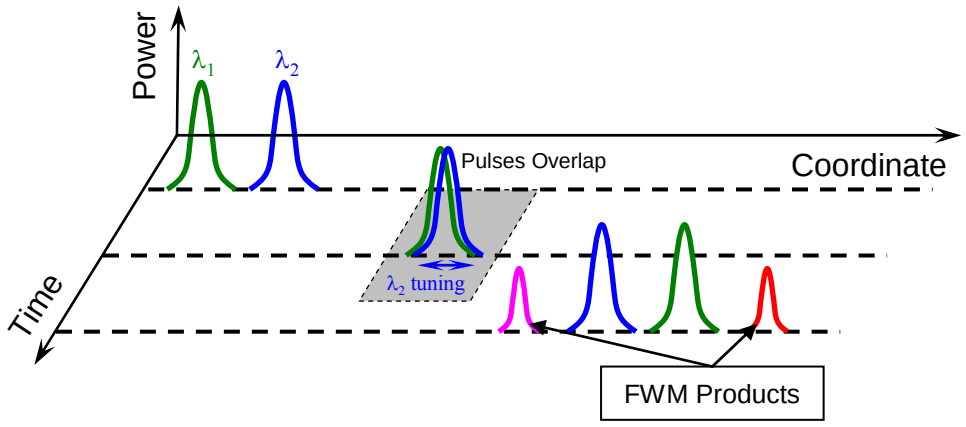

Fig. 4: Schematic representation of Gordon's method.

Mamishev [34] reported OTDR-like measurement technique that retrieves the localized FPM signature using Rayleigh backscattering. Two relatively long (sub-

microsecond) overlapping pulses propagate and generate FWM products. Because of a wave-vector phase mismatch, newly created FWM products oscillate with specific spatial frequency which is measured as a function of distance along the fiber. The oscillations are resolved by observing the temporal variations of the back-reflected light at the fiber input. The spatial frequency f_Z is given by

$$f_z = \frac{1}{\Lambda_z} = cD(\lambda)\left(\frac{\delta\lambda}{\lambda}\right)^2 \tag{1.2}$$

in which c is a speed of light, D is a dispersion coefficient, and $\delta\lambda$ is a wavelength spacing between the signals. The spatial oscillation period defines a resolution of the method. For example, if the pulses with the wavelength separation of 5 nm propagate in standard single mode fiber characterized by 16 ps/nm/km dispersion coefficient, the spatial period is 20 m. In highly nonlinear fibers the corresponding resolved interval is at least ten times longer because the typical dispersion coefficient less than 1 ps/nm/km within C– and L– bands. The spatial resolution can be improved by increasing the wavelength separation between the pulse wavelengths. However, the conversion efficiency drops fast because it is inversely proportional to squared wavevector mismatch Δk^2 [40]. The second difficulty of this method is that the power of the Rayleigh back-reflected light is processed. Considering the typical reflection coefficient for single mode fiber of –80 dB for 1-ns pulses (for 20 cm of propagated distance), the fraction of the reflected light for microsecond pulses is only –50 dB. This means that in order to keep the power of the reflected light 30 dB above quantum limit of –98 dBm for 10 MHz receiver bandwidth, the power of the generated FWM tone should be at least at –18 dBm peak level. Additionally, the physical resolution is limited by long pulse spatial duration

equal to 200 m for 1-us pulses. It is also useful to point out that the Rayleigh scattering itself has a finite bandwidth of several hundreds of MHz.

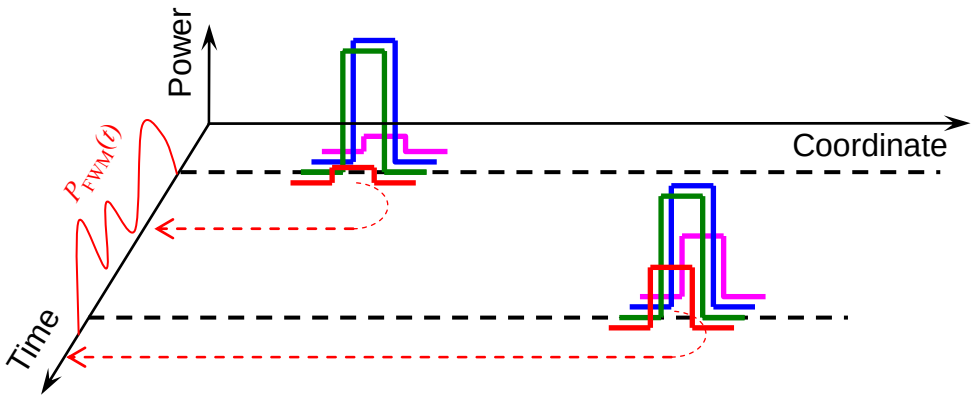

Fig. 5: Schematic representation of Mamishev's method.

Alternatively, the processing of the conversion efficiency [21] profiles corresponding to different positioning in frequency of interacting CW signals is the relevant property of the methods referred to the second group. The dispersion retrieving algorithms are mainly based on Fourier methods for phase reconstruction. The resolution of such methods is defined by sampling bandwidth and is proportional to the range over which one can acquire meaningful data.

Brener [35] has demonstrated a method for the extraction of ZDW variations from measurement of the power of the FWM products created from nonlinear interaction of the two CW signals. The wavelengths λ_1 and λ_2 of the two lasers were tuned keeping the spacing $\Delta\lambda = \lambda_1 - \lambda_2$ fixed. The power of the FWM wave given by

$$I_{\mathrm{FWM}} \propto \left| \int_0^L dz e^{j\phi(z)} e^{-jqz} \right|^2 \tag{1.3}$$

was measured. The variable $q = \kappa\lambda_1$ has a dimension of wavevector, $\kappa = 2\pi c(\Delta\lambda/\lambda_2)^2 S$, S is a fiber dispersion slope, and $\phi(z) = \kappa\int_0^z \lambda_0(z')dz'$ is an accumulated phase mismatch at z. If $\Delta\lambda$ is kept fixed and the ratio $\Delta\lambda/\lambda_2$ is considered as constant, the FWM efficiency is governed by the Fourier transform of the phase function $e^{j\phi(z)}$. The goal is to obtain $\lambda_0(z)$ from measured $I_{FWM}(\lambda)$ by solving the problem known in literature as "phase retrieval problem". González-Herráez [38] has devised a scheme to retrieve $\lambda_0(z)$ using Gerchberg-Saxton algorithm. The spatial resolution of the proposed method can be estimated using a sampling theorem which states that the spatial step is defined by maximum "bandwidth" of q. Considering the typical dispersion slope of HNLF of $S = 0.02$ ps/nm^2/km, the spacing $\Delta\lambda = 10$ nm, $<\lambda> = 1550$ nm, and tuning range of $\lambda_{max}-\lambda_{min} = 50$ nm, the maximum q_{max} is equal to 0.08 m^{-1} corresponding to spatial step $2\pi/q_{max} = 80$ m.

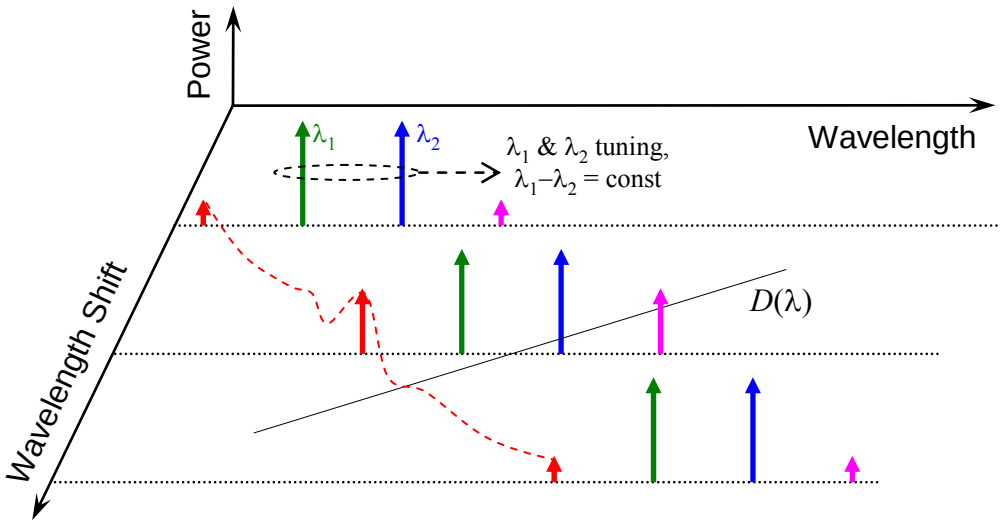

Fig. 6: Schematic representation of Brener's method.

Mussot [39] used the measured parametric gain profiles for different pump wavelengths to obtain a dispersion map. The spatial dispersion function was then optimized to fit the measured data. Unfortunately, this method does not provide a physical interpretation of the spatial resolution and could not be considered as valid as it could not be related to a unique physical dispersion map.

2. New Dispersion Measuring Method

2.1 Counter-Collision Architecture

In contrast to conventional dispersion mapping techniques designed for high-dispersion fiber types described in the previous chapter, the primary motivation for this work resides in measuring dispersion fluctuations in *low dispersion* waveguides such as HNLF. Recognizing this fundamental requirement, the new technique, if it is to successfully measure the waveguide with arbitrary (including near-zero) dispersion with high spatial resolution, it must be capable of spatial FPM control. More importantly, this control must be decoupled from the fiber dispersion or any other waveguide characteristics. Motivated by this requirement, the new measurement method is based on a simple idea that co-propagating waves with sufficiently low power will not generate significant mixing terms, even when propagating in a low-dispersion waveguide. By engineering spatially discrete, abrupt means for power increase anywhere along the fiber, the FPM generation could then be "switched on" in a spatially selective manner.

The new FPM localization in an arbitrarily dispersive waveguide is illustrated in Fig. 7.

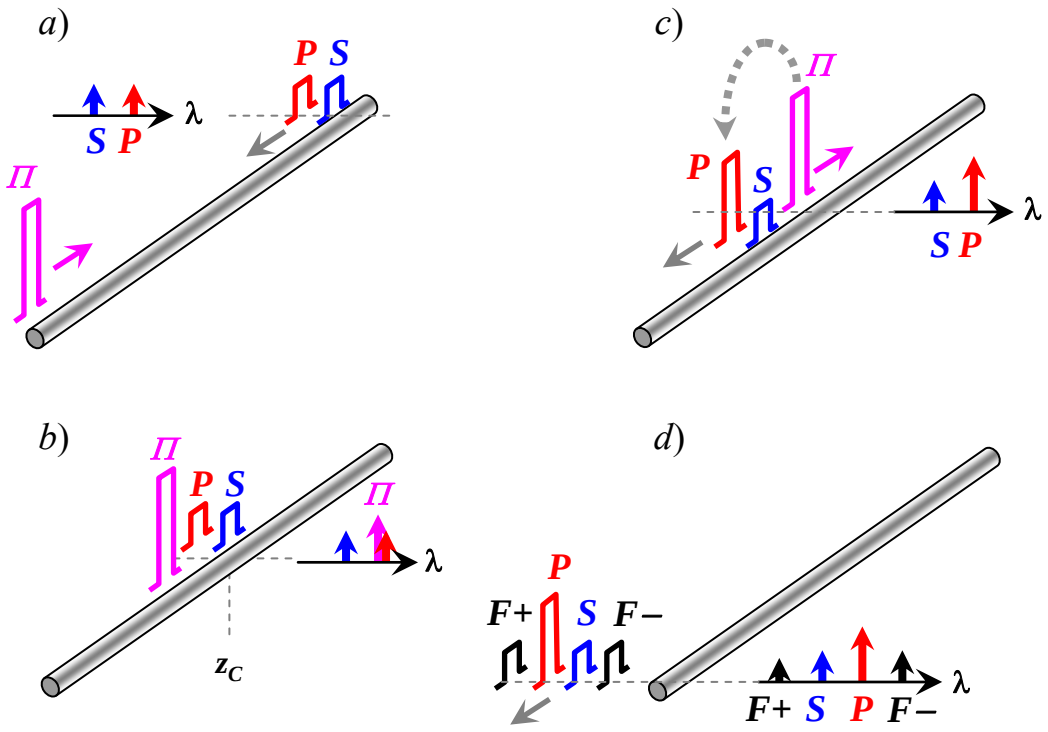

Fig. 7: FPM localization principle; *a*) Low power probe (*P*) and second signal (*S*) are launched contra-directionally to the pump (*Π*); *b*) Collision: probe is amplified by counter-propagated pump; *c*) FPM sidebands (*F*+/–) are generated along the reminder of the fiber (z_C, *L*).

The frequency non-degenerate probe (*P*) and second signal (*S*) pulses are launched into the waveguide with sufficiently low powers to guarantee negligible signal-probe mixing. The power of a single (or both) pulses is abruptly increased at the selected collision point (z_C), resulting in efficient signal-probe mixing along the remaining waveguide section. Highly localized power delivery is accomplished by a counter-propagating pump (*Π*) pulse that interacts with one (or both) pulse(s) during the brief fly-through interval. The counter-colliding interaction length, defined by the pump-probe pulse convolution, effectively represents the physical resolution of the technique: by controlling the duration of either the pump or the probe pulse, it is possible, within the limits of the physical power transfer mechanism, to arbitrarily program the spatial

precision of the measurement. The powers of the signal-probe mixing terms ($F+/-$) are measured for each collision instance and provide a unique signature of spatially distinct FPM processes. By moving the collision location z_C arbitrarily along the fiber, the FPM signatures of progressively longer (or shorter) fiber sections are obtained until the entire fiber length is scanned, as illustrated in Fig. 8. Consequently, the FPM powers corresponding to all the collision points are used to retrieve the spatial dispersion map of the entire fiber.

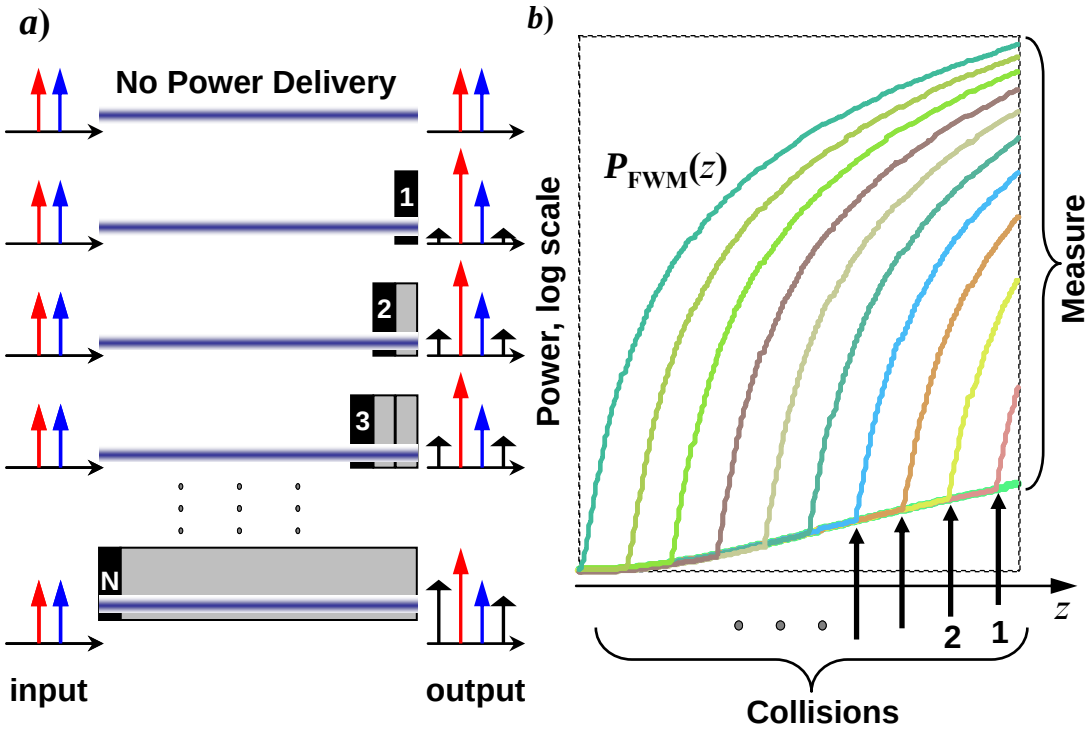

Fig. 8: Physical picture of the counter-collision technique.

2.2 Localized Pulse Amplification

At least two physical mechanisms are capable of amplifying the probe during the counter-collision instance – stimulated Raman (SRS) and Brillouin (SBS) scattering effects. The relevant process parameters are compared in Table I: . Although the Raman

process is considerably faster and supports sub-picosecond pulse amplification, the stimulated Brillouin interaction has nearly a hundred-fold larger gain coefficient [42, 48] and consequently requires lower pump powers. Furthermore, the interaction distance (~ m) required for HNLF-like measurement target is short enough to eliminate any significant noise accumulation in the case when Brillouin power delivery is used. A simple estimate of the necessary pump power can be made by requiring that the counter-colliding Brillouin pump delivers 20 dB of gain within a 2 m pump-probe flythrough interval. Assuming a standard [55] silica gain coefficient Γ of $4.6 \cdot 10^{-11}$ m/W and HNLF effective area [22] of 10 μm^2, the pump pulse should have a watt-peak power. While the counter-colliding power delivery could also be achieved by Raman pumping, hundreds of watts of peak pump power would be required in this case and, in effect, would lead to pulse self destruction of the pump pulse (mainly, by generating spontaneous noise) in HNLF lengths exceeding tens of meters. Consequently, the Brillouin pumping scheme is selected as the mechanism of choice for long (~ km) measurements, while Raman pumping is more suited for short waveguide mapping (~ m) that requires sub-millimeter spatial resolution.

Table I: Physical Properties of the Stimulated Scattering Effects.

Physical Process	Raman	Brillouin
Gain coefficient	~0.005 $m^{-1}W^{-1}$	>1 $m^{-1}W^{-1}$
Pump Power Required for 10 ns pulse and 20 dB gain	>100 W	>1 W
3-dB-bandwidth	10 THz	20 MHz
Time Response $\Delta\tau$[1]	0.05 ps	25 ns
Corresponding Spatial Resolution, $v\Delta\tau$	10 μm	5 m

The exact Brillouin gain spectrum of a specific HNLF sample can be measured by capturing the back-reflection of strong input CW wave, using simple setup illustrated in Fig. 9. The back-reflected spectrum contains the Rayleigh peak centered at the signal frequency and symmetrically located Stokes and weak anti-Stokes waves down-shifted and up-shifted from the carrier by the characteristic phonon frequency given by the fiber composition. The SBS shift is inversely proportional to the optical wavelength of the probe [55], as shown by the HNLF measurement illustrated in Fig. 11*a*. The coarse (> MHz) measurement of the Brillouin frequency was given by the spacing between the Rayleigh and the Stokes waves.

[1] The characteristic response time is calculated assuming the relation for the time-bandwidth product for Gaussian gain profile $\Delta\tau_{1/2}\Delta\nu_{1/2}\approx 1/2$.

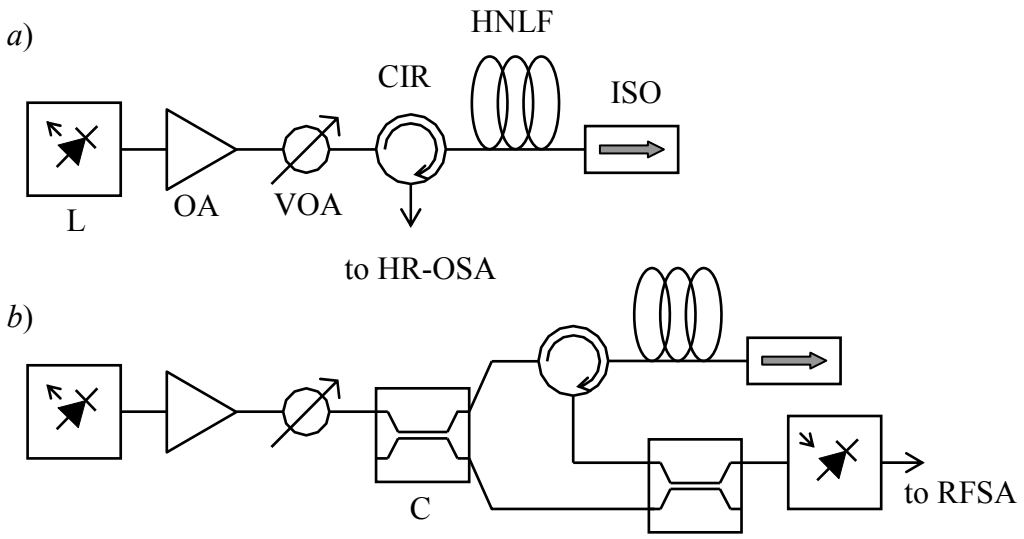

Fig. 9: The setups used for back-reflection spectral measurement: *a*) direct measurement of the back-reflected light by high-resolution optical spectrum analyzer (HR-OSA), *b*) measuring of the beating of the original CW wave and back-reflected Stokes wave at the receiver using a radio frequency spectral analyzer (RFSA). The indexes used: L – CW laser, OA – optical amplifier, C – coupler, CIR – circulator, ISO – isolator, VOA – variable optical attenuator.

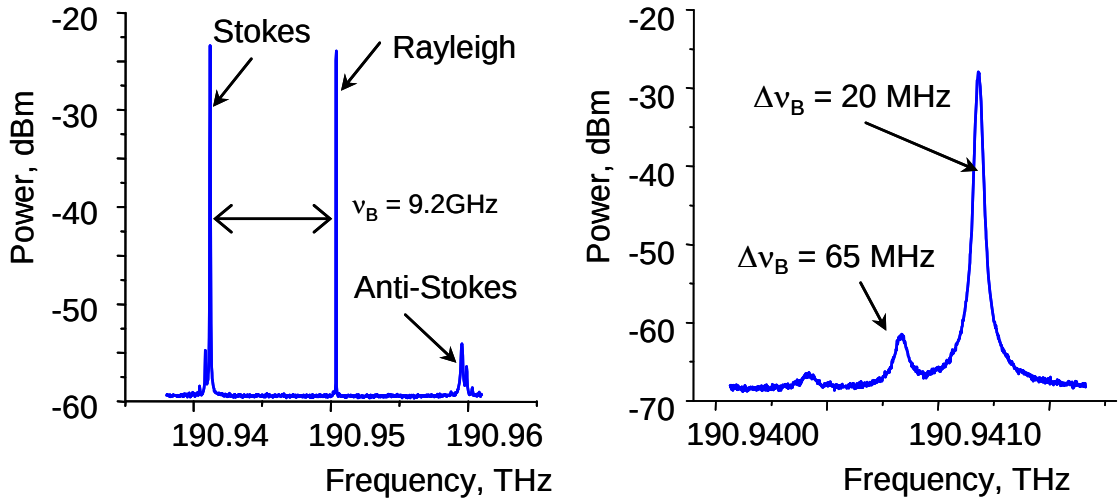

Fig. 10: *a*) Backreflected spectrum generated in 270-m HNLF sample and recorded using the heterodyne optical spectrum analyzer (resolution bandwidth ~1 MHz). *b*) High-resolution spectrum of the Brillouin HNLF Stokes component.

A high precision measurement (< MHz) was performed by maximizing the peak power of the amplified probe pulse acquired by a fast sampling oscilloscope. The precise Brillouin frequency-locking mechanism is further described in Section 3.2. The high-

resolution capture of the Stokes spectrum shown in Fig. 10 indicates the primary Brillouin peak 3-dB bandwidth of 20 MHz. The secondary 65 MHz-wide peak appears nearly 30 dB below the primary peak. The narrow amplification bandwidth ($\Delta\nu_B \sim 20$ MHz) sets a strict limit on the duration of the probe pulse $\tau_B = (2\Delta\nu_B)^{-1} \sim 25$ ns and, consequently, on the spatial resolution of the technique (~ 2 m). As a result of the close match between the pulse and gain spectral width, the amplified pulse does not necessarily retain its original shape, as illustrated in Fig. 11*b*. In other words, the instantaneous gain seen by the probe pulse varies, and the exact amplified waveform represents the convolution between the input pulse and the Brillouin gain functions.

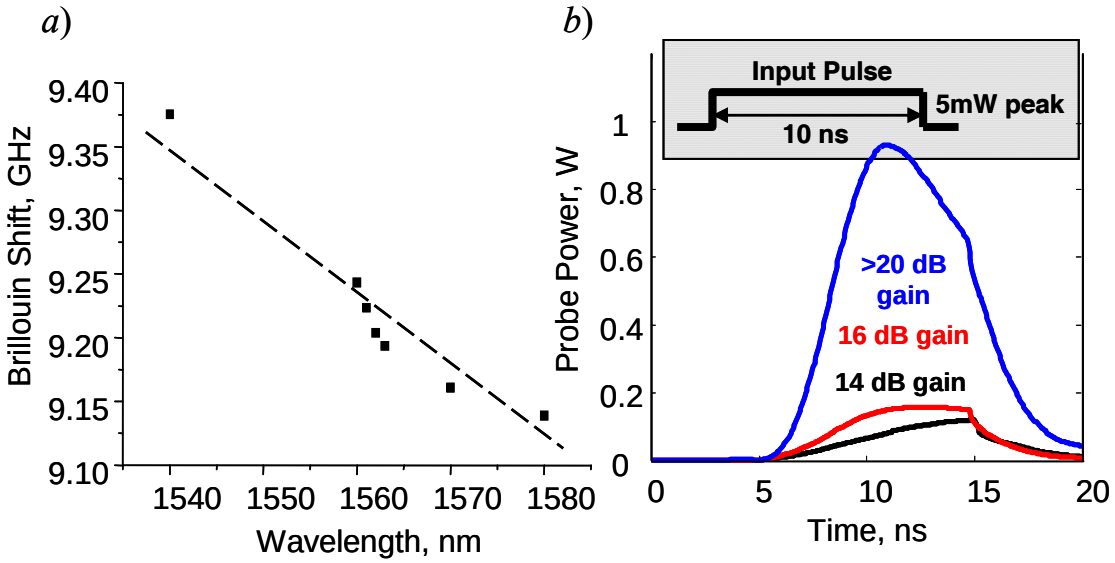

Fig. 11: *a*) Measured SBS frequency shift in a 200-m long HNLF sample. *b*) Measured waveforms of the amplified 10-ns pulse for different HNLF samples and varying SBS gain. HNLF section length, peak input power and Brillouin gain are given as (blue) 270 m, 8 mW, >20 dB, (red) 210 m, 4 mW, 16 dB, (black) 200 m, 5 mW, 14 dB.

On the other hand, the slow phonon-photon interaction response, as well as the counter-propagating nature of SBS, makes the pulse amplification relatively insensitive to the exact form of the pump pulse. The latter observation is supported by the

experimental measurements illustrated in Fig. 11*b*; gain compression leads to the variable characteristic time that can be faster than that of the calculated waveform using a bandwidth-constrained linear assumption.

The probe (pump) pulse duration represents the basic temporal resolution of the measurement. However, an intuitive argument can be constructed in which the exact temporal shape of the amplified pulse is not the sole governing factor of the measurement. While the ultrafast nature of the signal-probe mixing does respond to the instantaneous power of the pulse, the optical power measured at the end of the fiber is defined by the integration of the FPM terms during the entire pulse duration. It is also important to avoid the oversimplification, since the amplified pulse shape does govern higher-order accuracy of the nonlinear pulse-probe interaction and is position-dependent. In addition, the experimental limitations significantly affect the accuracy of the method. Consequently, the optimal technique needs to combine the fact that FPM measurements are pulse-integrated measurements and incorporate the corrections borne by intra-pulse intensity variations.

The narrow gain profile and the variation in the Brillouin response require precise locking between the pump and probe center frequencies. In ideal case, negligible HNLF transverse geometry fluctuation would guarantee a constant Brillouin downshift at any fiber location. In practice, the optimum Brillouin shift varies along HNLF and has to be precisely matched along the entire length of the fiber in order to maintain maximum power transfer for each collision instance. The last fact implies that the spacing between signals must be controllable with the accuracy defined by a fraction of the SBS gain

bandwidth. The main reason for such behavior is pump-pulse chirping during propagation and the non-harmonic Brillouin response for high pump powers.

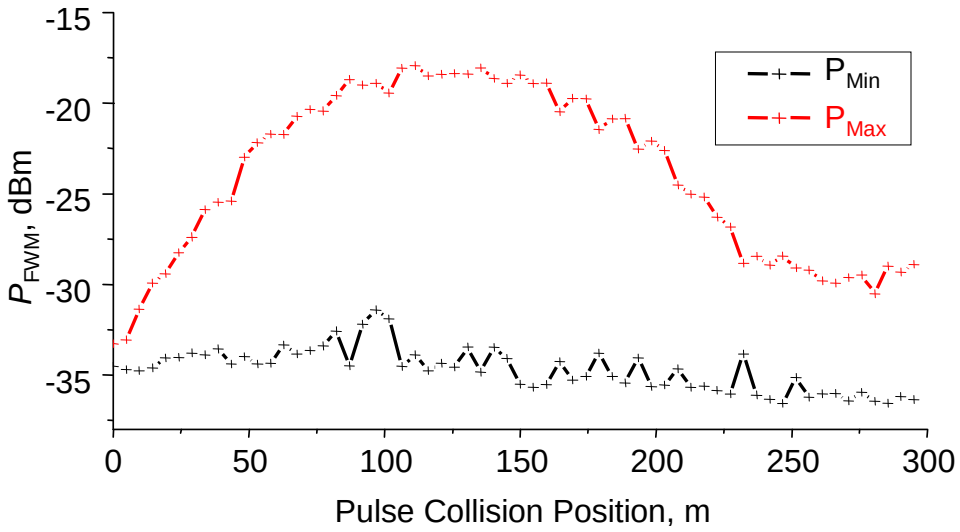

Fig. 12: Powers of the Stokes wave corresponding to the maximum (pump-probe co-polarized state) and minimum (pump-probe cross-polarized state) Brillouin gain instance.

In final consideration regarding counter-colliding power delivery, it must be recognized that stimulated Raman and Brillouin processes are polarization dependent. In practice, only one polarization state is preferentially amplified, thus requiring strict polarization alignment at each collision instance. More importantly, *experimental observations have demonstrated that the polarizations of both the probe and pump must be controlled to maximize the probe gain*. This implies that their Stokes vectors must not only be co-polarized but also have a specific polarization state. Fig. 12 illustrates the effect of precise collision polarization control: the average power of the Stokes FPM product was measured for polarization states corresponding to the maximum and minimum probe gain. The detailed properties of the polarization evolution in the fiber are described in chapter 7.1.

3. Experimental Architecture

3.1 Adaptive Counter-Colliding Scanner

A qualitatively new dispersion measurement was designed the purpose of this research. Fig. 13 illustrates one of the experimental setups used to validate the new principles. A continuous wave (CW) laser source L_1 was split (C_1) and used to create the frequency-locked pump (Π) and the probe (P) waves. Firstly, the probe wave was downshifted by the exact Brillouin frequency corresponding to each collision instance using the single sideband (SSB) modulator driven by the adaptive clock CL_1. The SSB clock tracked the exact Brillouin frequency for each collision instance. Secondly, the probe and pump pulses were created by the amplitude modulators AM_1 and AM_2. An independent laser source L_2 and modulator AM_3 were used to generate a signal (S) co-propagating with the probe. Two laser branches were temporally balanced to obtain a complete overlapping of interacting pulses. The pump and probe pulses were generated by two independent pattern generators ($PG_{1,2}$) synchronized to a master clock (CL_2). The spatial localization of the pulse within HNLF was controlled by programmed bit sequences in each PG unit. The accuracy of such pulse positioning (time sampling) was defined by the inverse clock frequency. The experiment used a 1 GHz master clock, guaranteeing the spatial (temporal) sampling interval of 20 cm (1 ns). The complement of amplifiers ($A_{1\text{-}4}$), attenuators ($AT_{1\text{-}4}$) were used to manage the power states.

Polarization controllers $PC_{1\text{-}4}$ were used to align the input polarizations along modulator principle states, $PC_{5\text{-}7}$ – to align pulse polarizations along the transmission axes of the front polarizers of the motorized polarization controllers $PC_{8\text{-}9}$. Thin film tunable filters placed after every amplifier and not shown Fig. 13 were used after every amplifier to suppress spontaneous noise. Circulators CIR_1 and CIR_2 were used to couple counter-propagating pulses and collect the signal, probe, pump and FPM waveforms. The polarization and (Brillouin-shift) frequency state of the interacting waves were strictly controlled prior to each collision instance, facilitated by monitoring provided by an optical spectrum analyzer, oscilloscope and power meter diagnostic block.

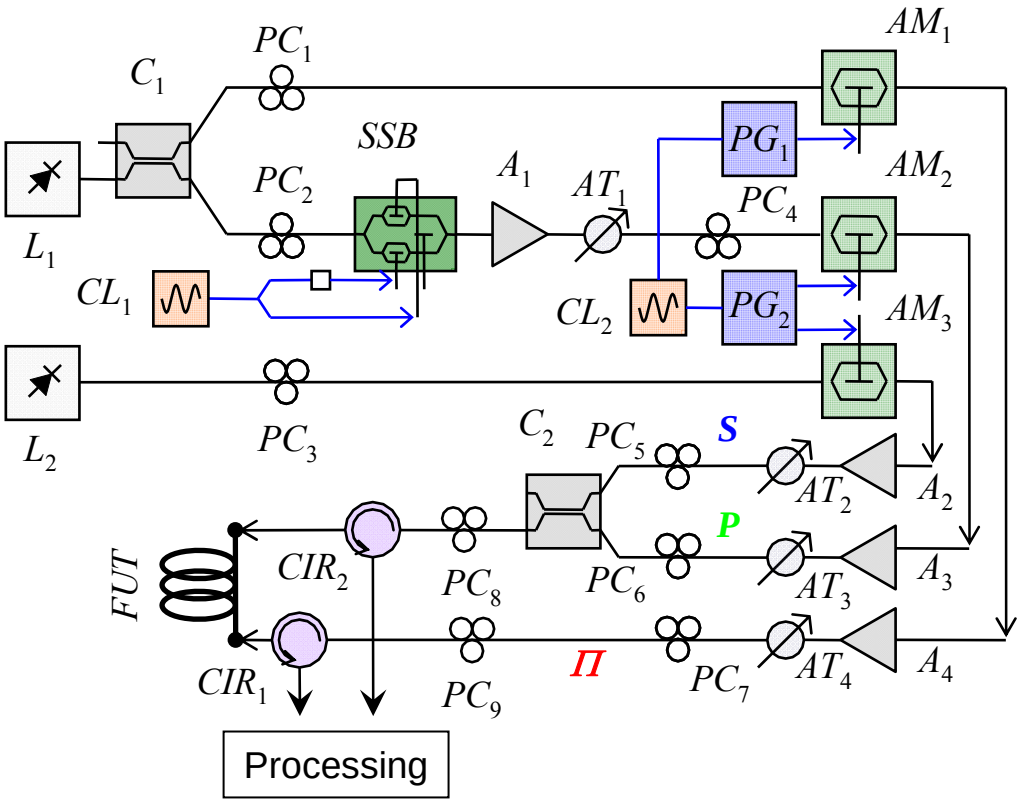

Fig. 13: Experimental setup.

The measurement process was fully automated requiring only initial manual localization of the collision at the very end of the fiber.

3.2 Frequency Locking

As pointed out previously, the frequencies of interacting signals must be precisely locked to match narrow (~20 MHz) SBS gain profile. The stable frequency position was obtained by splitting the output of the laser and shifting the frequency of the single output by the optical single sideband (SSB) modulator. The implementation of frequency shifting scheme is illustrated in Fig. 14: a master clock drives two RF arms of the modulator; a single arm is delayed by a clock quarter period, while the third (DC) input of SSB modulator sets a 90° phase shift between its lower and upper arms.

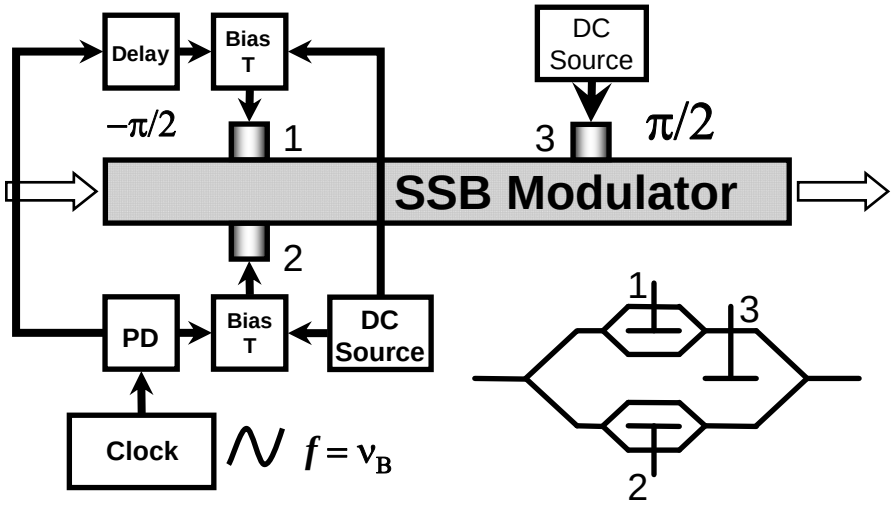

Fig. 14: SSB modulator biasing scheme. Inset indicates interferometric topology of the device.

The biasing of the SSB modulator was a three step procedure. At the first stage, the RF modulator inputs are switched off and the reference ("zero point") voltages for interferometers 1 and 2 are set. At this configuration, the output does depend on the bias for the master (outer) interferometer because zero signals are combined. At the second

stage, the RF peak amplitudes corresponding to carrier-suppressed return to zero (CS-RZ) [51] configuration are adjusted to suppress the original carrier. Finally, the phase delay at the master interferometer and the delay between RF signals are set to provide the maximum power for the downshifted sideband and minimum power for any other harmonic by observing the OSA spectrum. In ideal case, a solitary downshifted carrier is generated. In practice, the typical suppression ratio of more than 30 dB for the original carrier and 25 dB for complementary clock at triple modulation frequency can be achieved, as illustrated in Fig. 15. Precise bias tuning was performed by eliminating any modulation of the output waveform using the fast oscilloscope. The presence of the higher order harmonics typically indicated the loss of symmetry in biasing of the upper and the lower modulator arms, or the modulator being overdriven. The biases can be automatically tracked by commercially available bias controllers (for example, [52]).

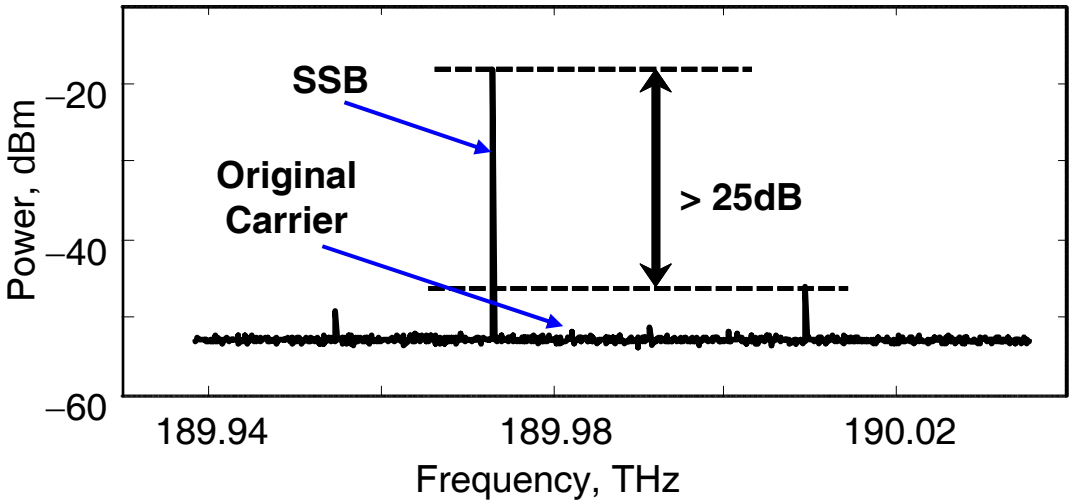

Fig. 15: Typical spectrum achieved by SSB frequency shifting.

3.3 Polarization Control

The motorized polarization controllers were used to set the state of the polarization (SOP) of the pump (PC_9) and probe/second pulse (PC_8), as illustrated in Fig.

13. The controllers have input polarizer followed by a pair of half-waveplate (HWP) and quarter-waveplate (QWP). The polarization states are specified by setting polarization azimuth η and ellipticity ε. SOPs were chosen to maximize the power for the amplified probe (counter-collision gain). Specific pump/probe/signal SOP was searched using a specific strategy: the polarization states are optimized in Stokes domain. In first step, initial SOP settings (±1, 0; 0), (0, ±1, 0) and (0, 0, ±1) were used in attempt to identify the octant with the maximum gain on the standard Poincare sphere. In the second step, the octant was iteratively shrunk to a cone on the Poincare sphere that satisfied the condition of growing counter-collision gain. The process repeated until the SOP was localized within the narrow cone defined by a central angle less than 5°.

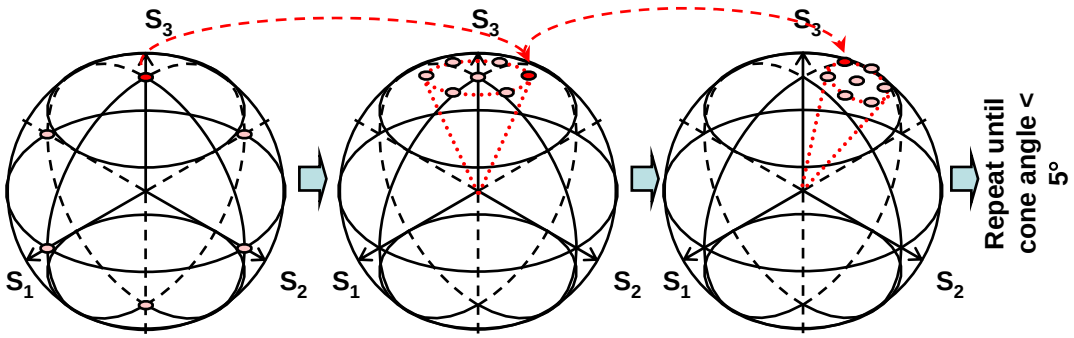

Fig. 16: Algorithm of the polarization control.

3.4 Spatial Localization of Pump-Probe Collision within the Fiber

Precise control of the pulse-probe collision position is critical, as it is uniquely related to the local dispersion fluctuation map. The collision scanning process originates at the end of the fiber and proceeds to cover its entire length. In order to localize the pulse collision at the end of the fiber, two conditions must to be satisfied:

1) the spacing between pulses multiplied by its group velocity must be longer than the doubled fiber length, and
2) the pump-probe pulses must overlap both at the beginning and at the end of the fiber.

These conditions are illustrated in Fig. 17. The condition requires the precise selection of the delay between the pump and the probe pulses and loading of the length-specific bit sequence to both the pump and probe pattern generators. In practice, the pulse waveforms synthesized by the pattern generators are not ideally rectangular and possess a long trailing tail that accounts for finite fraction of the pulse energy. The pump tail could potentially interact with the probe thus delocalizing amplification, or, equally important, the tail of probe could be amplified by the counter-propagating pump. This amplified tail can be clearly identified in Fig. 11. To avoid this impairment, we used the pattern generator temporal buffering whereby additional bits were added to the original bit sequence that formed the pump/probe pulse. As an example, consider a 200-m-long fiber corresponding to 2 μs double-pass propagation time and 1-GHz master clock. In this case, the required sequence length amounts to 2000 programmed bits. Upon adding a buffer zone of 500 bits, the total bit sequence will consist of 2500 bits, which is a sufficient guard-band to avoid the afore mentioned trailing edge impairment.

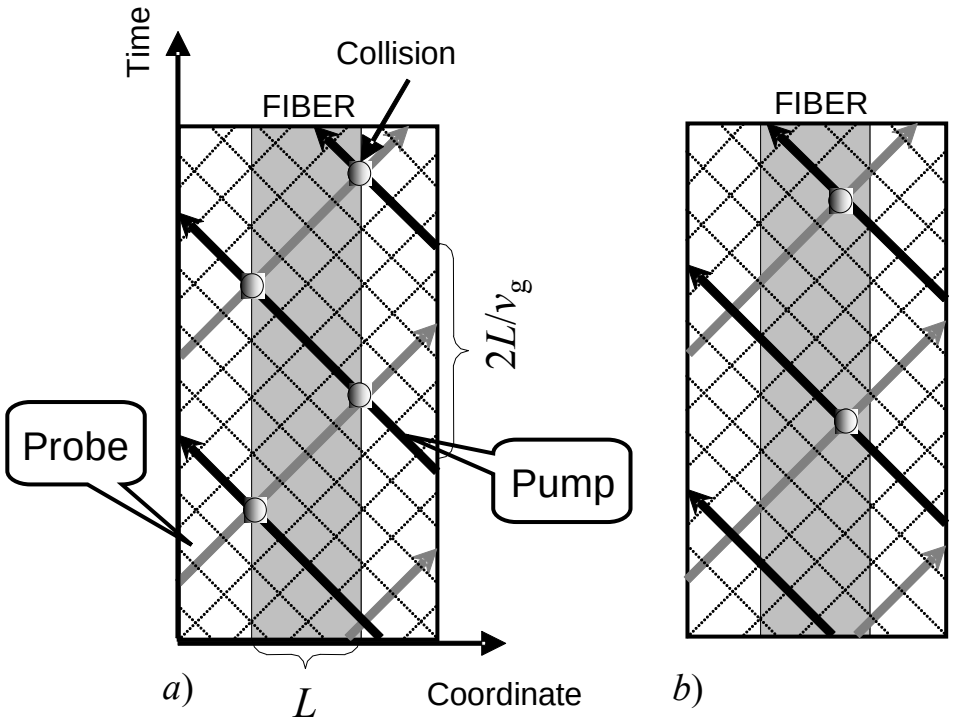

Fig. 17: Time-space collision analysis: *a*) collision at the beginning of the fiber, *b*) collision within the fiber.

The fast calibration can be done by a three-step manual search:

1) firstly, the position of markers in the probe pattern bit sequence is used as a temporal reference (i.e. $t = 0$),
2) secondly, the temporal position of the pump pulse is varied in a coarse manner to find the no-collision state, (i.e. absence of Brillouin amplification at the end of the fiber);
3) finally, the probe temporal reference is shifted to the position just prior to the amplification onset ($t' = 0$, i.e. single temporal increment would toggle between a gain and zero-gain at this position). It is easy to note that such collision points correspond exactly to the end of the fiber.

3.5 Bias Control and its Implications

The power transfer from the pump pulse to the probe should be strictly localized to be confined to collision interval only, avoiding any interaction with the pump pulse pedestal (trailing edge). Practically, any modulation scheme used for pump pulse formation has a finite extinction ratio (see Fig. 18*a*), leading to non-zero light level trailing the main pulse. If this power level is lower than the characteristic threshold of the nonlinear effect (Brillouin in this case), the power transfer between the probe pulse and the pump pedestal becomes negligible. Conversely, non-negligible probe pulse amplification will occur even in absence of the collision with the main pump pulse. Such amplification regime is distributed, rather than spatially localized, and represents the exact opposite of the scheme desired in the type of measurement under consideration. Furthermore, it is important to note that in the latter case, the probe pulse would become significantly impaired by the amplified spontaneous noise accumulated along the entire fiber length. To illustrate its impact, it is sufficient to estimate the Brillouin threshold of a 250 m long HNLF segment using standard scaling between gain, effective area and the effective fiber length [42]. The combination of watt pump peak power and SBS threshold power of ~20 mW, dictates the minimum 20 dB extinction ratio to be maintained throughout the measurement at AM_1. However, we have found that the probe gain and OSNR degradation can serve as a reliable feedback signature in case when collision did not occur within the HNLF, as illustrated in Fig. 18*b*.

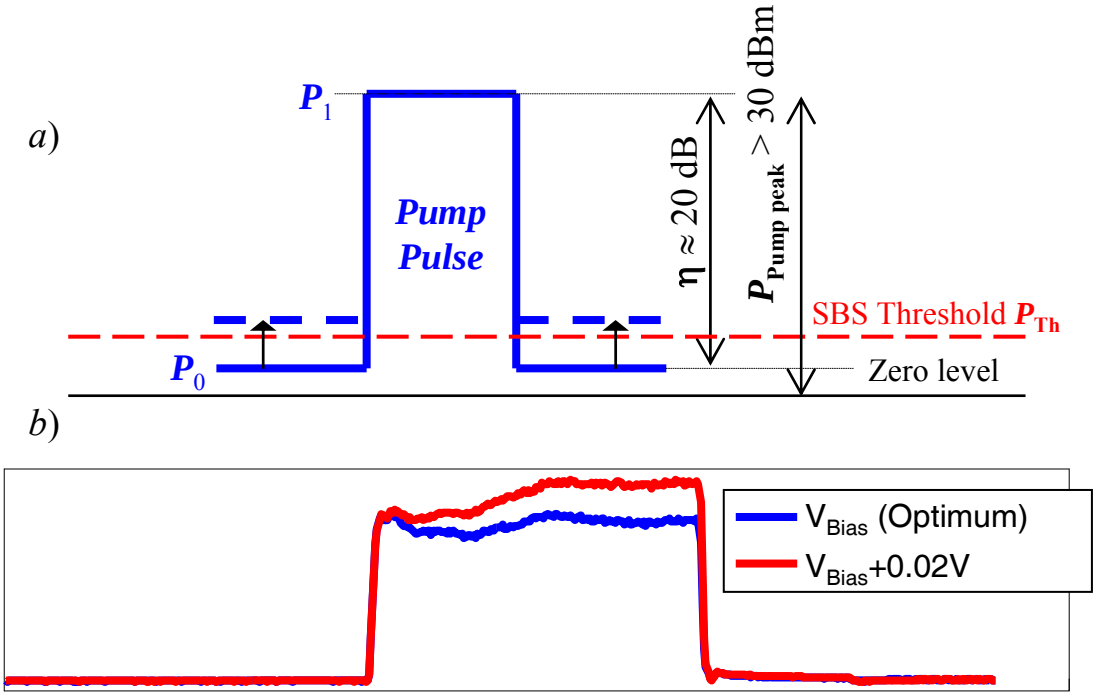

Fig. 18: *a*) Basic requirements for pulse geometry. *b*) Measured probe pulse waveform at the points where no pulse collision occurs in the fiber corresponding to the bias providing maximum extinction ratio (blue) and waveform corresponding to 0.02 V shift from optimum bias (red).

3.6 FPM Tone Acquisition and Gain Calibration

The algorithm of dispersion map reconstruction described in chapter 5 critically depends on accurate measurements of the pump/probe/FPM pulse powers. Our measurements have demonstrated that the average powers acquired by a conventional power meter were not accurate enough to obtain the precise peak pulse powers as the typical error was approximately 2 dB.

The first reason for this inaccuracy is the finite extinction ratio of the optical modulators used to carve the pulses and create frequency-shifted carriers. Indeed, simple calculations reveal that an extinction ratio of 24 dB would lead to a 3 dB discrepancy if 240-bit long sequence consisting of one isolated mark. As a second-order effect, the

pulse generator also produces a long non-zero transient tail described in the previous section. Finally, the pulse shape after amplification does not possess an ideal rectangular shape, as shown in Fig. 11, thus prohibiting simple scaling laws.

Alternatively, a pulse gating scheme, optical or electrical, should be used. Unfortunately, the optical gating scheme based on Mach-Zehnder modulators is not viable in practice due to their inherent polarization dependence: the polarization of the pulses must be adjusted for every collision instance only to impose temporal gating. In an alternative implementation, an acousto-optic modulator is polarization insensitive, but has a long impulse response, rendering its usefulness for the task at hand.

To address all the issues outlined above, we used a fast sampling oscilloscope for pulse localization within the window equal to the length of the loaded bit sequence. In addition, the pulse waveforms were stored for off-line processing. The detection scheme contained two devices with low (<0.1 dB) polarization dependent loss (PDL):

1) a variable optical attenuator required to keep the peak pulse powers within the linear reception band, and
2) a tunable optical filter required to select a single spectral tone and suppress background noise. Prior to any waveform acquisition, the zero-mean thermal noise was reduced by multiple averaging.

Finally, in case when the probe and the signal pulse powers were high (>25 dBm), the undepleted approximation was no longer valid and did not allow simple gain estimation using the ratio of the powers measured at the beginning and at the end of the fiber. This mandated the separation of SBS amplification from FPM and Raman power

transfer. In the experiment, the problem was solved by switching the laser generating the second pulse off, on the course of the counter-collision gain measurement.

3.7 Interacting Wave Power Range and its Implications

There are certain ranges of the powers of counter-propagating pulses providing best system performance; specifically, the parameters such as contrast, spatially equalized gain, and power for FWM product have to be optimized. In ideal case, the localized gain should be as high as possible and constant across the fiber. However, in practice, the gain is limited by the launched pump pulse power. The low pump power corresponds to low gain and poor contrast. Conversely, if high pump power is high, the pulse is distorted by fiber nonlinear effects, predominantly, by generation of the spontaneous Raman noise. As a result, a gain is maximized only at the front fiber section and is being degraded as the pump pulse propagates deeper to the waveguide. If the power of the amplified probe or a second pulse is too high, the pulses start exchanging their energy by means of Raman amplification, causing significant difficulties in gain calibration and adding uncertainties in power readings. In addition, high pulse powers result in polarization walk-off between the pulses (i) degrading conversion efficiency and (ii) making inaccurate a scalar model used to reconstruct a ZDW map. All issues described above are summarized schematically in Fig. 19. The sides of the diagram are attributed to three different pulses; the color intensity defines the pulse powers, and the rays crossing triangle sides correspond to the optimum power levels.

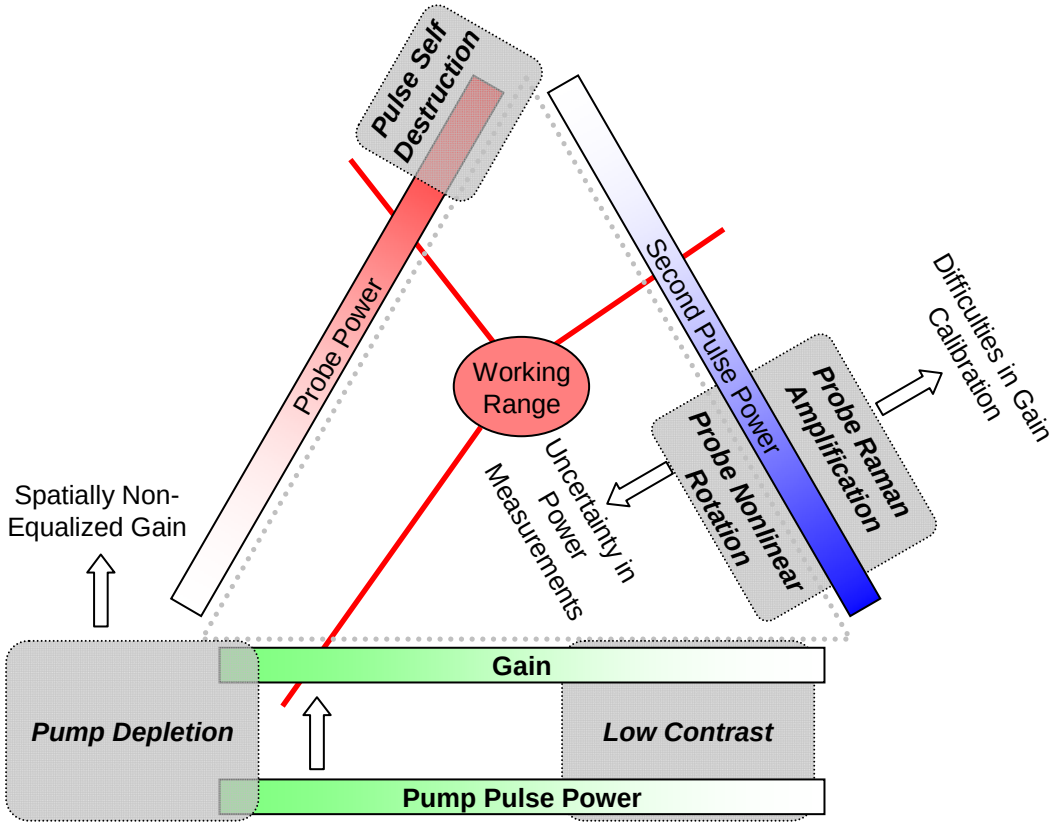

Fig. 19: A diagram demonstrating how to set optimum pulse powers.

3.8 Requirements for Pulse Wavelengths

Establishing the signal and the probe wavelengths with respect to the global zero-dispersion wavelength (ZDW) is an important consideration for experimental measurements. High pump peak powers (>1 W) dictated positioning within the *normal* dispersion regime to avoid nonlinear pump pulse distortions or pulse self-destruction. The second argument is a tradeoff between the efficiency of generation of FPM products and measured power dynamic range. In order to increase the dynamic range, the linear phase mismatch should be increased; however this requirement also necessarily leads to the efficiency decrease. The first configuration providing the effective generation of the FWM wave corresponds to the close (<5 nm) positioning of the probe and second pulses

shifted far (>20 nm) from ZDW to a normal dispersion band. However, such regime provides poor sensitivity of the measured profiles to ZDW variations. As an illustration, the FWM power traces generated in 210-m *L*-band fiber were measured in forward and backward directions (Fig. 20). Although the fiber has more than 5-nm ZDW fluctuations, the traces are almost identical proving a statement of poor sensitivity.

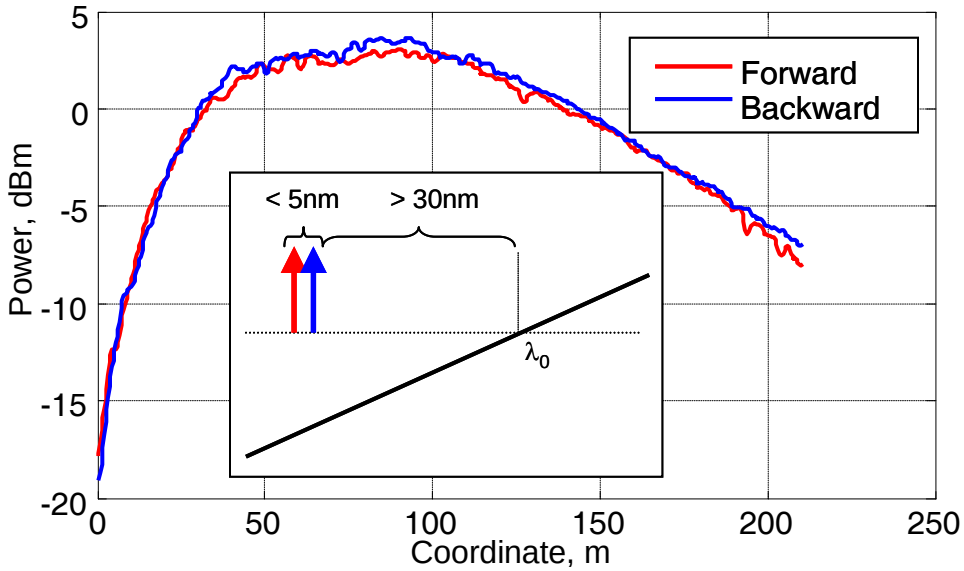

Fig. 20: Measured powers of propagated pulses scanned in both directions for 210-m HNLF sample.

A wide signal-probe separating (>20 nm) and a probe positioning closer to the ZDW were identified as one configuration capable of creating the compromise between measurement sensitivity and high FPM efficiency. All experimental results presented in the following sections were obtained in this regime.

4. Numerical Algorithms

4.1 Nonlinear Schrödinger equation

The generalized equation describing propagation of signal waveforms in optical fibers [54-57] is given by

$$\frac{\partial}{\partial z}A(t) = \left[\hat{\mathrm{A}} + \hat{\mathrm{D}} + \hat{\mathrm{N}}\right]A(t) \tag{4.1}$$

where $A(t)$ is the complex vector corresponding to propagating sampled bands (the complex envelope of the signal in time domain), $\hat{\mathrm{A}} = -\alpha/2$ is the operator describing fiber losses α measured in [m^{-1}] units, $\hat{\mathrm{D}}$ is the operator responsible for linear effects of dispersion, $\hat{\mathrm{N}}$ is the nonlinear operator.

Linear dispersive operator in frequency domain is defined by

$$\hat{\mathrm{D}}(\omega) = \sum_{n\geq 2}\beta_n \Delta\omega^n / n! \tag{4.2}$$

which corresponds to differential operator

$$\hat{\mathrm{D}}(t) = \sum_{n\geq 2} j^{(n+1)}\beta_n \frac{\partial^n}{\partial t^n} \Big/ n! \tag{4.3}$$

in time domain. This equation (1) is well known nonlinear Schrödinger equation (NLSE) [55-60]. The coefficients β_n are the coefficients of Taylor series of the propagation coefficient $\beta = n_{\mathrm{eff}} \cdot k_0$ expanded in the vicinity of specific reference frequency ω_{ref}, n_{eff} is a

mode propagation index defined by both waveguide and material properties. The index n refers to $n^{\text{-th}}$ order term of chromatic dispersion. The series is truncated considering the sufficient number of terms for accurate description of the dispersion effect. In practice, the wavelength dependent dispersion profile D_λ can be obtained using a commercially available dispersion measuring test sets. In this case, the dispersive term defined by eq. (4.2) can be replaced by direct integration of dispersion profile

$$\hat{\mathrm{D}}(\omega) = \int_{\omega_{ref}}^{\omega} d\omega' \int_{\omega_{ref}}^{\omega'} \beta_2(\omega'')d\omega'' \tag{4.4}$$

in which $\beta_2(\omega'') = -\dfrac{2\pi c}{\omega''^2} D_\lambda(\omega'')$.

The nonlinear operator $\hat{\mathrm{N}}$ describes all effects depending on the power of propagated signals. Relative to characteristic time of the nonlinear response, the nonlinear operator can be separated into near-instantaneous part (~7 fs) [55], usually referred to Kerr effect, and the time-delayed part characterizing the Raman (molecular vibration) scattering [60]. The nonlinear operator defining the evolution of a single optical band is given by [59-60]

$$\hat{\mathrm{N}}(t)A(t) = j\gamma A(t)\left[\underbrace{\xi_K(1-\rho)|A(t)|^2}_{\text{Kerr}} + \underbrace{\xi_R\rho A(t)\int_0^{\infty} h(\tau)|A(t-\tau)|^2 d\tau}_{\text{Raman}}\right] \tag{4.5}$$

where $\gamma = n_2\omega_{ref}/cA$ is the fiber *mode* nonlinear coefficient, n_2 is a *bulk* nonlinear refractive index, A is an mode effective area, ρ is coefficient defining the fractional contribution of the delayed Raman response to the entire nonlinearity, $h(t)$ is a real

normalized Raman response function, $\int h(t)dt = 1$, ξ_K and ξ_R are factors (ξ_K, ξ_R<1) defining polarization properties of Kerr (K) and Raman (R) effects.

In practice, if the nonlinear interactions outside the specified signal bands are negligibly small or not considered, it is advantageous to represents different signals relative to their carriers ω_n. In this case, the total electrical field is represented as a superposition of corresponding envelopes $A_n(t)$

$$A(t) = \sum_n A_n(t) e^{j\omega_n t} \tag{4.6}$$

Such technique is usually denoted as "frequency decomposition" [60]. After substituting expression (4.6) into equation (4.5), the two terms are transformed to five different terms for decomposed bands $A_i(t)$ [54-56, 61]

$$\begin{aligned}
&\frac{1}{j}\hat{\mathrm{N}}(t)A_i(t) = \\
&= \gamma_{ii}A_i(t)\left[\xi_1(1-\rho)\left|A_i(t)\right|^2 + \xi_2\rho\int_0^\infty h(\tau)\left|A_i(t-\tau)\right|^2 d\tau\right] + \\
&+ A_i(t)\sum_{k\neq i}\gamma_{ki}\left[2\xi_3(1-\rho)\left|A_k(t)\right|^2 + \xi_4\rho\int_0^\infty h(\tau)\left|A_k(t-\tau)\right|^2 d\tau\right] + \\
&+ \xi_5\rho\sum_{k\neq i}\gamma_{ki}A_k(t)\int_0^\infty h(\tau)A_k^*(t-\tau)A_i(t-\tau)e^{2\pi j(f_i-f_k)}d\tau
\end{aligned} \tag{4.7}$$

The first and second terms define instantaneous and delayed nonlinear effects of the self-influence known as self-phase modulation (SPM) and intra-band Raman scattering, the third and forth terms are responsible for the instantaneous and delayed phase shift (or, cross-phase modulation – XPM) of the $A_i(t)$ envelope induced by $A_k(t)$ bands at different carriers. ξ are the polarization factors. The last term represented by a Fourier component at frequency f_i–f_k of the normalized function of the delayed response multiplied by beating term $A_i(t)A_k(t)^*$ is responsible for the Raman phase rotation (real part) and power

transfer (imaginary part) between the interacting bands. The nonlinear coefficient γ_{ki} of two interacting signals is given by

$$\gamma_{ki} = \frac{n_2 \omega_i}{cA(f_i, f_k)} \tag{4.8}$$

In contrast to the mode effective area A, the overlap integral $A(f_i, f_k)$ could not be measured directly. However, it can be approximated as average betweeen two effective areas measured for f_i and f_k. This approximation is accurate if the modes are Gaussian profiles. For example, the Gaussian profile represents the real Bessel mode profile for step-index fiber with 96% accuracy [69]. For the fibers with complex transversal geometry of the refractive index (such as double-clad fibers), this factor varies between 90 and 95% demonstrating that Gaussian mode fitting provides a reasonable approximation of the real mode profile.

It is important to note that the NLSE is specified in the moving coordinate frame propagated with the group velocity at the reference frequency ω_{ref}. This implies that the linear phase rotation and motion of the harmonic are "frozen" and the phases of the other spectral components are measured relative to this frequency.

4.2 Quasi-CW approximation

In most practical cases, detailed information of the signal waveform resolved in time/frequency domain is not necessary or is redundant. For example, the optimization of the broad-band amplifier characteristics for multi-channel system requires the knowledge of the gain function for specific channel count; the separate channels can be characterized by a single *averaged* channel power. The second example is the interaction

of the signals propagated in opposite directions. The signal wave mixes fast with the backwardly propagated wave and sees only its averaged field.

In general case, the figure of merit that governs the use of this approximation is defined as a product (η) of the bandwidth of the propagated signal to the characteristic time of the physical effect modifying this signal. There are three distinct situations.

If $\eta >> 1$, the variations of the signal in time are significantly faster than the speed of the system response. In this case, the effect is assumed to be stationary and the system transfer function can be represented by a filter with frequency dependent spectral profile. A typical example is the simulations of the amplification of the fast modulated signals in Er-doped amplifiers.

If $\eta << 1$, the effect can be considered as instantaneous and the evolution of different samples of the waveform can be processed independently. For instance, if the rectangular-shape 10-ns pulses are used for counter-collision power delivery and travel over sub-kilometer distances, the pulse behavior can be predicted by observing the spatial amplitude of a *single* sample carved somewhere in the middle of the pulse. In strict terms, if $\eta << 1$, the equations of the frequency-decomposed sampled waveforms can be modified by eliminating the time dependency, which is equivalent to the substitution of the optical envelopes $A_i(t)$ by a single *complex* number A_i. After this replacement, the equation (4.7) is transformed to

$$\begin{aligned} \frac{1}{j}\hat{\mathrm{N}}\, A_i &= \gamma_{ii}\left[\xi_1(1-\rho)+\xi_2\rho H(0)\right]P_i A_i + \\ &+\sum_{k\neq i}\gamma_{ki}\left[2\xi_3(1-\rho)+\xi_4\rho H(0)+\xi_5\rho H(f_i-f_k)\right]P_k A_i \end{aligned} . \qquad (4.9)$$

The newly introduced variable $P_i = |A_i|^2$ defines the power of the signal at frequency f_i, $H(\omega)$ is a Fourier transform of the delayed nonlinear response function. The factor

$$g_{Rki} = g_R(f_i - f_k) = 2\rho\gamma_{ki}H(f_i - f_k) \tag{4.10}$$

with the dimension of $[m^{-1}W^{-1}]$ is a Raman response function. It contains both real and imaginary parts. In practice, the imaginary part of g_{Rki} can be measured directly by tuning the wavelength of the weak probe signal relative to strong pump and measuring probe gain spectral dependency [43-45]. The real part can be reconstructed using Kramers-Kroenig relation between real and imaginary parts of the analytical function [46].

The equation (6) does not describe the resonant coupling of the wave at frequency f_i and three waves at f_j, f_k, and f_l. The FWM terms must be derived by substituting the expression of total field $A(t)$ that accounts four waves ($A_i e^{j\omega_i t} + A_j e^{j\omega_j t} + A_k e^{j\omega_k t} + A_l e^{j\omega_l t}$) into eq. (4.5) and grouping the resonant terms with like frequencies. The final expression for FWM operator is given by [61, 63]

$$\frac{1}{j}\hat{\mathrm{N}}\Big|_{FWM} A_i = \sum_{\substack{j,k,l;j,l\neq k \\ f_i = f_j - f_k + f_l}} \gamma_{ijkl} A_j A_k^* A_l \left[\xi_6(1-\rho) + \xi_7 \rho H(f_l - f_k)\right]. \tag{4.11}$$

Subsequently, a FWM nonlinear coefficient γ_{ijkl} becomes a complex function of four frequencies [61, 63]

$$\gamma_{ijkl} = \frac{n_2 \omega_i}{cA(f_i, f_j, f_k, f_l)}. \tag{4.12}$$

In (4.12), $A(f_i, f_j, f_k, f_l)$ is an overlap integral of the modes of four interacting signals which can be approximated by

$$A(f_i, f_j, f_k, f_l) = 4\sqrt{A(f_i)A(f_j)A(f_k)A(f_l)}\left(\frac{1}{A(f_i)} + \frac{1}{A(f_j)} + \frac{1}{A(f_k)} + \frac{1}{A(f_l)}\right) \quad (4.13)$$

This expression is accurate for the Gaussian profiles.

The most complicated situation corresponds to η having a value close to unity, in which case both spatial and temporal evolution must be simultaneously considered.

4.3 Evolution of the Signals in Counter-Collision Setup

The counter-colliding scanning measurement technique is characterized by a set of uniquely defined observables that include signal, probe, pump and FPM powers, measured at one or both fiber ends. Formally articulated, the dispersion retrieval is the inverse problem with input variables defined by the powers of controlled signals and FPM waves, measured at both waveguide ends. The signal-probe FPM interactions include both degenerate and non-degenerate mixing processes, as illustrated in Fig. 21. The dominant FPM process is described by the degenerate photon exchange whereby two probe photons are annihilated and create anti-Stokes and Stokes-shifted photons.

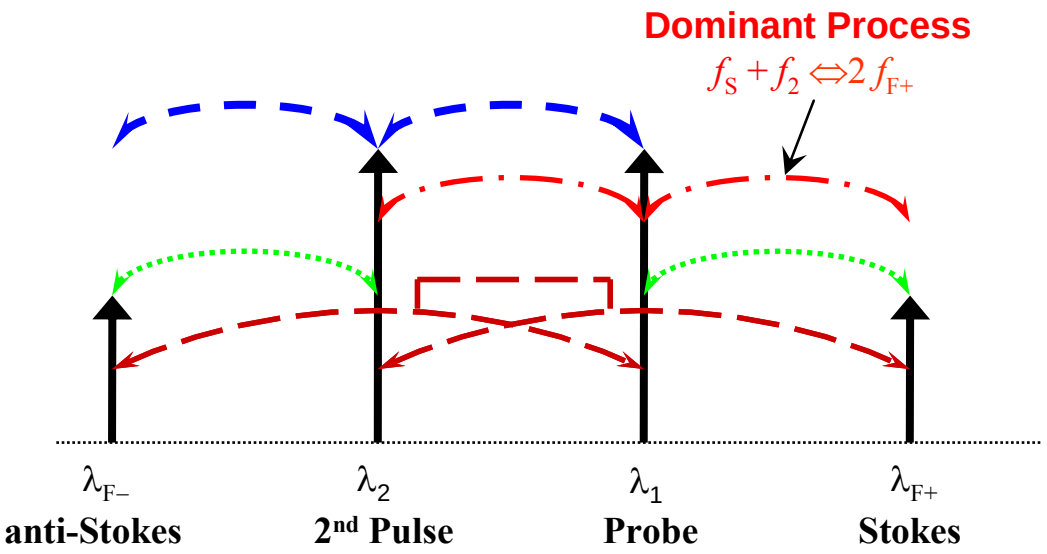

Fig. 21: Signal-probe FPM processes. The dominant (degenerate) process $2f_P \leftrightarrow f_S+f_{F+}$ is indicated by red curve.

The solution of eq. (4.1) requires special consideration, as it is used in the bidirectional counter-colliding power exchange. Specifically, four interacting pulses are represented by a distinct vector representing the total field. The length of the vector depends on HNLF segment length and required spatial resolution. In a typical example used in this research, a 10-nm separation between the probe and pulse required calculation arrays composed of 2×10^5 elements.

A typical length of the HNLF-based device is shorter than the characteristic dispersion distance defined by eq. (1.3.2) [54] and the pulse chirping takes place only at its leading and trailing edges. Therefore, the FPM interaction can be accurately predicted by considering mid-pulse power and integrating the set of coupled quasi-CW equations with linear (4.2) and nonlinear operators (4.9, 4.11). This set of equations (4) was solved numerically to illustrate the spatial evolution of the FPM wave before and after the pump-probe collision instance. Fig. 22 illustrates the collision scanning process by plotting the

evolution of powers and phases for all four observables (signal, probe, Stokes and anti-Stokes FPM waves). The power evolution was defined by the incident signal and probe waves launched with $P_S = 100$ mW and $P_P = 0.5$ mW and centered at 1540 and 1538 nm into a 200-m-long HNLF fiber with $\lambda_0 = 1579$nm, $S_\lambda = 0.025$ ps/nm^2/km, and $\gamma = 25\text{km}^{-1}\text{W}^{-1}$. The gain experienced by the probe wave was 20 dB at each collision instance. While the format chosen to plot Fig. 22 might seem unconventional, it was carefully selected to illustrate the FPM localization of the new measurement method. The plot is segmented into two sections that correspond to wave powers immediately prior to the collision (left of the 200 m mark) and powers measured at the end of the fiber for each collision point (right of the 200 m mark). In absence of any collision, the powers of all four waves at the end of the fiber can be read just left of the 200 m mark ($P_S = 20$dBm, $P_P = -3$ dBm, $P_{F-} = -9$ dBm, $P_{F+} = -31$ dBm). In case of a collision instance at, e.g. $z_C = 100$ m, the power of four waves at the end of the fiber is read right of the 200 m mark ($P_S = 20$ dBm, $P_P = 17$ dBm, $P_{F-} = -1$ dBm, $P_{F+} = 3$ dBm).

Fig. 22 illustrates that the significant growth of the power of FPM sidebands takes place only after probe amplification. Furthermore the abrupt phase change in the FPM tone is also induced at the collision instance and is quantified by the last term of eq. (4.11). Indeed if the localized collision increment for the mixing terms $A_{F+/-}$, (given by $\gamma A_{P/S}^2 A_{S/P} \Delta z$), is considerably larger than the mixing powers *just prior to the collision* their phases are governed by the complex amplitude of the amplified probe pulses.

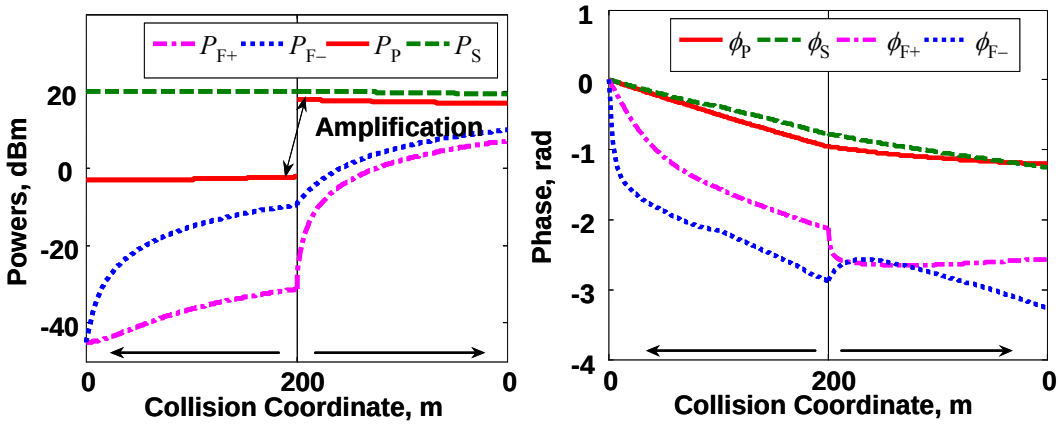

Fig. 22: Power and phase evolution for signal, probe and FPM waves during the collision scanning of a 200-m-long HNLF section. All traces to the right of the 200 m mark correspond to the power/phases at the fiber end; to the left – to the power/phases just prior to the collision point.

The validity of the quasi-CW approximation was verified by solving the time-dependent nonlinear Schrodinger equation describing the counter-collision process. Time-dependent simulations (eq. (4.1)) indicated excellent agreement with the quasi-CW approach described. This agreement is illustrated in Fig. 23, indicating near-vanishing differences for all interacting wave powers. The simulation used launched the probe (P_P = 15 mW, λ_P = 1558 nm), amplified by 20 dB at every collision instance, and the second pulse (P_S = 65 mW, λ_P = 1523 nm) propagated in 250 m of HNLF with λ_0 = 1560 nm, S_λ = 0.026 ps/nm^2/km, and γ = 14.5 km^{-1}W^{-1}.

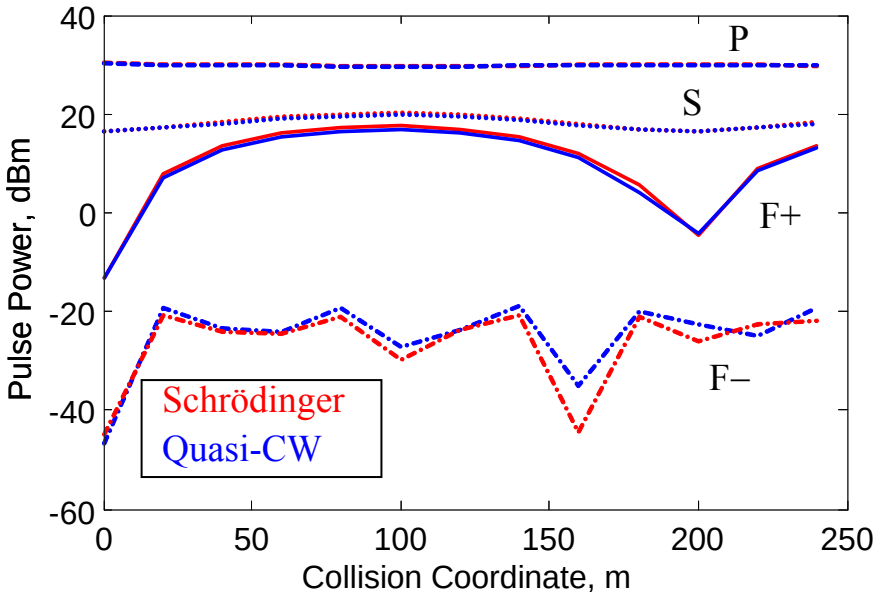

Fig. 23: Powers of the probe P, second pulse S, and FPM sidebands $F_{+/-}$ at the end of the fiber obtained using the integration of the time-dependent Schrödinger and quasi-CW equations.

The rigorous prediction of the evolution of all interacting pulses is provided by the nonlinear Schrödinger equation for the envelope $A(t)$ at a chosen carrier frequency using the standard split-step formalism [55] described in more details in chapter 4.4:

If the power transfer between the probe and the second pulse is negligible before the collision instance (undepleted propagation), the power evolution of the Stokes amplitude A_{F+} is described by:

$$\frac{dA_{F+}}{dz} = \left(-\frac{\alpha}{2} + j\kappa\right) + j\gamma\left[\left(\left|A_{F+}\right|^2 + 2\left(\left|A_P\right|^2 + \left|A_S\right|^2\right)\right)A_{F+} + A_P{}^2 A_S{}^*\right] \qquad (4.14)$$

where A_P and A_S are the amplitudes for the probe centered at f_P, the pulse f_S, and the Stokes wave at $2f_P - f_S$, κ is a linear operator given by (4.2).

Assuming negligible fiber loss, eq. (4.14) can be simplified by using the transformation

$$A_{F+} = B_{F+}\exp\left(j\int_0^z k + j\gamma\left(\left|A_{F+}\right|^2 + 2\left(\left|A_P\right|^2 + \left|A_S\right|^2\right)\right)dz'\right) \qquad (4.15)$$

that allows the FPM evolution to be rewritten in the rotating frame of reference

$$\frac{dB_{F+}}{dz} = j\gamma {B_P}^2 {B_S}^* e^{j\phi(z)} \tag{4.16}$$

In eq. (4.16), the phase term $\phi(z)$ defines total (linear and nonlinear) retardation seen by the FPM wave. A new variable $\phi(z)$ represents the accumulated phase mismatch experienced by the FPM wave. The phase mismatch combines both linear $\kappa_{lin}(z)$ and nonlinear $\kappa_{nl}(z)$ contributions defined as:

$$\phi_{lin}(z) = \int_0^z \Delta\kappa_{lin}(z')dz' \tag{4.17}$$

$$\phi_{nl}(z) = \gamma \int_0^z (2P_P(z') - P_S(z') - P_{F+}(z'))dz' \tag{4.18}$$

The power of the FWM wave at the fiber end can be obtained by integration of equation (4.16)

$$P_{F+}(L) = |B_{F+}|^2 = \left| \int_0^L \gamma {B_P}^2 {B_S}^* e^{j\phi(z)} dz \right|^2 \sim \left| \int_0^L e^{j\int \Delta\beta dz'} dz \right|^2 \tag{4.19}$$

For a constant dispersion profile, the expression for the FWM power is transformed to a classical $sinc^2$-law dependency [58].

As implied by equation (4.18), the 1:2 ratio between the probe (P_P) and the signal (P_S) can be used to minimize the nonlinear contribution to total phase mismatch. By acquiring the power of all four waves at the end of the fiber, it is possible to solve the inverse problem and retrieve the dispersion fluctuation map along the entire fiber length.

4.4 Numerical Integration and Accuracy control

The split-step method (SSM) is usually used to solve parabolic Schrödinger equation (1). According to this technique, a single integration step is replaced by a combination of the steps desribing linear and nonlinear effects independently. Typically, the following symmetrical scheme shown in Fig. 24 is applied. First of all, the step length Δz at every integration step is calculated. Then, the optical field is modified by a liner operator corresponding to the propagation at $\Delta z/2$ calculated in the frequency domain. Subsequently, the nonlinear operator corresponding to the full step Δz in time domain is applied. The Raman terms containing the convolutuon of the propagated fields and Raman response functions are simulated in frequency domain using a convolution theorem. Finally, the linear operator (2) of the second $\Delta z/2$ interval is repeated. The process is continued until the left border of integration is reached. The integration step Δz is usullally selected by specifying the maximum nonlinear phase rotation $\Delta\phi_{\max}$ taking place in this step. i.e.

$$\Delta z(z) = \frac{\Delta\phi_{\max}}{\gamma\, P_{\max}(z)} \tag{4.20}$$

$P_{\max}$ is a maximum total power (in time) of the optical field at coordinate z. The typical $\Delta\phi_{\max}$ providing 0.1-dB-accuracy integration for 1 W signals is less than 0.2°. However, it is worth limiting this step to some reasonable (better random) value if the power of the propagating wave is low. The worst integration strategy is to use the integration grid with constant step size in which case the FWM products can be artificially overestimated [62].

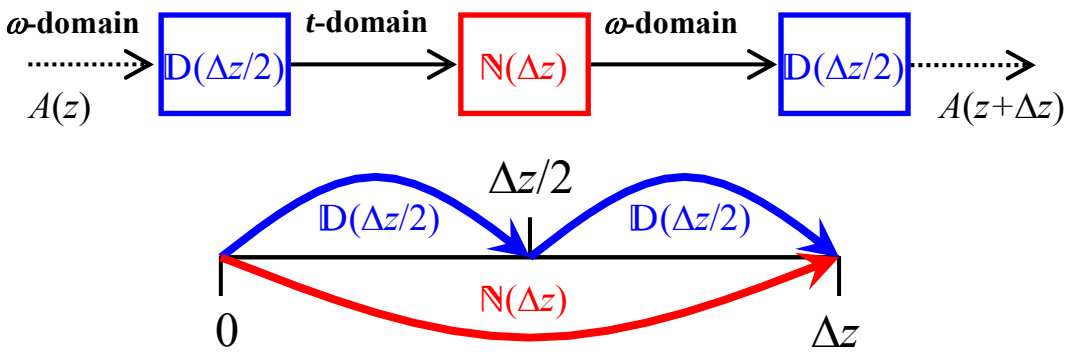

Fig. 24: Schematic representation of the split-step method.

In the previous chapter, it has been proved that the quasi-CW approximation is valid for accurate representation of the pulse evolution used in counter-colliding pulse scheme. It was shown that, if the time dependency is exclused, the partial differential equation (4.1) is transformed to a set of ordinary differential equations for complex quasi-CW waves. The differential equations can be integrated using standard Runge-Kutta technique [64]. However, simulations demonstrated that the standard Runge-Kutta algorithm provides only the first order accuracy for a *set* of differential equations. In order to overcome this difficulty, the split-step method can be adapted. As before, a single integrating step has to be divided into 3 steps. The two linear steps can be integrated accurately using analysical expression for the rotated phase. The nonlinear step can be calculated using predictor-corrector scheme. According to this scheme, if a set of coupled equations $d\vec{Y}/dx = F\left(x,\vec{Y}\right)$ is integrated at *dx*, the solution at right border is first predicted $\vec{Y}^*(x+dx) = \vec{Y}(x) + F\left(x,\vec{Y}(x)\right)dx$, then it is mixed with the original vector to find approximate (averaged) value of the right-hand part of the equation at *dx*, i.e. $F\left(x,\left\langle\vec{Y}\right\rangle\right) = 1/2\left(F\left(x,\vec{Y}(x)\right) + F\left(x,\vec{Y}^*(x+dx)\right)\right)$, and finally the value of the function at

$x+dx$ is calculated $\vec{Y}(x+dx)=\vec{Y}(x)+F\left(x,\left\langle\vec{Y}\right\rangle\right)dx$. Of cause, if only SPM and XPM effects are considered, there exists analytical expression for nonlinear phase rotator and predictor-corrector step is not required.

4.5 Phase Matching Conditions

The linear phase matching factors introduced in (4.17) corresponding to the different dispersion order can be analytically calculated for arbitrary nonlinear process involving four interacting waves. If four distinct waves exchange power by means of FWM process $\omega_1+\omega_3 \leftrightarrow \omega_2+\omega_4$ (i.e. $dA_4/dz \sim A_1A_2^*A_3$), the generalized expression for the phase matching factor is given by

$$\Delta\beta=\sum_{n\geq 2}\frac{\beta_n}{n!}\left[(\omega_1-\omega_{\text{ref}})^n-(\omega_2-\omega_{\text{ref}})^n+(\omega_3-\omega_{\text{ref}})^n-(\omega_4-\omega_{\text{ref}})^n\right]=\\ =\sum_{n\geq 2}\Delta\beta_n \tag{4.21}$$

in which β_n is a dispersion factor defined in Chapter 4.1, ω_{ref} is a frequency at which these coefficients are specified, i.e. $\beta_n=\beta_n(\omega_{\text{ref}})$. The analytical expressions for three lower order phase matching terms can be written as follows:

$$\Delta\beta_2=-\beta_2(\omega_1-\omega_2)(\omega_3-\omega_2) \tag{4.22}$$

$$\Delta\beta_3=-\frac{1}{2}\beta_3(\omega_1-\omega_2)(\omega_3-\omega_2)(\omega_1+\omega_3-2\omega_{\text{ref}}) \tag{4.23}$$

$$\Delta\beta_4=-\frac{1}{12}\beta_4(\omega_1-\omega_2)(\omega_3-\omega_2)\times\\ \times\left[(\omega_1-\omega_3)^2+\left(\omega_2^{\,2}-\omega_2(\omega_1+\omega_3)+\omega_1\omega_3\right)+3(\omega_1-\omega_{\text{ref}})^2+3(\omega_3-\omega_{\text{ref}})^2\right] \tag{4.24}$$

For a degenerate process $2\omega_1 \leftrightarrow \omega_2+\omega_4$ ($\omega_1=\omega_3$), these expressions transform to

$$\Delta\beta_2=-\beta_2(\omega_1-\omega_2)^2 \tag{4.25}$$

$$\Delta\beta_3 = -\beta_3(\omega_1 - \omega_2)^2(\omega_1 - \omega_{\text{ref}}) \tag{4.26}$$

$$\Delta\beta_4 = -\frac{1}{12}\beta_4(\omega_1 - \omega_2)^2\left[(\omega_1 - \omega_2)^2 + 6(\omega_1 - \omega_{\text{ref}})^2\right] \tag{4.27}$$

In practice, the dispersion coefficients β_n are calculated analytically using a polynomial fit of the dispersion profile $D(\lambda)$ measured by dispersion measuring test set. For example, the first three factors are given by (4.28-30). As before, the dispersion D, slope S, and slope derivative $dS/d\lambda$ are specified at specific reference frequency ω_{ref}.

$$\beta_2 = -\frac{\lambda_{\text{ref}}^{\ 2}}{2\pi c}D \tag{4.28}$$

$$\beta_3 = \frac{\lambda_{\text{ref}}^{\ 3}}{(2\pi c)^2}(2D + S\lambda_{\text{ref}}) \tag{4.29}$$

$$\beta_4 = -\frac{\lambda_{\text{ref}}^{\ 4}}{(2\pi c)^2}\left(6D + 6\lambda_{\text{ref}}S + \lambda_{\text{ref}}^{\ 2}\frac{dS}{d\lambda}\right) \tag{4.30}$$

4.6 Modeling of Localized Pulse Amplification

The interaction of two optical waves E_S and E_P propagated in opposite direction and interacting through Brillouin scattering and a complex acoustic wave ρ is described by a set of coupled equations

$$\begin{cases} \dfrac{\partial E_S}{\partial z} + \dfrac{1}{v_g}\dfrac{\partial E_S}{\partial t} = -\dfrac{\alpha}{2}E_S - j\kappa_1\rho E_P \\ \dfrac{\partial E_P}{\partial z} - \dfrac{1}{v_g}\dfrac{\partial E_P}{\partial t} = -\dfrac{\alpha}{2}E_P - j\kappa_1\rho^* E_S \\ \dfrac{\partial \rho}{\partial t} - v_A\dfrac{\partial \rho}{\partial z} = -\dfrac{\Gamma}{2}\rho + j\dfrac{\kappa_2}{A_{\text{eff}}}E_S^* E_P + f_n \end{cases} \tag{4.31}$$

α is the attenuation coefficient, $\kappa_1 = \gamma_e \omega / 2nc\rho_0$, $\kappa_2 = \gamma_e \omega / c^2 v_A$ are the Brillouin coupling coefficients, $\Gamma = \pi \Delta f_B$ – photon decay rate, Δf_B is a SBS gain spectrum FWHM, f_n is the noise source, A_{eff} is a fiber effective area, $4\kappa_1\kappa_2/\Gamma = g_B$ is the Brillouin gain coefficient. The typical values for silica are as follows: electrostrictive constant $\gamma_e = 0.902$, material density $r_0 = 2210$ kg/m^3, velocity of the acoustic wave $v_A = 5960$ m/s.

The equations can be solved using a method of characteristics [65]. The basic idea of the method is to reduce the two-dimensional integration to a single dimension. The integration is performed along characteristic lines (dashed lines in Fig. 25) $z = v_g t$, i.e. the integration steps in time τ and space $h = v_g \tau$ are dependent. The group velocity v_g of the optical field is significantly larger that the velocity of the acoustic wave v_A so that the second term in eq. (4.31) can be neglected. This implies that the acoustic wave evolves in time (vertical lines) whereas the optical waves propagate both in time and space (tilted lines). In a single step, the predictor-corrector integrating scheme described in the previous paragraph can be used.

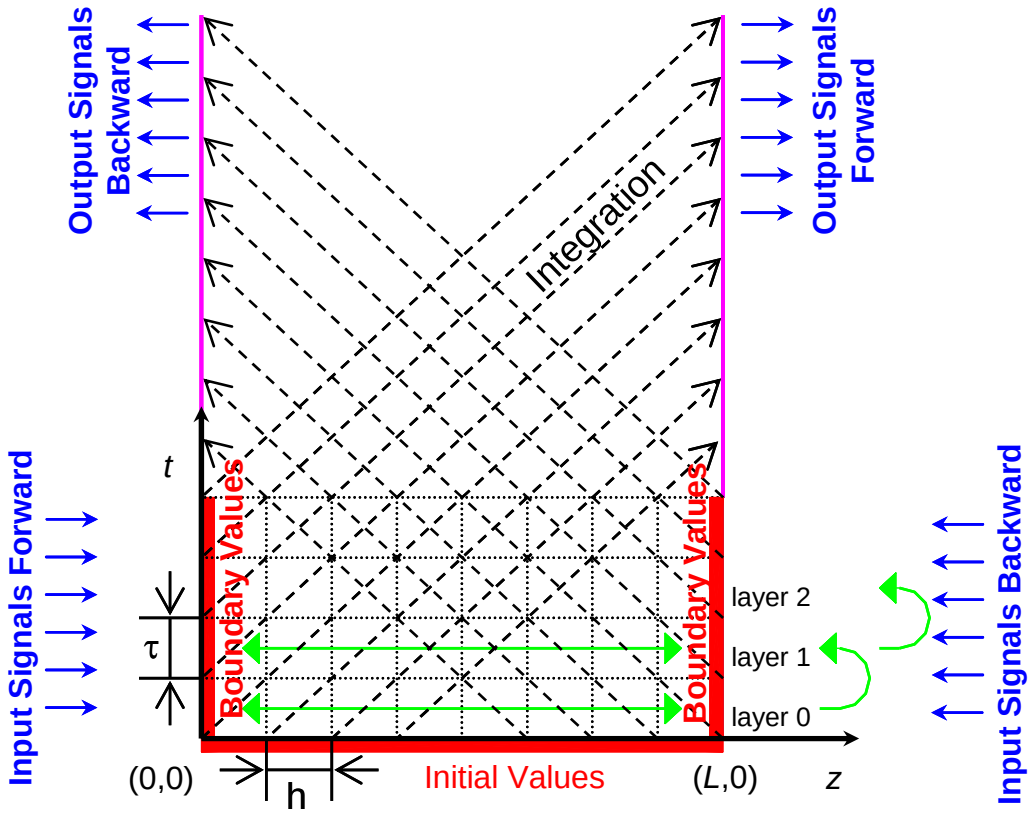

Fig. 25: Schematic representation of the integration algorithm.

Fig. 26 demonstrates the profiles of the 10-ns ideal rectangular probe with 3-dBm-peak input power amplified in HNLF ($\Delta f_B = 50$ MHz, $A_{eff} = 12$ um^2) by 10-ns pumps with peak powers varied in 34–42 dBm range. It is clearly seen that the simulated waveforms are very consistent with the measured ones shown in Fig. 11*b*.

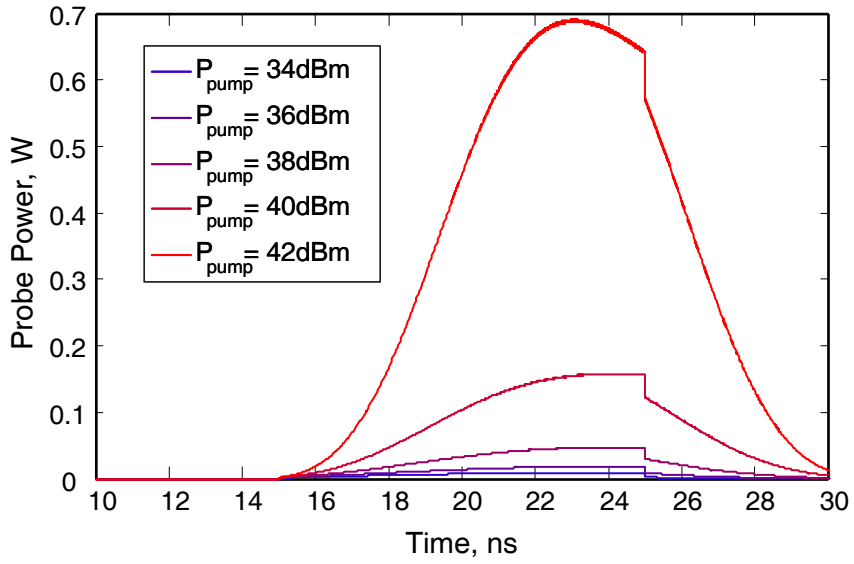

Fig. 26: The profiles of the 10-ns amplified probe.

4.7 Calculation of the Mode Profile and Dispersion Characteristics

The optical properties of the waveguide can be calculated if the transversal refractive index profile $n(r)$ and the material dispersion are known. In the first step of this process, the equation for cylindrically symmetric waveguide [53]

$$\hat{L}E = \frac{\partial}{\partial r}\left(\frac{1}{\varepsilon(r)}\frac{\partial}{\partial r}(\varepsilon(r)E)\right) + \frac{1}{r}\frac{\partial}{\partial r}E - \frac{l^2}{r^2} + \varepsilon(r)k_0^2 E = n_{\text{eff}}^2 k_0^2 E = \lambda E \qquad (4.32)$$

is projected to sufficiently dense discrete spatial grid and converted to the matrix form $L_{ij}E_j = \lambda E_i$. In this expression, the transversal profile of the susceptibility $\varepsilon(r) = n^2(r)$, effective index n_{eff}, and mode profiles E are all functions of wavelength. k_0 is the absolute value of a free-space propagation vector. This formulation allows eq. (4.32) to be transformed to the standard eigenvalue problem governed by the (variable) effective index n_{eff} and the mode profile E_i. From practical point of view, it is advantageous to shift a grid from the origin by half of the discretization step Δ, i.e. $r_{i+1} = (i+1/2)\Delta$. The

boundary conditions at $r = 0$ are dictated by axial symmetry of the radial mode, i.e. $E(r_{1/2}) = E(r_{-1/2})$. At the right boundary, the field at the last point $E(r_{imax})$ can be set either to 0 (zero approximation) or selected considering deterministic exponential depletion of the mode outside the core (transparent border approximation, $E(r_{imax}) = E(r_{imax-1})\cdot e^{-\alpha r}$). In practice, the simulation window should be selected at least ten times larger than the effective core diameter to guarantee significant mode depletion in cladding area. All obtained *real* effective indexes $\{n_{\text{eff}}\}$ lying between the maximum core index and cladding index correspond to the fiber guided modes for a certain azimuthal index l. The propagation index of the fundamental mode has the maximum value among $\{n_{\text{eff}}\}$. The matrix L_{ij} has a tri-diagonal nonsymmetrical form with a dominant diagonal ($|L_{ii}| > |L_{i,i-1}|$, $|L_{i,i+1}|$). Such matrix can be transformed to a *symmetrical* tri-diagonal one L_{ij}* [74] with identical eigenvalues allowing application of fast linear algebra methods, for example, QL algorithm with implicit shifts [72]. The modes E_i (eigenvectors) can be found using a method of inverse iterations [73] which converges extremely fast (typically, 3-5 iterations). The eigenvector of the transformed symmetrical matrix L_{ij}* is a good guess to find the eigenvector of the original matrix L_{ij}. In addition, by applying inverse iterations, the modes and propagation indexes at arbitrary frequencies can be obtained if they are calculated at some nearest frequency. Such strategy makes mode and dispersion analysis very fast. The overlap integrals $A_{ik} = A(f_i, f_k)$ of the interacting modes at different frequencies defined in eq. (8) can be calculated by integrating the obtained mode profiles

$$A_{ik} = \frac{\left(\int\int |E_i(x,y)|^2\, dxdy\right)\left(\int\int |E_k(x,y)|^2\, dxdy\right)}{\int\int |E_i(x,y)|^2 |E_k(x,y)|^2\, dxdy} \qquad (4.33)$$

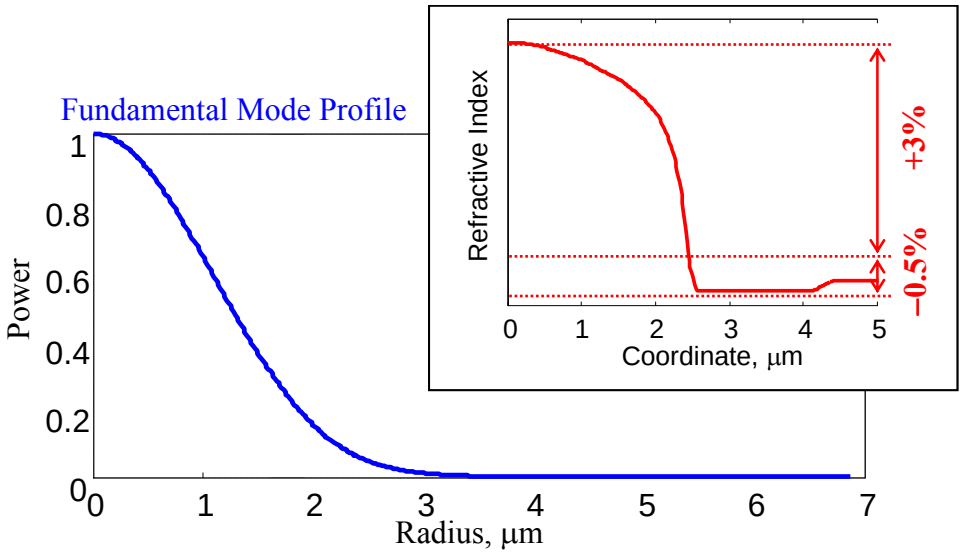

Fig. 27: The simulated fundamental mode profile of the HNLF at λ_0 = 1560 nm [24].

Fig. 27 demonstrates the mode profile for highly nonlinear fiber with zero dispersion wavelength of 1562 nm calculated using a transversal refractive index profile obtained from fiber manufacturer. The wavelength dependencies for dispersion, slope, and effective area for this fiber and a fiber with ±1 perturbed geometry are shown in Fig. 2 and Fig. 28. As seen from Fig. 28, slope and effective area, in contrast to dispersion, are almost insensitive to variations of fiber geometry. This implies that the slope and nonlinear coefficient used in the inverse dispersion solver can be approximated by some average values. The later fact significantly simplifies the numerical complexity of the dispersion retrieving solver.

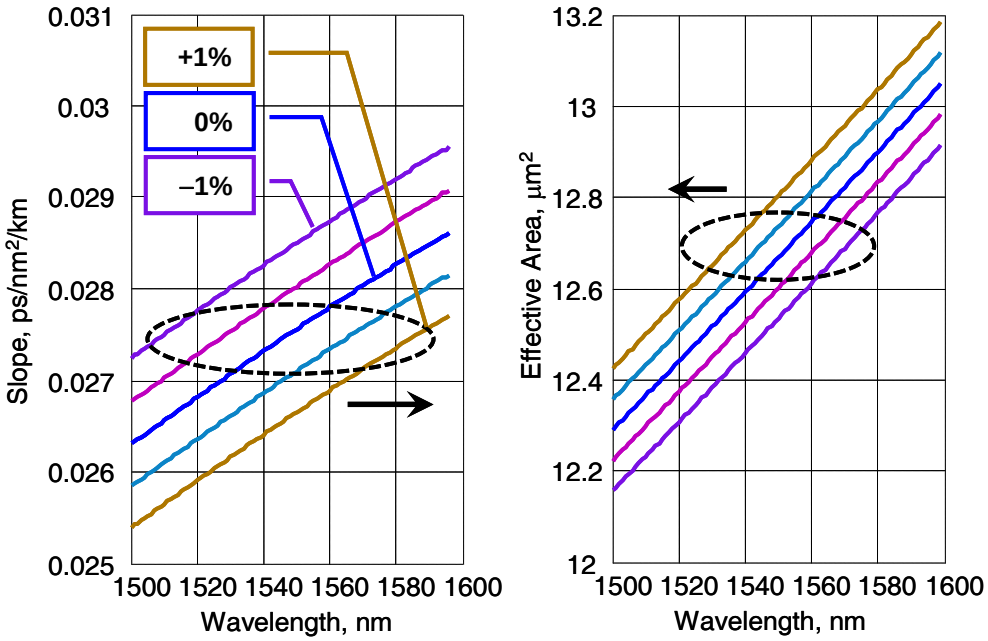

Fig. 28: HNLF dispersion slope and effective area sensitivity to transversal profile perturbation. Reference (unperturbed) waveguide designed for $\lambda_0 = 1560$ nm; the core radius perturbed by ±0.5% and 1%.

5. Inverse Dispersion Retrieval

In this thesis, three distinct paths leading to the inverse problem solution will be introduced. The first two methods utilize the approximation in which the evolution of propagated pumps is deterministic assuming that the effect of the generated FWM sidebands on strong waves is negligible. This simplification allows creating very illustrative graphical constructions (trajectories) in phase space. In the last approach, the experimentally obtained power profiles are fitted by numerical ones by optimizing spatial dispersion map.

As discussed in chapter 4.2, using of the quasi-CW approximation instead of solving time-dependent nonlinear Schrödinger equation for long (>1 ns) interacting pulses simplifies the numerical analysis significantly. The validity of this approach was verified by numerical simulations. The observables of the counter-colliding scanning measurement are the measured waveforms of the probe, pump, and Stokes waves acquired at the end of the fiber and probe gain at collision instance. Following the quasi-CW notation, one is ready to consider solving the inverse problem and retrieve the dispersion fluctuation map using the signal levels sampled in the middle part of the pulse.

5.1 Geometrical Method for Dispersion Retrieval

The geometrical approach is based on a simple notion that the amplitudes of the FPM products could be represented by the vectors in the complex (phase) space.

Propagation along HNLF simply elongates the vector and rotates it according to the accumulated (linear and nonlinear) phase retardation that the wave experiences. The evolution of the vectors is fully described by elemental increments defined by RHS of the following equation.

$$\frac{dB_{F+}}{dz} = j\gamma B_P{}^2 B_S{}^* e^{j\phi(z)} \tag{5.1}$$

i.e. the entire propagation and discrete collision process simply becomes the vector summation problem. B_P, B_S, and B_{F+} are the amplitudes for the probe centered at f_P, the pulse at f_S, and the Stokes wave at $2f_P - f_S$ specified in rotating frame.

To construct the geometrical solution more formally, assume that the FPM wave propagates from the beginning of the fiber up to some point z_C, with $\boldsymbol{B}_0 = \boldsymbol{r}_0$ representing its accumulated complex amplitude. Two distinct cases can be identified: in the first one, the probe is amplified at z_C; in the second one – the probe is amplified at the nearest resolvable point $z_C + dz_C$. Let $\boldsymbol{R}$ and $\boldsymbol{r}$ be the FPM amplitudes measured at the fiber end, corresponding to the collision at z_C and $z_C + dz_C$ respectively, and $\boldsymbol{R}_\Sigma$ and $\boldsymbol{r}_\Sigma$ be the FPM amplitudes accumulated after $z_C + dz_C$:

$$\begin{aligned} \boldsymbol{R}_\Sigma &= \gamma \int_{z_C+dz_C}^{L} B_P{}^2 B_S{}^* e^{\phi(z')} dz' \\ \boldsymbol{r}_\Sigma &= \gamma \int_{z_C+dz_C}^{L} B_P{}^2 B_S{}^* e^{\phi(z')} dz' \times e^{j\delta\phi(z)} \end{aligned} \tag{5.2}$$

For the undepleted case, their absolute values are equal, i.e. $|\boldsymbol{R}_\Sigma| = |\boldsymbol{r}_\Sigma| = \Sigma$ because the RHS of eq. (5.2) is identical except the constant phase factor $\delta\phi$. Let $\boldsymbol{e}_{R\Sigma}$ and $\boldsymbol{e}_{r\Sigma}$ be directional unit vectors for $\boldsymbol{R}_\Sigma$ and $\boldsymbol{r}_\Sigma$ ($\boldsymbol{R}_\Sigma = \Sigma \boldsymbol{e}_{R\Sigma}$, $\boldsymbol{r}_\Sigma = \Sigma \boldsymbol{e}_{r\Sigma}$) and Δ_1 and δ_1 be the

increments to amplitudes R and r during the collision interval $[z_C, z_C+dz_C]$. A schematic diagram of the vector collision description is shown in Fig. 29.

According to eq. (5.1), the angle between vector $\boldsymbol{r}_0$ and $\boldsymbol{\Delta}_1$ corresponds to the phase mismatch at point z_C corrected by finite increment $(\Delta\kappa_{lin}(z_C)+\Delta\kappa_{NL}^{(AC)}(z_C))dz_C$. By analogy, the angle between vector $\boldsymbol{r}_0$ and $\boldsymbol{\delta}_1$ is a phase mismatch at point z_C corrected by $(\Delta\kappa_{lin}+\Delta\kappa_{NL}^{(BC)}(z_C))dz_C$. Correspondingly, the angle between vectors $\boldsymbol{\Delta}_1$ and $\boldsymbol{\delta}_1$ is given only by collision nonlinear phase shift $\alpha = 2\gamma(P_1^{(AC)}-P_1^{(BC)})dz_C$. Finally, the angle between the vectors $\boldsymbol{R}_\Sigma$ and $\boldsymbol{r}_\Sigma$ is also α ($\boldsymbol{e}_{R\Sigma}\cdot\boldsymbol{e}_{r\Sigma} = \cos\alpha$) since the increments and rotation angles after z_C+dz_C are identical.

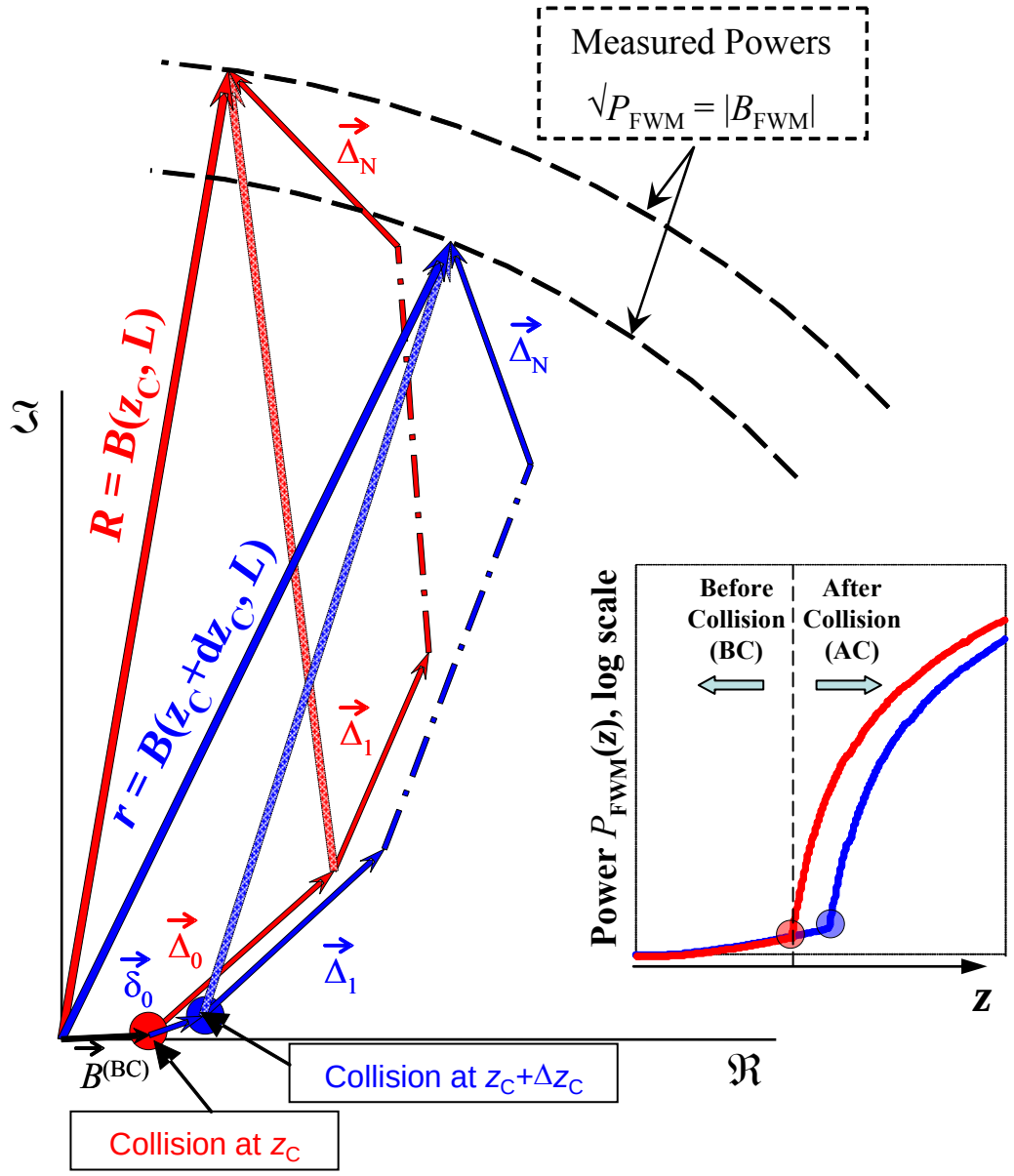

Fig. 29: Vector representation of the evolution of FPM waves.

The geometrical interpretation of FPM evolution can now be formalized in the flowing set of equations:

$$\begin{cases} \boldsymbol{R} = \boldsymbol{r}_0 + \boldsymbol{\Delta}_1 + \Sigma \boldsymbol{e}_{R_\Sigma} \\ \boldsymbol{r} = \boldsymbol{r}_0 + \boldsymbol{\delta}_1 + \Sigma \boldsymbol{e}_{r_\Sigma} \\ \boldsymbol{e}_{R_\Sigma} \cdot \boldsymbol{e}_{r_\Sigma} = \cos\alpha \\ \boldsymbol{e}_{\Delta_1} \cdot \boldsymbol{e}_{\delta_1} = \cos\alpha \end{cases} \tag{5.3}$$

Decomposition of eq. (5.3) to the vector $\boldsymbol{r}_0$ and its perpendicular generates a set of four transcendental equations with 6 unknowns. The number of equations is reduced to 4 for collision points at the beginning and at the end of the fiber.

If the powers of the FPM products before the collision are negligible, i.e. $\boldsymbol{r}_0$ and $\boldsymbol{\delta}_1$ are zero-length vectors, the analysis is significantly simplified as the vectors corresponding to the amplitudes for two consecutive collision points and the vector $\boldsymbol{\Delta}_1$ create a simple triangle in this case.

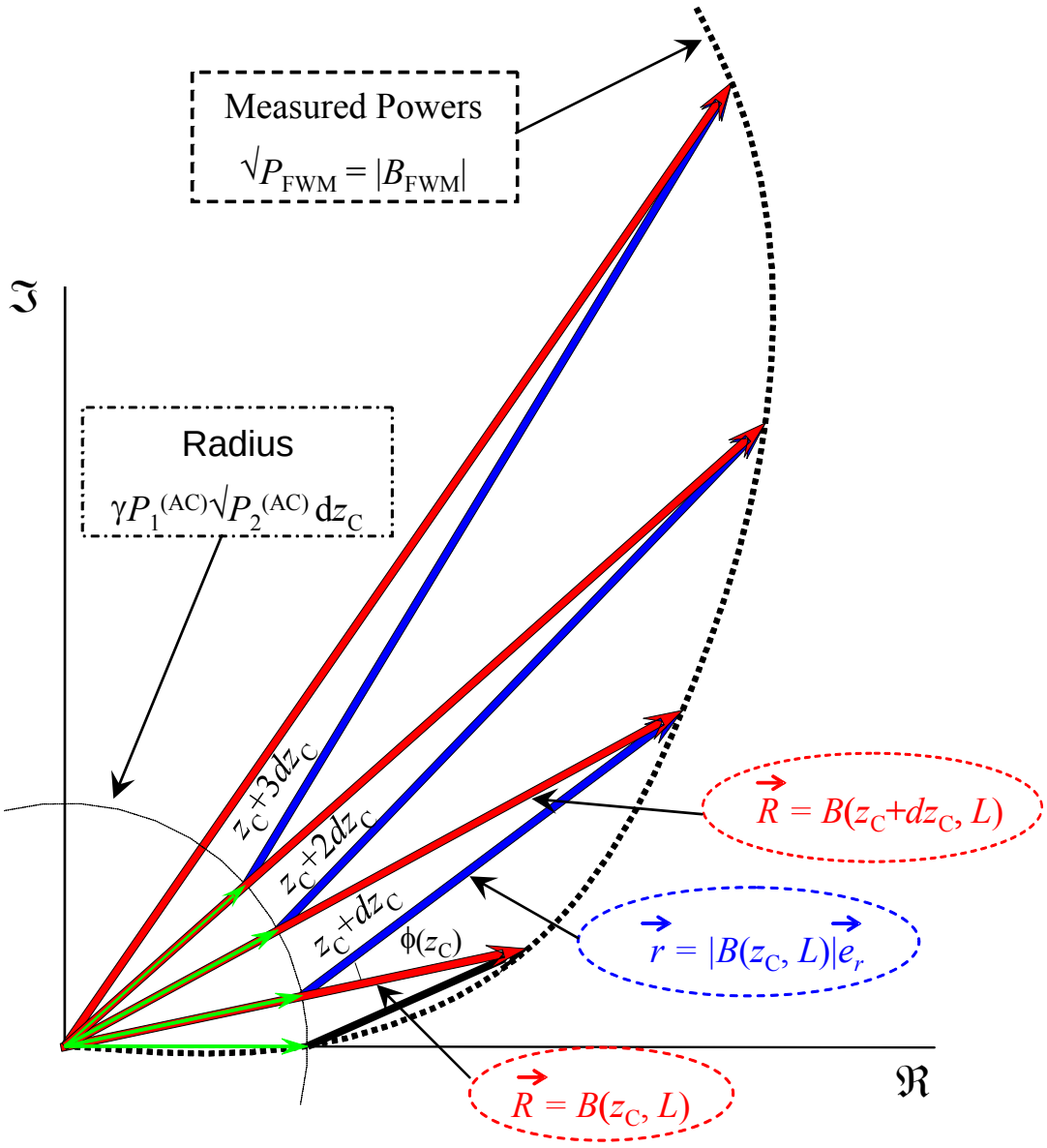

Fig. 30: Vector representation of the evolution of FPM products assuming zero mixing power before the collision instance.

To illustrate this important observation, the incremental vector Δ_i can be plotted within one circle of radius Δ, as illustrated in Fig. 30. Fig. 31 finally reduces the task of dispersion retrieval to a trivial geometrical problem: the outer angle is the local phase mismatch and is calculated by cosine theorem:

$$\phi(z_C) = \pi - \operatorname{acos}\left(\frac{R^2 - r^2 - \Delta^2}{2|r||\Delta|}\right) \tag{5.4}$$

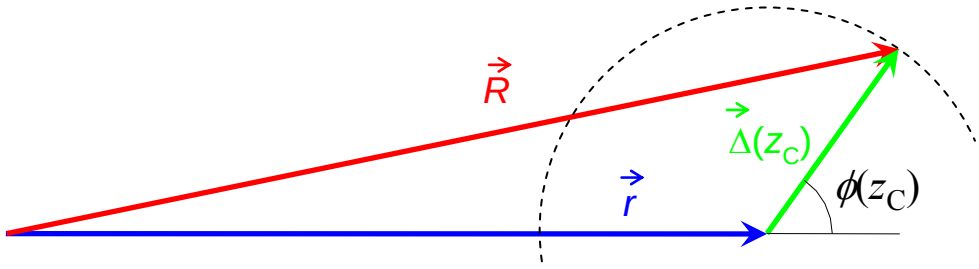

Fig. 31: A triangle formed by vectors of complex amplitudes of the FWM product referred to the collisions at some nearest points.

Local phase mismatch, in turn, defines the local linear propagation difference, and correspondingly, the dispersion profile via the simple relation:

$$\Delta\kappa_{\text{lin}} = \frac{d\phi_{\text{lin}}(z_C)}{dz_C} \tag{5.5}$$

By consecutively applying the geometrical solution to all collision instances, the entire dispersion fluctuation map is retrieved.

5.2 Dispersion Retrieval Using Finite Difference Approximation

By separating the amplitude and phase, eq. (4.16) can be transformed to:

$$\frac{d\sqrt{P_{F+}}}{dz} = \gamma P_P \sqrt{P_S}\sin\phi(z) \tag{5.6}$$

Integrating the last relation, it is possible to express the absolute value of the Stokes amplitude at the end of the fiber as:

$$\begin{aligned}\sqrt{P_{F+}}(z_C, L) = \gamma\Bigg[&\int_0^{z_C} P_P^{(BC)}\sqrt{P_S^{(BC)}}\sin\phi(z')dz' \\ &+ \int_{z_C}^{L} P_P^{(AC)}\sqrt{P_S^{(AC)}}\sin\phi(z')dz'\Bigg] = \Phi(z_C)\end{aligned} \tag{5.7}$$

Eq. (5.7) implies that the generation of the FPM wave is aided by the pump-probe collision at z_C that delivers abrupt power increase to the probe pulse. The separate subscripts BC and AC correspond to the wave evolution (B)efore and (A)fter the (C)ollision instance. Using a straightforward algebraic approach, it is easy to differentiate equation $\Phi(z_C)$ with respect to the collision coordinate z_C and calculate $\phi(z_C)$ by assuming the undepleted pump approximation. The difference relation following from this procedure is given by:

$$\begin{aligned}&\sqrt{P_{F+}\left(z_C+dz_C,L\right)}-\sqrt{P_{F+}\left(z_C,L\right)}=\\&=\left(\Delta-\delta\right)\left[\sin\phi+\frac{1}{1/G-1}\left\{\frac{\partial\phi}{\partial z_C}\right\}\int_{z_C}^{L}\cos\phi dz\right]\end{aligned} \tag{5.8}$$

where G indicates the abrupt gain experienced by the probe pulse at the collision point z_C. The newly defined variables Δ and δ are given by:

$$\begin{aligned}\Delta&=\gamma P_P^{(AC)}\sqrt{P_S^{(AC)}}dz_C\\\delta&=\gamma P_P^{(BC)}\sqrt{P_S^{(BC)}}dz_C\end{aligned} \tag{5.9}$$

and represent the absolute values of the amplitude increments before and after the collision instances. The term $(\partial\phi/\partial z_C)$ in eq. (5.8) is the derivative of the total accumulated phase at the collision point with respect to collision coordinate defined by:

$$\begin{aligned}&\frac{\partial\phi}{\partial z_C}=\left(\kappa_{nl}^{(BC)}-\kappa_{nl}^{(AC)}\right)\approx\\&\approx\gamma\left(\left(2P_P^{(BC)}-P_S^{(BC)}\right)-\left(2P_P^{(AC)}-P_S^{(AC)}\right)\right)\end{aligned} \tag{5.10}$$

It should be noted that linear terms do not present in (5.10) because linear phase mismatch is a deterministic (although unknown) value independent on collision coordinate.

A significant insight is gained by noting that RHS of eq. (5.10) is composed out of two distinct parts: the first one unifies the information about pre-collision propagation and the phase at collision instance, while the second (integral) term describes the difference in the Stokes powers accumulated after collision due to different initial phase relations at z_C and z_C+dz_C points. The value of the accumulated phase can be found using the iterative procedure:

$$\sin\phi^{[j+1]} = \frac{\sqrt{P_{F+}(z_C + dz_C, L)} - \sqrt{P_{F+}(z_C, L)}}{(\Delta - \delta)} - \\ - \frac{1}{1/G - 1}\left\{\frac{\partial\phi}{\partial z_C}\right\}\int_{z_C}^{L}\cos\phi^{[j]}dz \tag{5.11}$$

In the initial iteration, the simplest solution can be chosen by setting the second term of RHS of eq. (5.11) to zero. The algorithm then proceeds and can be stabilized by dampening the phase guess the at consecutive iterations, $\phi^{[j+1]} = \varepsilon\phi^{[j]}+(1-\varepsilon)\phi^{[j+1]}$ in which ε is the (empirical) stabilization factor ($0 < \varepsilon < 1$). Finally, difference process reconstructs the entire phase evolution and leads to dispersion fluctuation retrieval.

5.3 Accuracy of Dispersion Retrieval Algorithms and Uniqueness of Dispersion Fluctuation Map Solution

The basic property of any algorithm is its tolerance to a variation of the input parameters that still provide acceptable accuracy in calculating the target physical quantity. We adopted the simulate-then-retrieve strategy in order to gauge the accuracy of any dispersion retrieval algorithm. At first stage, randomly generated dispersion fluctuation map $D_{gen}(z)$ was used to calculate all observable parameters $P(z_C)$ within the counter-collision scanner system. Then, these powers were used as input parameters to

the inverse solver; consequently the inverse solution $D_{gen}(z)$ is compared to the original (randomly generated) dispersion map. We refer to the front end of this algorithm testing construct as a synthesizer (as it mimics observables in the experimental setup), and the inverse solver as an analyzer (as it analyzes the provided observables).

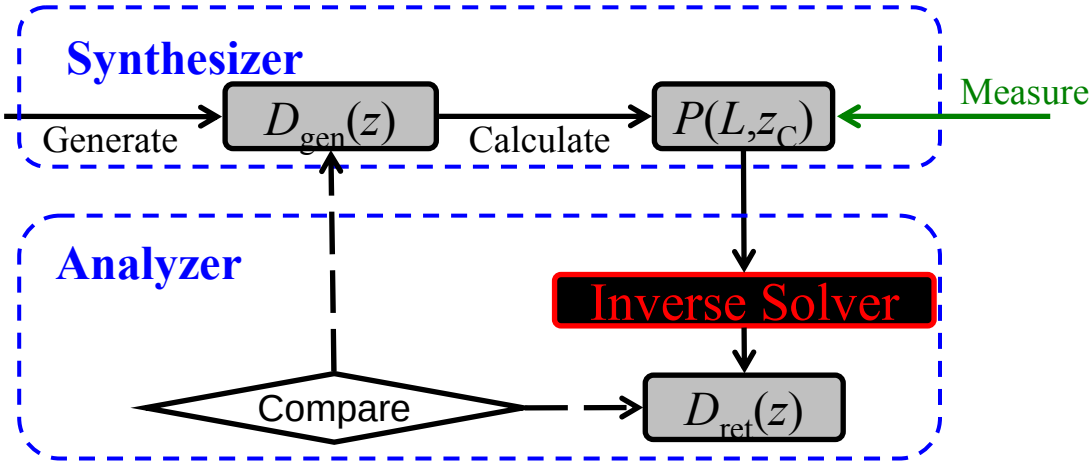

Fig. 32: Schematic representation of the simulate-and-retrieve strategy.

Following proposed strategy, in order to verify the applicability of the introduced methods, the set of equations (4.9, 4.11) is integrated numerically for consecutive collision instances using the dispersion profile generated by randomly weighed four Fourier spatial harmonics, as shown in Fig. 33, and represents the synthesizer block. The output power profiles from the synthesizer are processed by the analyzer using the finite difference and geometrical approaches described in sections 5.1 and 5.2.

Both algorithms exhibit comparable tolerances to the variation of the input parameters within certain operational regimes, which is not surprising because these algorithms use similar physical principles. More specifically, in the case of low signal/probe peak power (<10 mW) and high gain, (>20 dB), the accuracy of the dispersion retrieval algorithms is satisfactory, as shown in Fig. 33*a*. The discrepancies

between the two methods depend on the initial phase of input signals and are pronounced at the collision points close to the end of the fiber where the rapid increase of the FPM sideband power takes place.

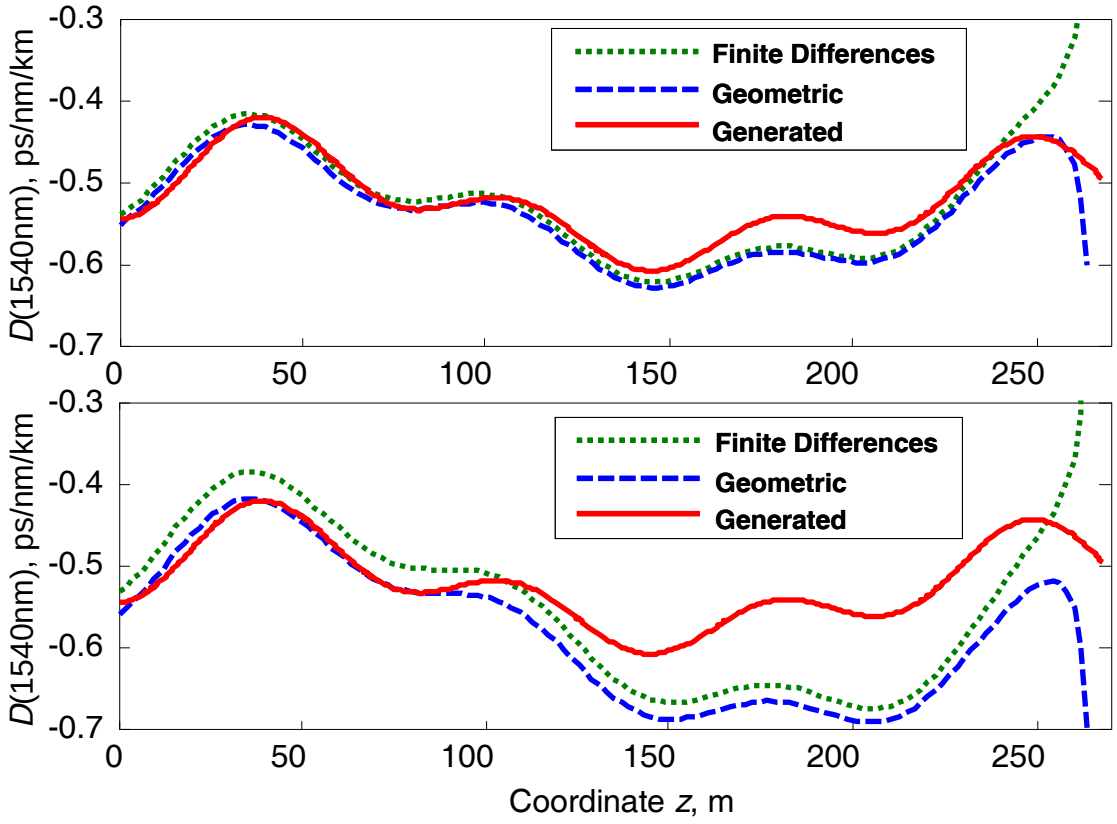

Fig. 33: Dispersion profiles at 1540 nm: generated (exact), inverse solution retrieved by algebraic (finite-difference) and geometrical methods. *a*) $P_P = 0.02$ mW, $P_S = 20$ mW, *b*) $P_P = 0.05$ mW, $P_S = 50$ mW, $\gamma = 14.5$ m^{-1}W^{-1}, fiber length $L = 270$ m, gain $G = 27$ dB.

Fig. 33*b* demonstrates that both methods overestimate the dispersion and add some tilt to spatial profile in the case when the pulse powers are increased beyond a certain limit (from 20 to 50 mW). In this operating regime, the accuracy cannot be improved by increasing the density of the collision grid (or, equivalently, by decreasing the integration step) which means that the other physical effects such as pump depletion cannot be neglected. As seen from Fig. 33*b*, the maximum tilt is attributed to the

collisions taking place close to the fiber end and corresponding to longer propagation distances the amplified pulses.

However, the combination of high gain and low optical signal to noise ratio (OSNR) of the FPM pulses pose a real challenge in the counter-colliding scanner implementation. In practical terms, for signal powers below 10 dBm, low FPM powers are generated even in high-confinement HNLF sections. In the ideal (phase matched) case, a simple estimation from eq. (5.6) for maximum (peak) power of Stokes wave results in $P_{F+} = -14$ dBm for 300-m-long fiber with $\gamma = 15$ km^{-1}W^{-1}, $P_P = 10$ dBm and $P_S = 13$ dBm, thus requiring a low-noise detection scheme.

The limited range of input parameters accepted by both the geometrical and finite-difference inverse solvers motivates a different approach less sensitive to signal/probe power and gain variances.

5.4 Dispersion Retrieval by Minimization

Both geometrical and finite-difference inverse solvers used a set of approximations that ultimately limited the range of their applicability. In an alternative approach, one can take a different position: since complete FPM and collision physics can be described accurately for any dispersion fluctuation map, these calculations should be repeated until the desired accuracy of matching of experimental and simulated observables is reached. The physical insight is exchanged for an intense computational search required to find the unique dispersion profile that, when used to calculate all observables, will produce required-accuracy match. This approach essentially considers a fiber as a “black box” with known input and output signals, as illustrated in Fig. 34.

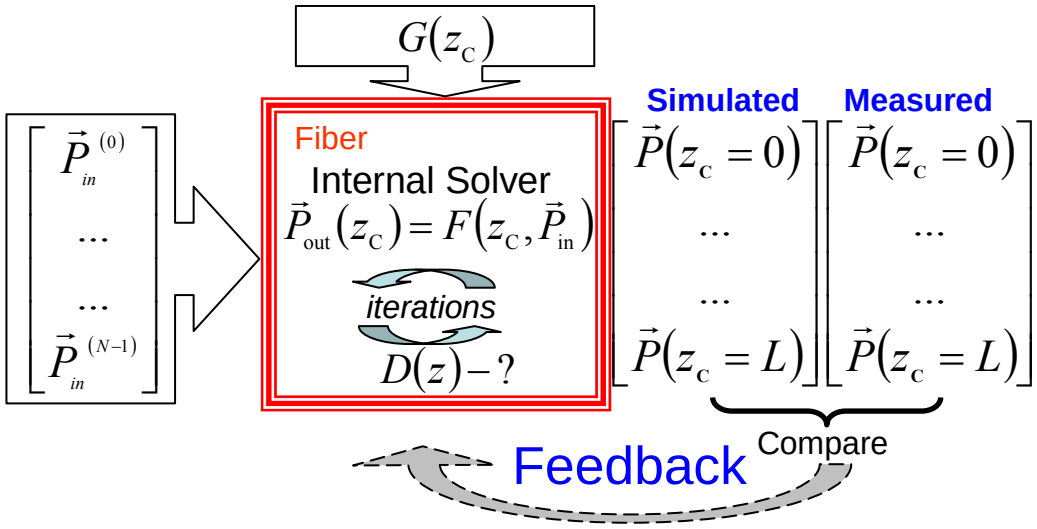

Fig. 34: A schematic diagram of black-box inverse approach.

The unknown characteristic of the fiber is its dispersion profile that is found following a simple concept. Target fiber maps measured input pulse powers to its output using the internal numerical algorithm (propagator), described by a set of equations

$$\boldsymbol{P}_{out}(z_{Cj}, L) = \Phi(\boldsymbol{P}_{in}, z_{Cj}, \boldsymbol{D}) \;, j = 1 \ldots N \qquad (5.12)$$

in which $P_{out}(z_{Cj}, L)$ represents a vector of output powers (P_P, P_S, P_{F+}, P_{F-}) corresponding to collision at z_{Cj}, $\boldsymbol{P}_{in}$ is a vector of input powers, N is the total number of measured points, Φ is a function-propagator described by eq. (4.9, 4.11), and $\boldsymbol{D}$ is the unknown dispersion fluctuation map. The simulated powers are compared to the measured ones to generate a specific feedback to the algorithm, which is used to update the calculated dispersion profile in iterative manner applying chosen minimization algorithm. A metric ε used in simulations

$$\varepsilon = \sum_j \left| \boldsymbol{P}_{measured}(z_{Cj}) - \boldsymbol{P}_{simulated}(z_{Cj}) \right|^2 \Big/ N \qquad (5.13)$$

is a geometrically averaged difference between measured and simulated profiles specified in logarithmic units.

In real fiber, the dispersion varies continuously, i.e. there is a significant spatial correlation along its length, justifying the expansion of function $D(z)$ in terms of some basis functions $f_k(z)$ weighed by d_k:

$$\boldsymbol{D} = D(z) = \sum d_k f_k(z) = \boldsymbol{d} \cdot \boldsymbol{f} \tag{5.14}$$

The simplest choice for $f_k(z)$ is a set of Fourier harmonics or some orthogonal polynomials.

The minimization methods [75] of choice can be divided into two basic groups: *a*) the first class (conjugate gradient, quasi-Newton and similar) is based on the search in multidimensional space by making steps along some optimized direction, calculated mainly using the information of local gradient, *b*) the second class (direction set, simplex, genetic algorithms) is based on evaluation of eq. (5.12) along different directions in *N*-dimensional *D*-space and selection of "best"/elimination of "worst" trials.

The criterion of the method convergence depends on the applied optimization algorithm. For the methods from the first group, the simulations can be stopped if the relative metric difference

$$\eta_1 = \frac{\left|\varepsilon^{[i+1]} - \varepsilon^{[i]}\right|}{1/2\left(\left|\varepsilon^{[i+1]}\right| + \left|\varepsilon^{[i]}\right|\right)} \tag{5.15}$$

between two consecutive iterations is below some small factor (say 10^{-4}). For the second group, the criterion (5.15) can be enhanced by additional requirement of small difference between maximum and minimum metric

$$\eta_2 = \frac{\left|\varepsilon^{[i]}{}_{\max} - \varepsilon^{[i]}{}_{\min}\right|}{1/2\left(\left|\varepsilon^{[i]}{}_{\max}\right| + \left|\varepsilon^{[i]}{}_{\min}\right|\right)} \tag{5.16}$$

for a set of directions or points processed at every iteration.

Simulations demonstrated that all of the methods are capable of perfect retrieving numerically synthesized dispersion profile. For measured data that inherently possesses built-in uncertainty, the situation was more complicated: the main problem was the stability of the algorithm to the initial guess and the ability to converge to the global extremum. The methods based on gradients demonstrated the worst performance, converging only if the initial guess was close to the global minimum. In case of a distant initial guess, the solution vector ***D*** varied significantly, converging to some local minimum, not necessarily related to a physical solution. Direction set method was almost insensitive to the initial guess since multiple linearly independent directions were simultaneously tried, but converged in a slow manner.

While not providing elegance, the optimization approach proved itself to be a "working method" for most practical cases. More importantly, approximations such as pump non-depletion were not required and the measured power profiles were successfully used without pre-processing (scaling and smoothing).

The resolution of the presented method is defined by both considered physical effects and numerical algorithm. Likewise Mollenauer's method [34] (eq. (1.2)), the rough estimation of the average zero dispersion wavelength results from the measuring of the period of FWM oscillation. A minimally resolved spatial cell is limited by collision interval. The mathematical resolution is defined by the primitive period of the basis function (5.14). The fundamental limitation is imposed from the fact that the evolution of

FWM sidebands is driven by periodic function of local phase mismatch proportional, at the same time, to integrated fiber dispersion (see equation (4.19)). However, integration of some function implies averaging and smoothing. In proposed method all measured points are considered, in which case the definitive characteristic becomes the sensitivity of the observable characteristics even to small variations in dispersion profiles. The preferable behavior is when small deviations of dispersion profile are converted to significant deviations in power traces, but these deviations have to be resolved by measuring technique. Practically, they should be more than 0.5 dBm. The high sensitivity mode can be obtained by correct positioning of the wavelength of interacting pulses relatively to zero dispersion wavelength (ZDW) and selecting peak powers, as described in section 3.7 and 3.8.

The 268-m HNLF sample with mean ZDW of 1560.5 nm, dispersion slope of 0.025 ps/nm^2/km and deviation σ_λ less than 3 nm was scanned by two co-propagating 10-ns pulses positioned at λ_1 = 1558.23 nm and λ_2 = 1530.23 nm and a counter-propagating 10-ns pump. The corresponding FWM tone is located at 1587.3 nm. Fig. 35 illustrates the measured and converged (calculated) power profiles obtained by the metric minimization algorithm. The averaged Stokes product mean-squared deviation between the measured and calculated values (upon algorithm conversion) was less than 1 dB across the entire fiber collision scan.

The fiber was cut into 50-m long segments and global ZDW of each section was measured by FWM method and noise injection method [50] for blue and red pump, providing only 50-m spatial resolution. Fig. 35 shows that a good agreement was found between standard (destructive) and new counter-colliding techniques for

$\gamma = 16.8\ \mathrm{W^{-1}km^{-1}}$. The dispersion profile was reconstructed using Powell's method with relative metric tolerance η_1 of 10^{-3} [76].

The input powers of the co-propagated probe and second pulse were 30 mW and 58 mW, respectively, throughout the collision scan. The SBS collision gain varied from 25 dB at the end of the fiber to 15 dB at the fiber input. Gain depletion was fully accounted for in the algorithm implementation. While the pump power, as well as the gain at the last fiber section, could have been increased beyond the reported values, the pulse destruction became evident. The convergence of the inverse algorithm is illustrated in Fig. 36: the simulated Stokes power profile converged to a measured one, with an initial guess defined by the constant dispersion corresponding to the average ZDW. The dispersion profiles were calculated using thirteen-harmonic decomposition.

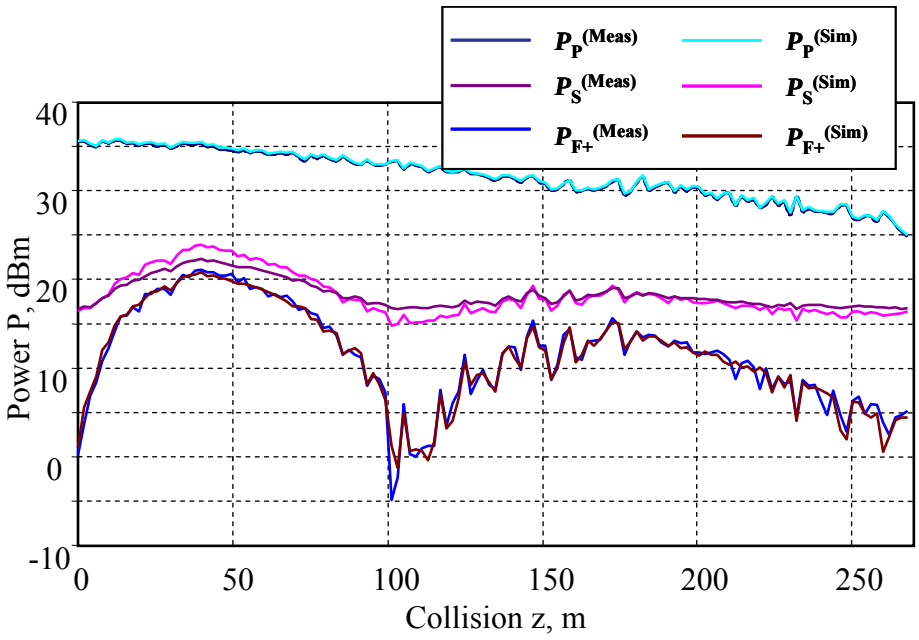

Fig. 35: Measured and calculated powers of propagated pulses 268-m HNLF sample.

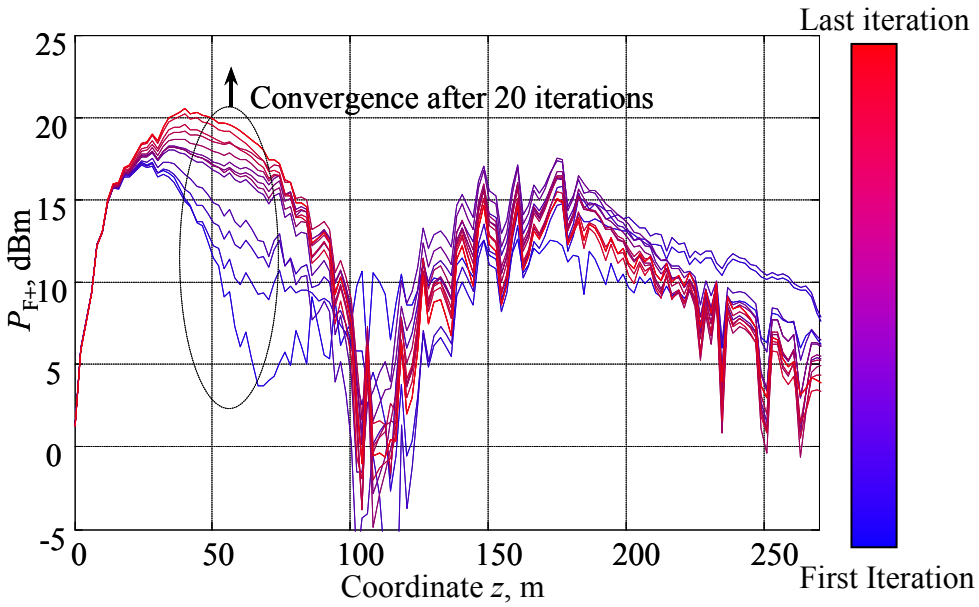

Fig. 36: Convergence of the Stokes power.

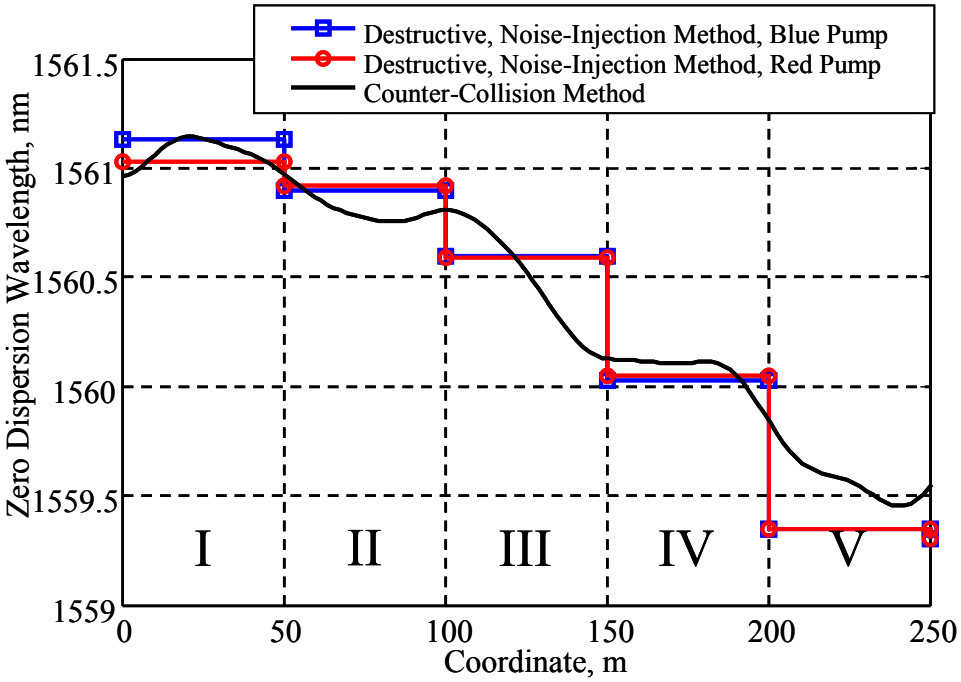

Fig. 37: Comparison between destructive measurement and the counter-collision mapping technique: red and blue lines show average dispersion profiles of five 50-m long sections obtained using a noise injection method for red- and blue-shifted probes, black line corresponds to a dispersion profile recovered after convergence of the numerical algorithm.

The second 175-m HNLF sample with ZDW of 1562.5 nm and slope of 0.025 ps/nm^2/km was scanned with the SBS gain below 15 dB. Such regime provides the equalized gain along the fiber coordinate and, correspondingly, smoother measured traces, as clearly seen form Fig. 38. In order to keep the minimum measured power of the FWM product above −10 dBm, the power of the second pulse was increased up to 27 dBm, which is at least ten times higher than that used in the previous measurement. The new configuration also allowed the equalized powers of the probe and the second pulse and elimination the nonlinear phase mismatch defined by (4.18).

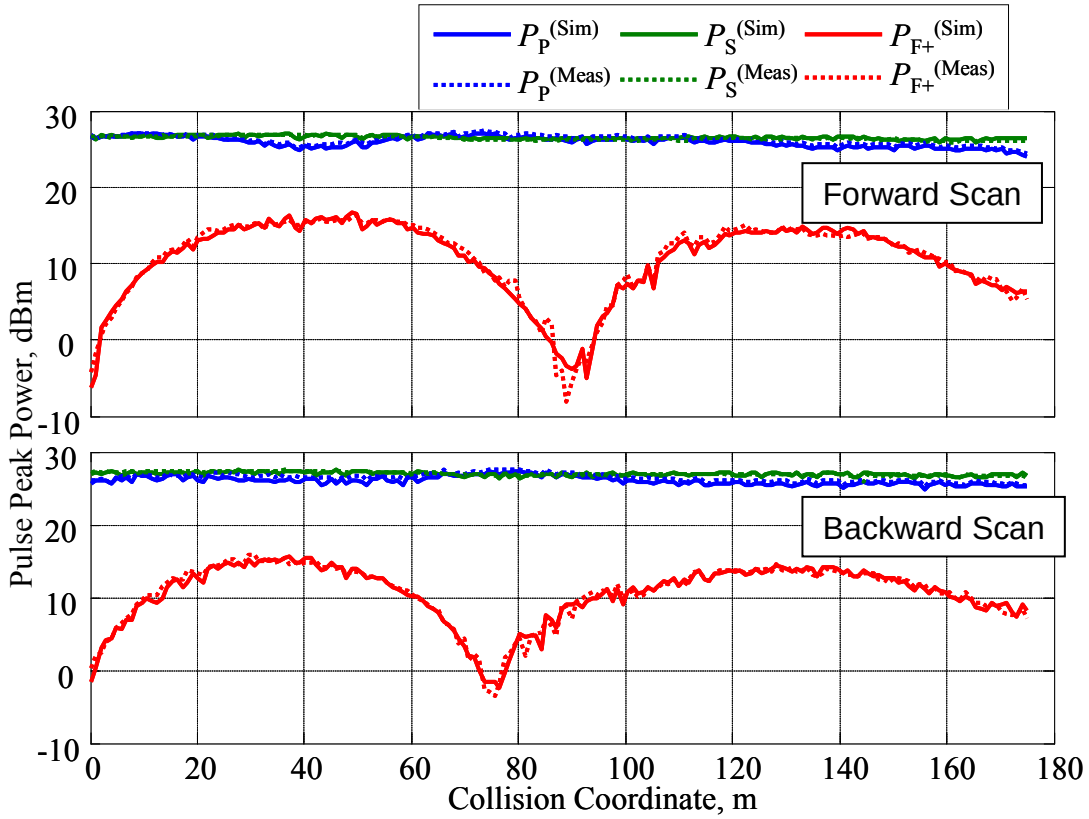

Fig. 38: Measured powers and simulated power of propagated pulses scanned in both directions for 175-m HNLF sample. Nonlinear index used in optimization algorithm: 17.2 W^{-1}km^{-1}.

The fiber was scanned in both directions: after completing the first collision scan, the fiber input and output were swapped and the scan was repeated, resulting in good

agreement between retrieved dispersion profiles, as shown in Fig. 38. The used wavelengths of the probe and second pulses are $\lambda_1 = 1559$ nm and $\lambda_2 = 1530$ nm. The period of the first spatial FPM oscillation differs by approximately 15 m (90 vs. 75 m) indicating that the ZDW of the front section is located closer to a probe wavelength by 1 nm (see eq. (1.2)). After the converging of the numerical algorithm, the simulated profiles reproduced the measured ones with the 0.9-dB accuracy, as shown in Fig. 40. The obtained ZDW profiles (Fig. 39) are obtained using simplex method started from the constant ZDW profile of 1562.5 nm.

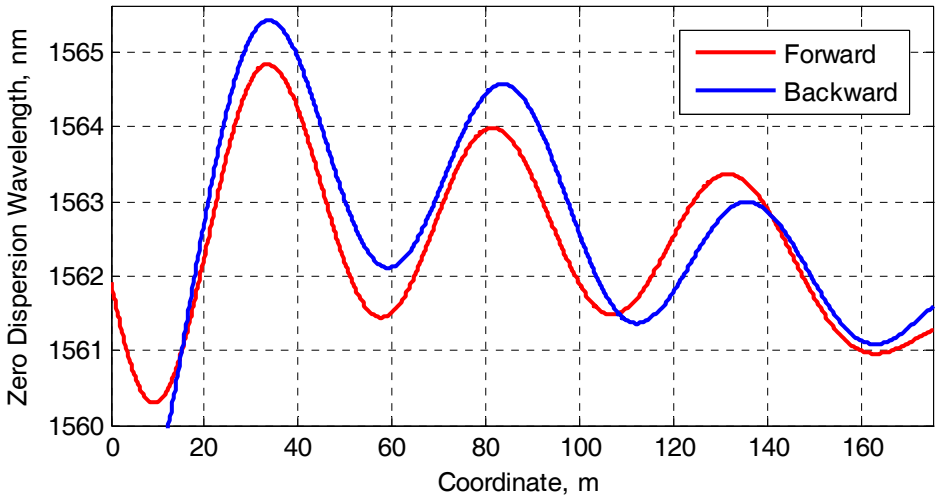

Fig. 39: Comparison between ZDW measurements obtained from traces scanned in both directions.

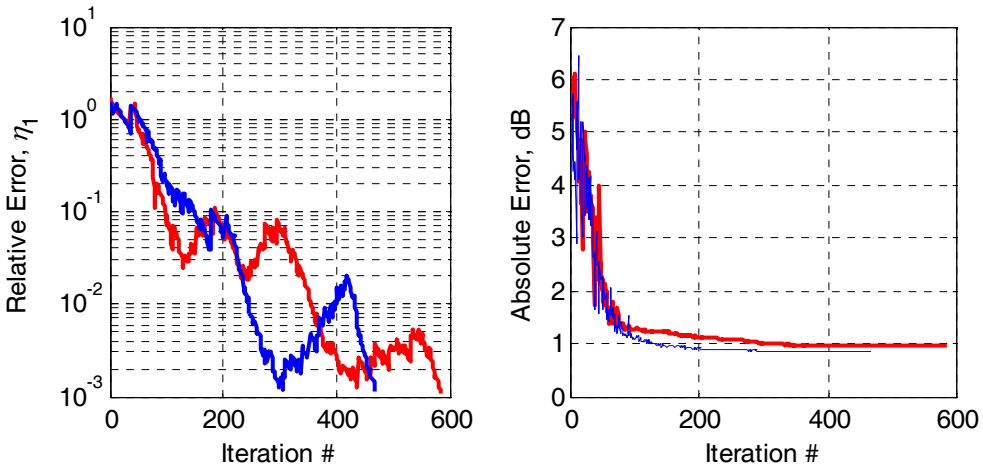

Fig. 40: Relative and absolute error of the simplex algorithm for forward (red) and backward (blue) scans.

In fact, the oscillations shown in Fig. 39 overestimate the real ZDW oscillations. Such uncertainty can be addressed to weak sensitivity of the power of FWM wave to variations of ZDW at locations of power extrema. Specifically, for the points corresponding to local maxima z_{max}, the phases of the complex vectors defining the local accumulated amplitude $\boldsymbol{B}_{FWM}(z_{max})$ of FWM wave and the vector defining the FPM contribution $\Delta(z_{max})$ (see eq. (5.3) and (5.9)) at short subsequent interval dz, dependent of the phase mismatch of the three interacting waves, are orthogonal (shifted by 90° in phase) so that the total power increase is small, i.e. $|\boldsymbol{B}_{FWM}(z_{max}+dz)-\boldsymbol{B}_{FWM}(z_{max})| \ll |\Delta(z_{max})|$. For the points corresponding to local minima, the vectors $\boldsymbol{B}_{FWM}(z_{max})$ and $\Delta(z_{max})$ are almost parallel so that the local phase mismatch (see eq. (5.4)) is badly resolved. In practice, this difficulty can be surmounted by simultaneous processing of several FWM profiles with non-overlapping positions of the extreme points and corresponding to different wavelengths of the scanning pulses.

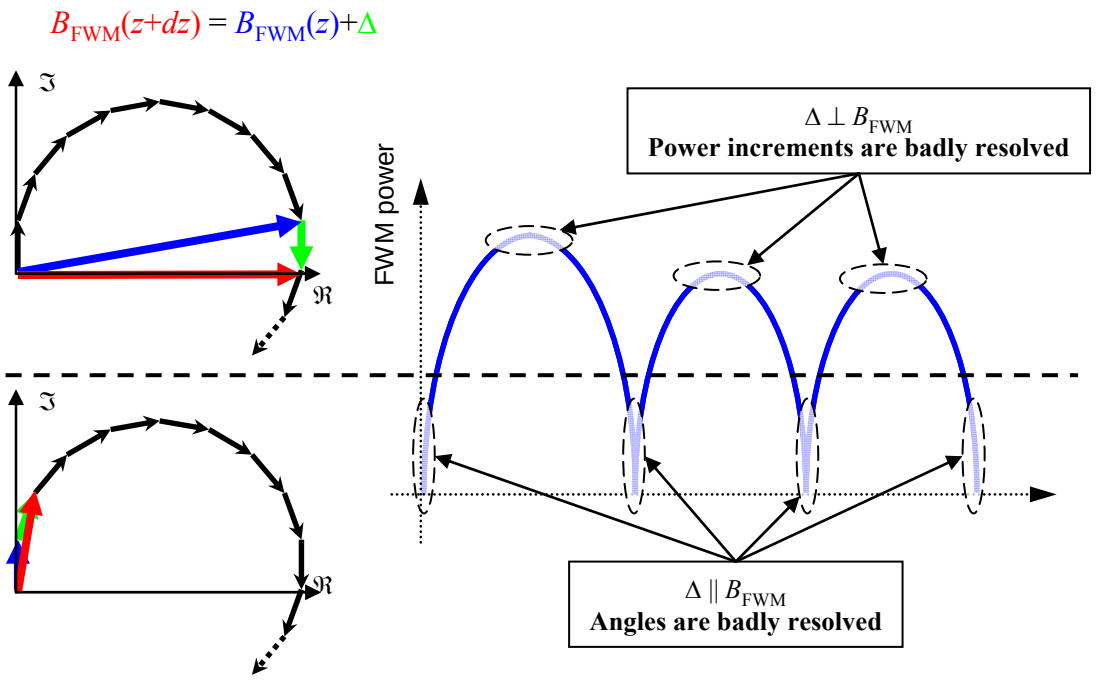

Fig. 41: Evolution of the FWM product in a fiber corresponding to extremal cases of minimum and maximum powers.

It is clearly seen from both measurements that the amplified probe transferred its energy for both Stokes wave and the second pulse and its power decreased by several decibel. In this case, the undepleted pump approximation is no longer valid and the geometrical and finite-difference methods could not be used.

5.5 Measuring Fiber Nonlinear Coefficient

The inverse dispersion retrieving algorithms described in chapter 5 require knowledge of the nonlinear refractive coefficient γ as an input parameter with the accuracy better than 5%. Several methods of measuring γ that exploit different nonlinear effects have been proposed. However, most of them need complicated signal sources, or suffer from a large uncertainty in the measured physical characteristics. This section

describes two "working" methods to measure γ utilizing the pulse sources used in the dispersion measuring setup shown in Fig. 13.

The first method called "two-tone method" presented in [80] is based on the measuring of the strength of the first order harmonic formed in nonlinear fiber by self-phase modulation. The signal launched to a fiber contains two spectral tones forming a periodic pattern in time domain. In the original article [80], these tones were formed by two independent lasers. Such two-tone oscillating pattern can be created using a single amplitude modulator driven by a single clock and biased at null point. The peak-to-peak voltage (typically, $\sim V_\pi$) is adjusted in order to guaranty the negligible power for the higher order harmonics. The experimental setup is shown in Fig. 42.

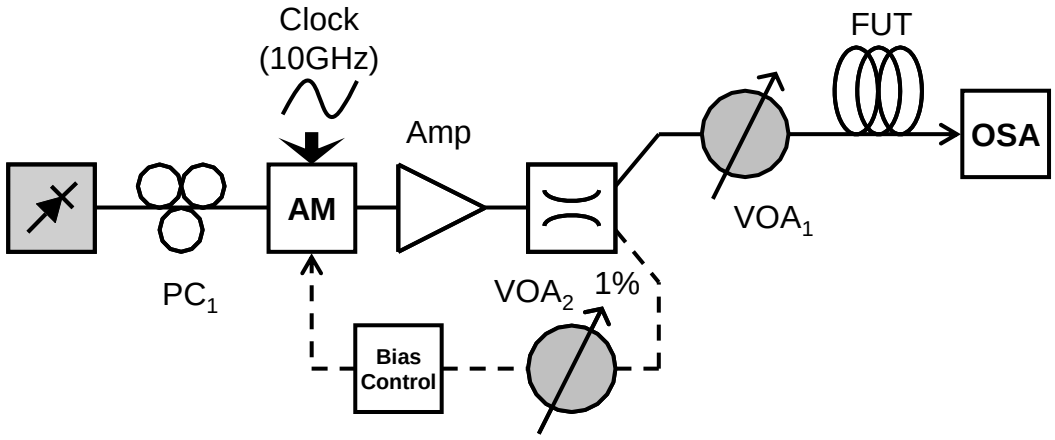

Fig. 42: Experimental setup for two-tone method.

The difference in power between zero- and first-order harmonics I_0/I_1 can be measured using an optical spectrum analyzer with the resolution of 0.01 nm (for example, Ando AQ6317B) and is given by

$$\eta = \frac{I_0}{I_1} = \frac{J_0^2(\phi_{NL}/2) + J_1^2(\phi_{NL}/2)}{J_1^2(\phi_{NL}/2) + J_2^2(\phi_{NL}/2)} \tag{5.17}$$

in which J_i is a Bessel function of i^{-th} order, $<P>$ is the average input power (measured by power meter), $\phi_{NL} = \gamma <P> L$ is the nonlinear phase shift, γ – fiber nonlinear coefficient, L – fiber length. The method provides "natural" means to measure the nonlinear coefficient because of low dispersion in HNLF. In such a fiber, the phase shift between closely-spaced harmonics is predominantly formed by SPM with a negligible effect of the linear phase rotation. The transcendental equation (5.17) for γ can be easily solved using a method of division of the interval of search by two. An example of the measured spectra for different average power launched to a 520-m HNLF is shown in Fig. 43. The factor η and the reconstructed nonlinear coefficient are shown in Fig. 44.

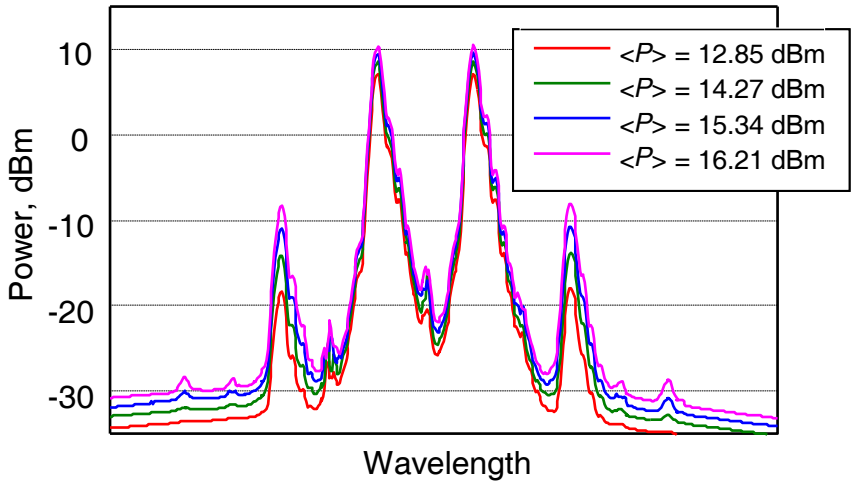

Fig. 43: Spectra measured for different input powers $<P>$.

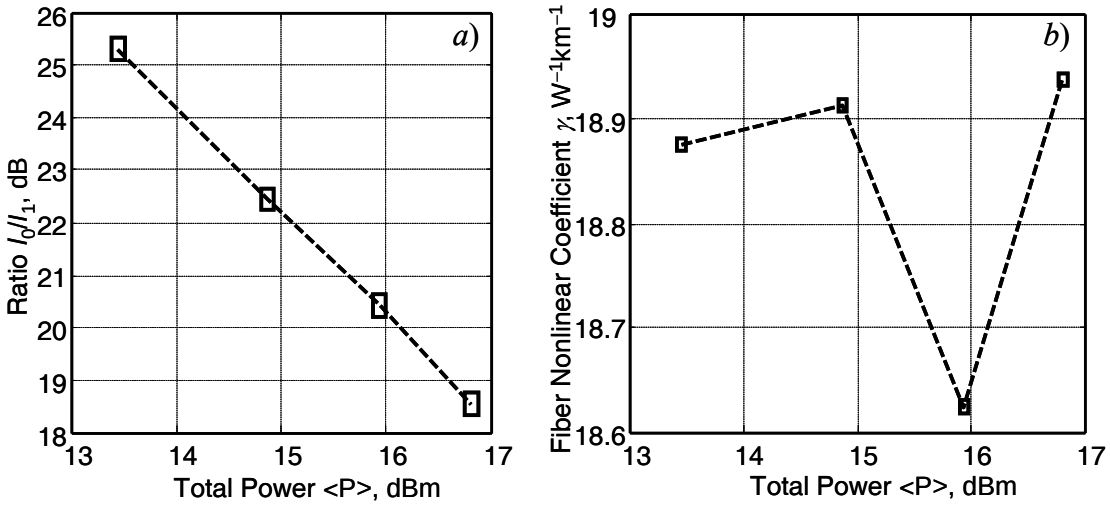

Fig. 44: *a*) Measured ratio I_0/I_1 and *b*) and nonlinear coefficient γ calculated using eq. (17) for different launched powers.

The second method [81] is based on detection of the nonlinear phase shift in self-aligned interferometer shown in Fig. 45. The input pulse is split between two interferometer arms with non-equal power. The lengths of the two branches are selected unbalanced in order to avoid pulse overlapping at the interferometer output. This output is connected to the fiber under test followed by Faraday mirror to unwrap the linear polarization rotation and stabilize the interferometer operation. The pulses propagated in the interferometer in clockwise and counter-clockwise directions see the same physical length and interfere. The polarization controller PC_2 is necessary to balance the polarization transfer matrices for these directions. The balancing can be done by maximizing output power for a weak input pulse. In order to simplify calibration procedure and to eliminate nonlinear phase shift in backward direction, the power at the fiber end was depleted significantly (more than 10 dB). For some pulse power set by variable optical attenuation VOA_1 and corresponding to a π-phase shift, the output power

reaches a null point. The typical measured waveforms are shown in Fig. 46. The nonlinear coefficient can be obtained from

$$\pi = \gamma \Delta P L \tag{5.18}$$

where ΔP is a power difference of the pulses propagating in long and short arms given by $\Delta P = \frac{P_0}{\alpha_{\min}\alpha_{\text{Splice}}}\left(\frac{1}{\alpha_{\text{L}}} - \frac{1}{\alpha_{\text{S}}}\right)$, P_0 is a pulse power before VOA_1, $\alpha_{\min}$ is the attenuation (VOA_1) corresponding to a null point, α_{Splice} is the fiber front splicing loss, α_{L} and α_{S} are interferometer losses of long and short interferometer arms.

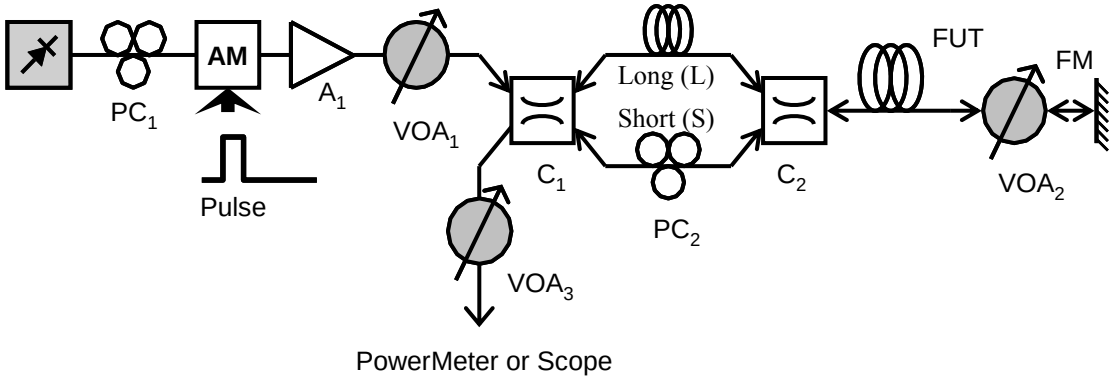

Fig. 45: Experimental setup for interferometric method.

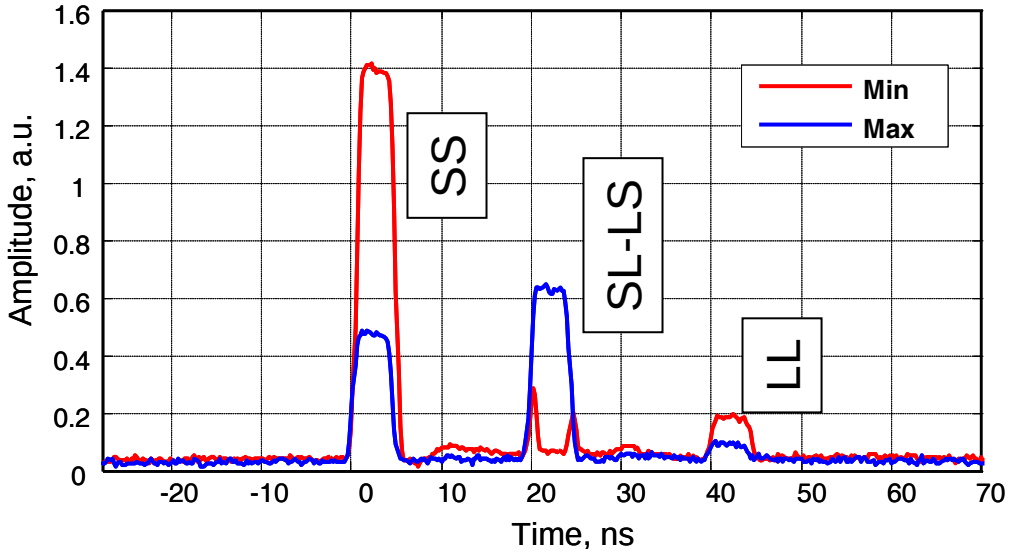

Fig. 46: The pulses at the interferometer output. Blue trace corresponds to low power of the launched pulse; red trace – to π nonlinear phase shift. Pulse duration: 5 ns.

For the same 520-m HNLF sample, $P_0 = 5.76$ W, $\alpha_{\min} = 4.1$ dB, $\alpha_L = 5.43$ dB, $\alpha_S = 9.7$ dB, $\alpha_{Splice} = 0.5$ dB, $\gamma = 16.9$ /W/km, which is less than the nonlinear index measured using two-tone method. The difference can be attributed to the stronger nonlinear polarization rotation because the significantly higher power was used for the second method.

6. Dispersion Measuring Technique with Polarization Scrambling

6.1 Polarization Locking Scheme

In the previously described realization (section 3.1) of the counter-collision setup, the polarization states of the week pulse (probe) and pump launched at opposite ends were controlled independently in order to maximize the Brillouin gain. Such operation, however, provides only local polarization synchronization since the counter-propagating signals evolve along different optical passes. The aforementioned setting implies that the pump and probe polarization states providing maximized gain even at adjacent points can be uncorrelated. The described practical difficulty can be alleviated by *polarization reversal*.

The concept is illustrated in Fig. 47. Assume that the pump and probe are launched at one fiber end at orthogonal states using a polarization beam splitter (PBS). The Brillouin effect is used to transfer energy from pump to probe so the polarization walk-off is negligible and the pulse states stay orthogonal at any point within a fiber because of relatively small Brillouin frequency shift. At the other end, the pulses are reflected by a Faraday mirror which guaranties the orthogonality of the polarization states of forward propagated signal and the reflected ones at any longitudinal position as well.

If the probe and the delayed pump pulses are launched at orthogonal states and the reflected probe pulse collides with a strong forward-propagating pump, their polarization states will be perfectly aligned. The interaction between the forward propagated probe and reflected backward propagated pump is less effective because of pump power loss in Faraday mirror and splices. For a single collision regime, the spacing between the consecutive pulses has to be longer than a quadrupled propagation time, as illustrated in Fig. 47*d*.

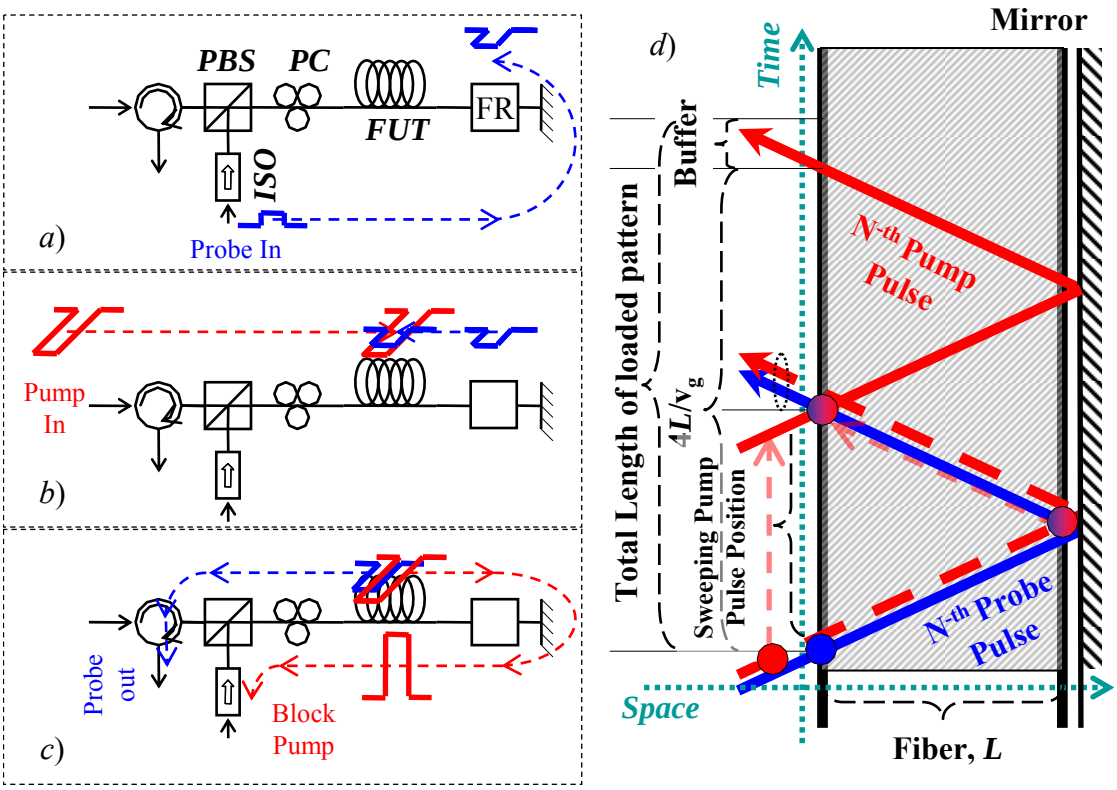

Fig. 47: *a*) Probe is launched through Polarization Beam Splitter (PBS), propagated in fiber (*FUT*) and reflected from Faraday Mirror (*FM*). *b*) Pump is launched at orthogonal state and collides with backward-propagating probe. *c*) Probe is passed through circulator (*CIR*), pump is blocked in isolator (*ISO*). *d*) Time-space evolution.

6.2 Dispersion Map Measuring Using Polarization Scrambling

The polarization control is the slowest part of the original dispersion measuring setup shown in Fig. 13. For example, the algorithm for the polarization tuning described in section 3.3 requires at least 50 power readings; the motorized polarization controller needs at least 0.25 s to set a certain polarization state. The total time needed to obtain 300 points is $300 \times 50 \times 0.25$ s = 62.5 min. This fact raises a question: is it possible to make the polarization algorithm faster, or, to eliminate it at all? The polarization locking scheme introduced in section 6.1 allows using only one polarization controller placed before a fiber under test instead of the two ones used in the original scheme. This controller must *not* contain a front polarizer in order to pass the pulses propagating in both directions at orthogonal states.

In the original setup, a calibrated scope was used to process the pulse powers. However, the real polarization beam splitters have finite extinction characteristic, typically, at the order of 25-30 dB. This implies that some little fraction of the pump will leak to a processing scheme and could not be filtered because of the small spacing between the probe and pump frequencies. During the propagation, the pump pulse generates the unpolarized Raman noise which is eliminated by PBS only by half. It is very important to note that the Faraday mirror reverts only the linear polarization rotation. Excessive polarization shift induced by a nonlinear rotation misaligns the polarization states of the co-propagating pulses at the output port of the PBS. Correspondingly, a certain part of these pulses is blocked, which is the opposite to a power calibration requirement (<0.5 dB) described in chapter 3.6.

All these facts add uncertainty to the powers of the waveforms measured using a scope and motivate us using the method based on different physical principles. First of all, the previous algorithm was based on the precise measurement of the ***absolute pulse powers***. The frequency discrimination was achieved by using a tunable filter in a processing scheme. Alternatively, the averaged pulse powers can be measured in frequency domain using an optical spectrum analyzer but the absolute pulse power could not be precisely estimated by the reasons described in section 3.6. The idea of using the ***relative pulse powers*** can be borrowed from the Mamishev's method [32-34] described in chapter 1.2. Specifically, the period of the spatial oscillation defines the averaged dispersion regardless of the pulse powers used. The gain value, and correspondingly, a peak pump pulse power, is no longer a critical parameter because the oscillations can be processed even for gain values of several decibels. The difficulty with gain polarization dependence can be resolved by replacing the polarization controllers PC_8 and PC_9 shown in Fig. 13 by the polarization scrambler (*PS*) put before fiber under test. In this case, the polarization averaged gain has to be considered in place of the gain maximized in the original scheme. In order to provide orthogonality of the interacting counter-propagating pulses, the polarization scrambling speed should be significantly slower than the doubled propagation time. For example, for 250-m HNLF sample, the pulse repetition rate is $2 \cdot 10^8/(2*250) = 400$ kHz. The polarization scrambler with 10-kHz rotation speed is a reasonable choice (for example, General Photonics PSM-001). On the other hand, the scrambling speed should be significantly faster than that of the detector measuring the power of FWM product to guarantee polarization-insensitive operation.

The modified setup is shown in Fig. 48. The block forming pulses is remained unchanged. The probe and pump pulses are launched to a fiber at orthogonal states in accord with the polarization locking scheme introduced in the previous chapter. The probe and the second pulse are combined before *PBS* so that their polarization sates are aligned at the fiber input. The amplified probe is coupled to the processing scheme using the circulator *CIR* whereas the pump is blocked by the isolator *ISO*. The output probe power (or gain) is measured as a function of the collision coordinate. The processing scheme can be either a standard optical spectrum analyzer or a lock-in amplifier detecting the power of the narrowly filtered FWM product.

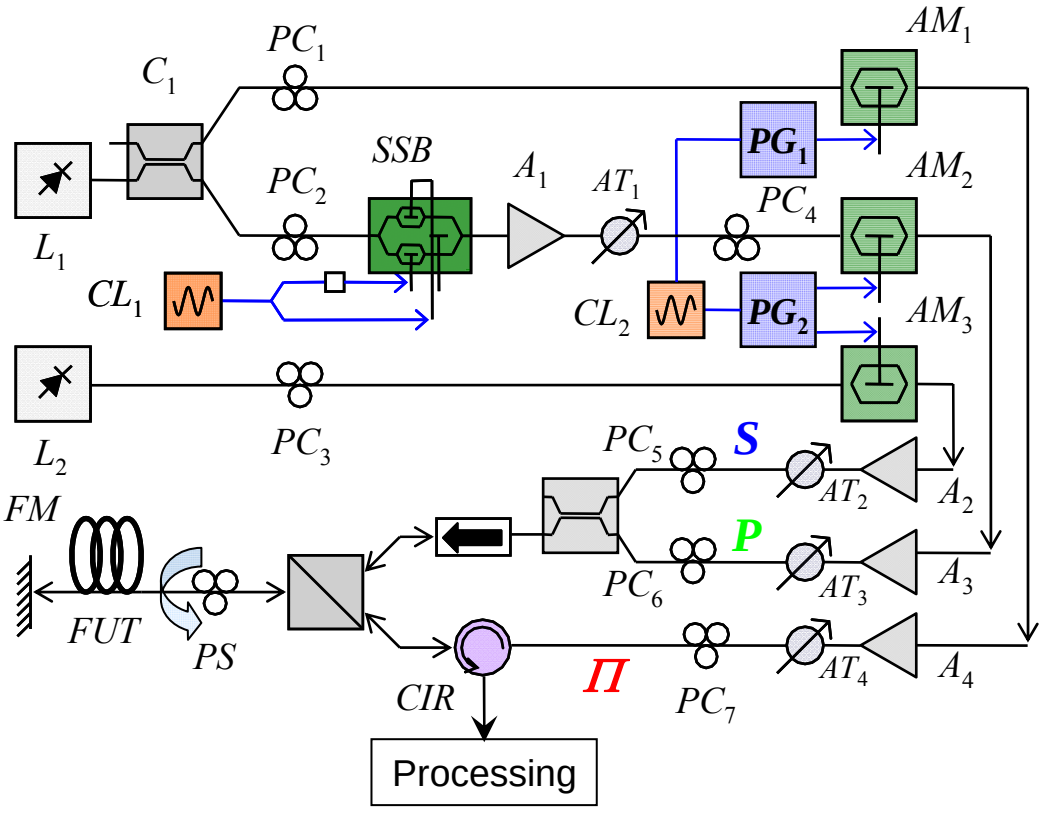

Fig. 48: Dispersion measuring setup with polarization scrambling.

The maximum length of the FUT amenable to the introduced technique depends on the fiber loss and nonlinear effects such as spontaneous Raman scattering depleting the pulse peak power. In practice, a gain of only several decibels is required allowing 500-m samples to be characterized.

It is important to emphasize that the scanning steps (defining the measuring ***accuracy***) smaller than the interval of interaction of the counter-propagating pulses can be used. Experiments demonstrated that the measured periods of FWM oscillations are practically independent of the pump pulse duration for the pumps shorter than 30 ns.

Fig. 49 demonstrates the power of the FWM product measured as a function of fiber coordinate in 210-m *L*-band fiber having more than 5 nm variations of ZDW and 0.013 ps/nm^2/km slope. The oscillation period varies between 16 to 23 m mapping the ZDW spatial profile shown in Fig. 50.

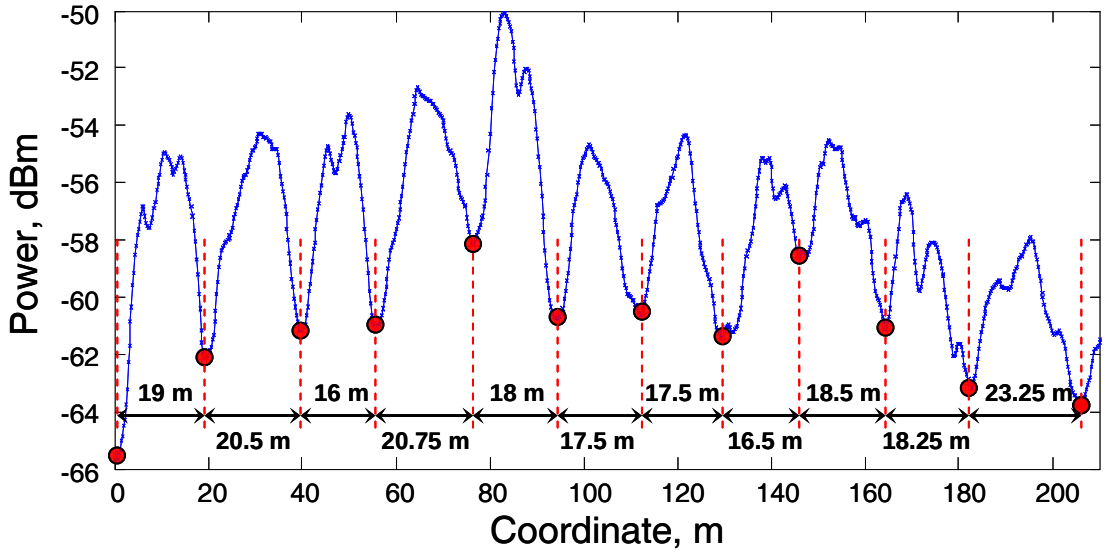

Fig. 49: Measured power of FWM product as a function of collision coordinate of 210-m HNLF sample. Pulse length: 2 m, scanning step: 25 cm, probe wavelength $\lambda_1 = 1578$ nm, second pulse wavelength $\lambda_2 = 1535$ nm.

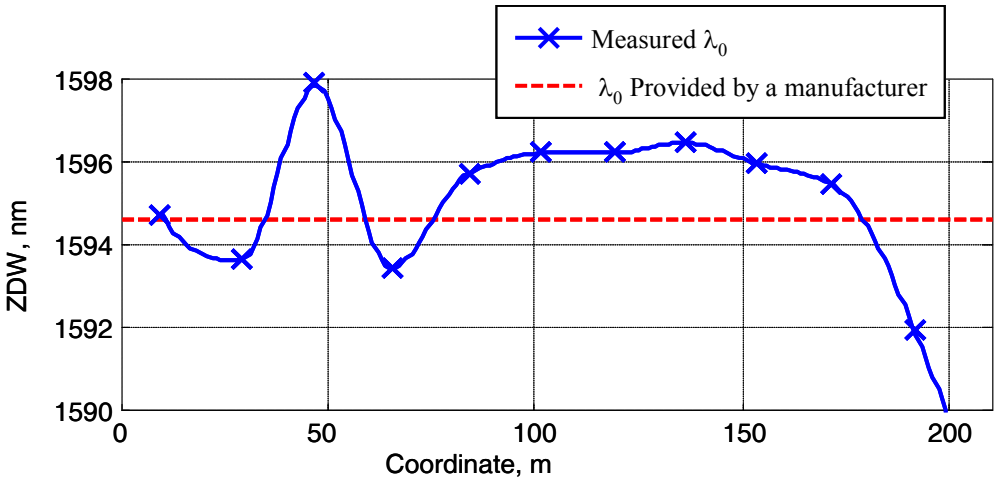

Fig. 50: Reconstructed ZDW map.

The second example of the evolution of FWM product in a 205-m sample measured in both directions is shown in Fig. 51. The dispersion slope of 0.0236 ps/nm^2/km and average ZDW of 1561.19 nm where measured by Advantest Q7750 test set. The oscillation period varied between 9 and 13 m corresponding to maximum ZDW deviation of 8 nm (Fig. 52).

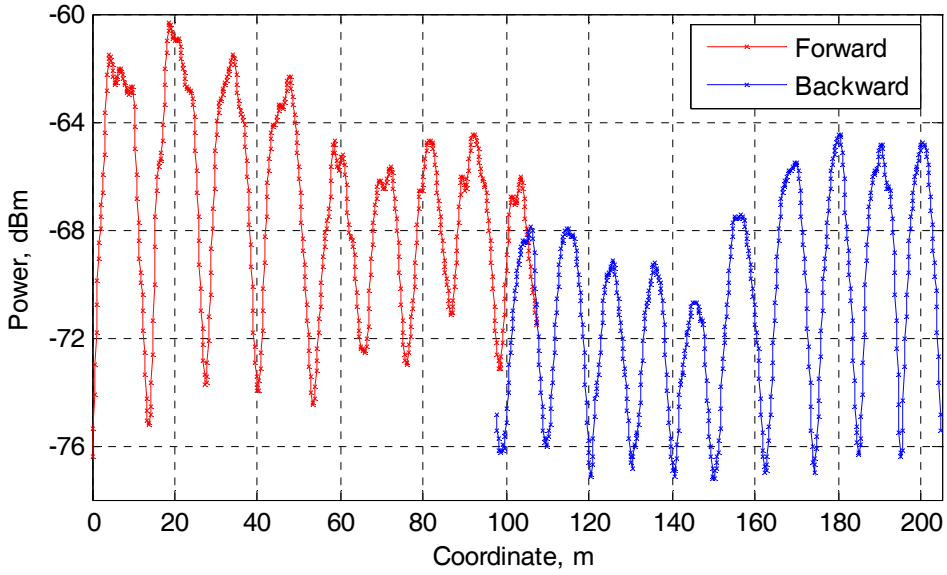

Fig. 51: Measured power of FWM product as a function of collision coordinate of 205-m HNLF sample. Pulse length: 2 m, scanning step: 20 cm, probe wavelength $\lambda_1 = 1537$ nm, second pulse wavelength $\lambda_2 = 1573$ nm.

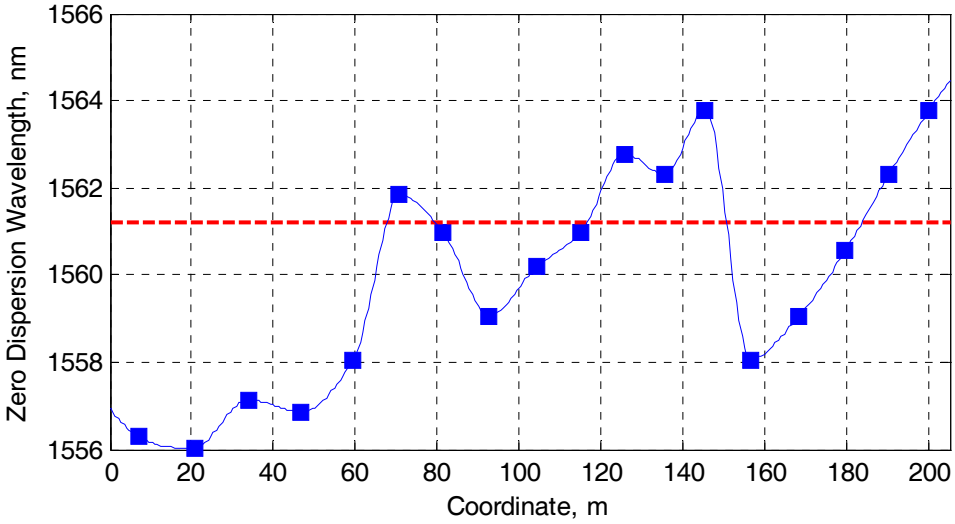

Fig. 52: ZDW map reconstructed from data measured in both directions. Dashed red line corresponds to a global ZDW of 1561.19 nm.

6.3 Equalization of the Polarization Walk-off Between Co-Propagating Pulses

The dispersion measuring scheme described in the previous chapter has a drawback for the case when the high (<10 m) spatial resolution is required. For typical HNLFs having a dispersion slope below 0.03 ps/nm^2/km, such resolution can be achieved if the spacing between co-propagating pulses exceeds 40 nm. The polarization states of the probe and the second pulse are perfectly aligned at the fiber input because they are launched through the same port of the polarization beam splitter, as illustrated in Fig. 48. However, experiment showed that the strength of the nonlinear interactions (i.e. measuring "contrast") degrades for far fiber sections if the polarization is scrambled. The situation is even worse if a fiber contains several spliced pieces. This behavior happens because real fibers necessarily possess random asymmetries in the transversal geometry resulted in different mode propagation indexes for two orthogonal polarization directions. The effect is known in literature as polarization mode dispersion or PMD. More importantly, it causes the polarization walk-off of the signals at different frequencies. In short fibers, a certain orientation of the polarization (a principle state) minimizing the walk-off within a broad band exists. In HNLFs, the principle states typically present for the samples shorter than 200 m. As an illustration, Fig. 53 shows the evolution of the polarization state on the Poincare sphere for a signal swept in wavelength between 1520 and 1580 nm and measured at the output of the 205-m-long HNLF sample. It is important to emphasize that HNLFs typically have higher PMD in comparison to that of standard fibers because of stronger mode confinement. The effect of PMD is "amplified" if the HNLF is spooled onto the low diameter reels.

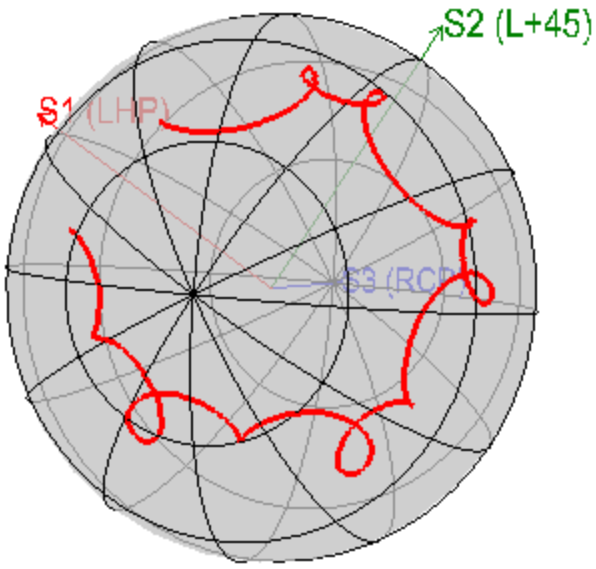

Fig. 53: Polarization evolution as a function of wavelength. Wavelength step: 0.1 nm.

The second difficulty is that the overlapping probe and second pulses transfer their energies to FWM waves while propagating in both directions. Both issues can be resolved by combining the second pulse with a probe only at the backward pass and separating their polarizations. Typically, their wavelengths are located at different bands so that they can be easily joined with negligible loss using standard C/L band couplers. In this configuration, the FWM product has to be coupled to a processing *before* the polarization beam splitter. The final scheme is shown in Fig. 54. The *WDM* is a standard multiplexer used to combine pump and signal in Raman or Erbium-doped amplifiers.

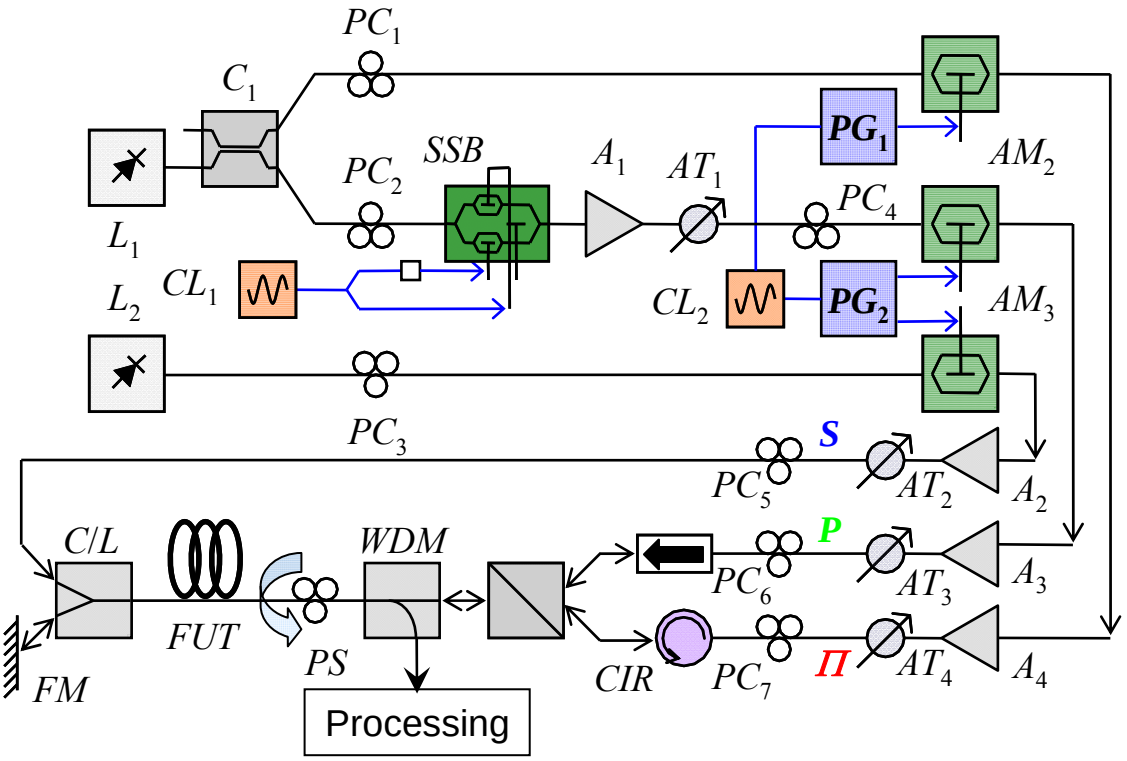

Fig. 54: Dispersion measuring setup with polarization scrambling. Probe and second pulse are separated.

Experiment proved that the average power of the FWM product is practically independent (<1 dB) on the polarization of the second pulse set by PC_5 if the pump/probe polarization is scrambled.

Fig. 55 demonstrates the Stokes power oscillations generated in a fiber with shifted chromatic dispersion (DSF) having ZDW of 1563.53 nm and slope of 0.079 ps/nm^2/km. The spatial period is almost constant indicating ultra-low dispersion variations (see Fig. 56*a*). This result is verified using a noise injection technique [50] by observing the spectra of the idler waves. The idlers are generated by a widely spaced (>200 nm) pump, tuned across ZDW, and a fixed probe. It is seen from Fig. 56*b* that there is a sharp resonant peak centered at 1910.5 nm corresponding to the narrow 0.3-nm bandwidth in which the phases of the interacting waves are matched.

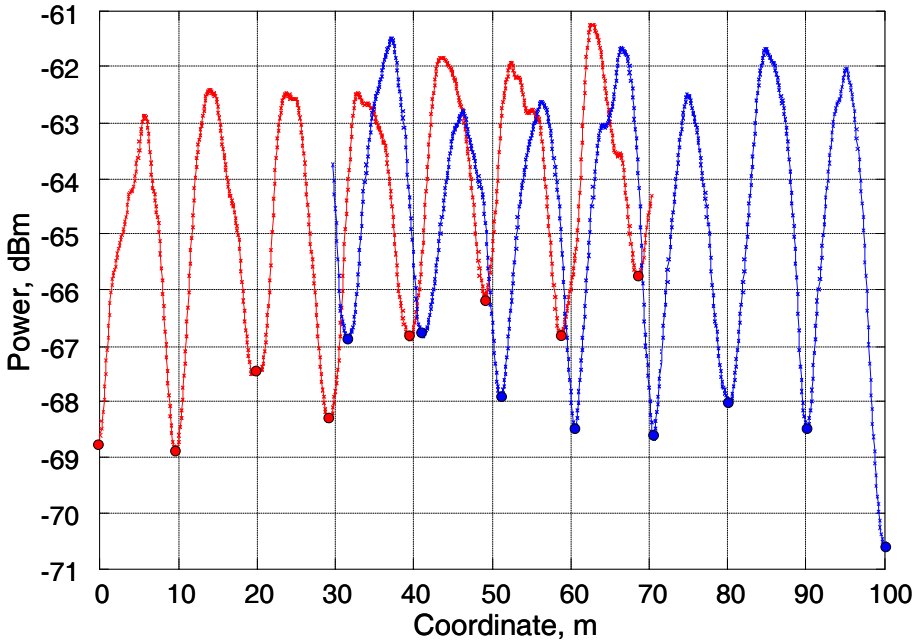

Fig. 55: Measured Stokes power as a function of collision coordinate for 100-m long DSF sample. Pulse length: 2 m, scanning step: 10 cm, probe wavelength $\lambda_1 = 1560.582$ nm, second pulse wavelength $\lambda_2 = 1610$ nm.

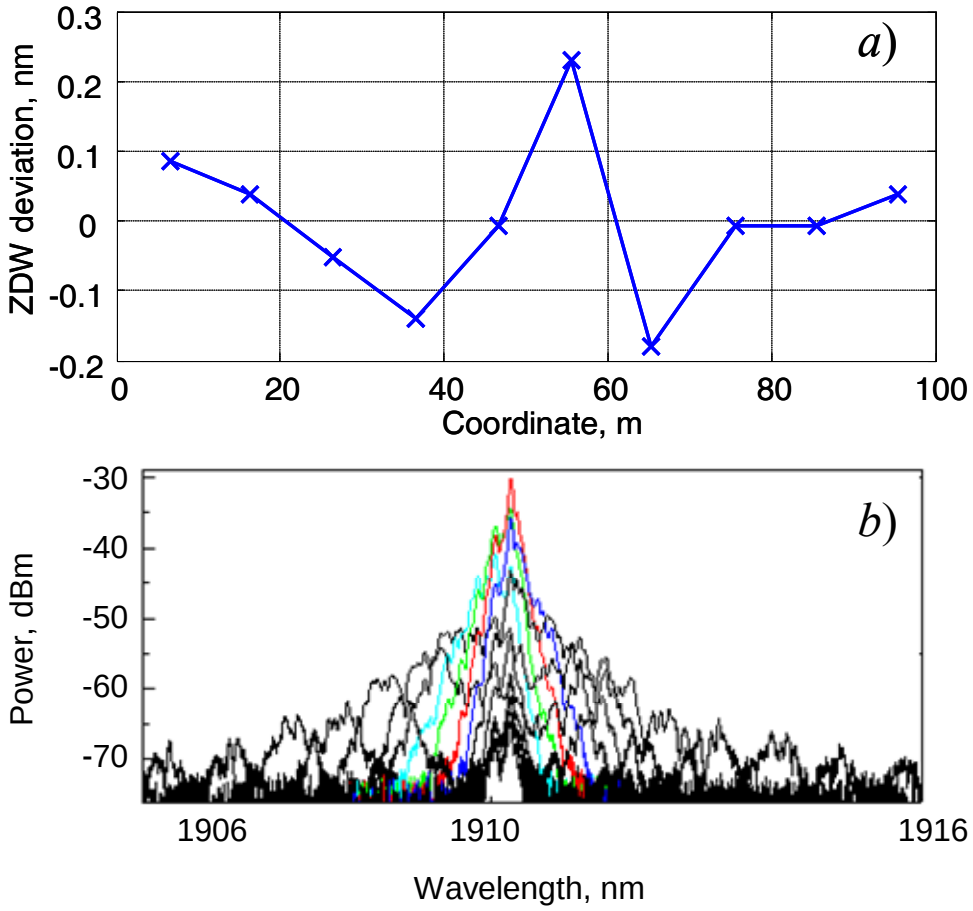

Fig. 56: *a*) Variations of ZDW reconstructed from data measured in both directions. *b*) Spectra of the idler waves measured for different positions of the pump.

6.4 Sensitivity and Resolution Control

The accuracy of the new method requires special considerations. First of all, the period of the spatial oscillation Λ_z given by

$$\int_z^{z+\Lambda_z} \Delta\beta(z)dz = \langle \Delta\beta(z, z+\Lambda_z) \rangle \Lambda_z = 2\pi \qquad (6.1)$$

defines the resolution. $\langle \Delta\beta(z, z+\Lambda_z) \rangle$ is the averaged phase mismatch at interval $(z, z+\Lambda_z)$ with β given by eq. (4.25-26). Second, even more important issue is the sensitivity of the method to the variation of the zero dispersion wavelength λ_0. Let us

assume that the reference wavelength (or, equivalent ω_{ref}) is selected equal to a zero dispersion wavelength. In this case, β_2 coefficient is zero and the phase mismatch is defined by the third order dispersion term given by eq. (4.26). Assume also that at some spatial coordinate z_1 the spacing between the probe wavelength λ_1 and λ_0 is $(\lambda_1-\lambda_0(z_1))$ and, at some nearest coordinate z_2, is $(\lambda_1-\lambda_0(z_2))$. The relative difference between the periods of oscillation (or contrast factor η) is

$$\eta = \frac{\Lambda_z(z_1)-\Lambda_z(z_2)}{1/2\left(\Lambda_z(z_1)+\Lambda_z(z_2)\right)} = \frac{\lambda_0(z_1)-\lambda_0(z_2)}{\lambda_1-\left(\lambda_0(z_1)+\lambda_0(z_2)\right)/2} = \frac{\Delta\lambda_0}{\lambda_1-\langle\lambda_0\rangle} \qquad (6.2)$$

In order to maximize this fraction, i.e. in order to increase sensitivity, the denominator has to be maximized which means that the position of the probe wavelength should be set as closely as possible to an averaged zero dispersion wavelength. If the wavelength difference $(\lambda_1-<\lambda_0>)$ is too small, the spatial resolution decreases. In practice, the contrast of 30% is a reasonable choice. If the variations of the zero dispersion wavelength are high and comparable with the spacing $(\lambda_1-<\lambda_0>)$, the best strategy is to scan fiber using several different probe wavelengths λ_1.

Let us consider a typical example. Assume that the FUT is an HNLF sample with measured $<\lambda_0>$ = 1550 nm, zero dispersion profile variations $\Delta\lambda_0$ = 5 nm, and dispersion slope S = 0.029 ps/nm^2/km. Assume also that the spatial resolution Λ_z = 10 m is required. Obviously, the spacing $|\lambda_1-<\lambda_0>|$ has to be larger than $\Delta\lambda_0$. From (6.2), in order to get η = 40% of contrast factor across the whole fiber distance, the wavelength of the probe must satisfy the relation $\lambda_1-<\lambda_0> = \Delta\lambda_0/\eta$ = 12.5 nm, i.e. the λ_1 should be set to 1537.5 nm (1550−12.5). The position of the second pulse can be estimated using

equation (1.2) with $D = S(\lambda_1 - <\lambda_0>)$. The corresponding frequency spacing $\delta\lambda = (\lambda_1 - \lambda_2) = 46.5$ nm. The obtained wavelength of the second pulse is either $\lambda_2^{(1)} = \lambda_1 - \delta\lambda = 1491$ nm, which has to be rejected because this wavelength is beyond the operating bandwidth of standard telecom amplifiers (which is typically 1530–1610 nm), or $\lambda_2^{(2)} = \lambda_1 + \delta\lambda = 1584$ nm, which perfectly matches the center of the *L*-band amplifier bandwidth. The corresponding wavelength of the generated FWM product is 1493.7 nm.

7. Applications beyond Dispersive Measurement

7.1 Polarization scanning

Polarization characteristics play a critical role in virtually all applications of fiber optics of high practical interest: from communications, to all-optical processing, and sensing applications. After a decade of research of polarization mode dispersion and its mitigation, the developed characterization techniques were focused on global polarization characteristics [66]. The recent advances in fiber optics and signal processing, however, have put forth the importance of local waveguide properties. In this contribution, we extend the introduced counter-colliding power delivery class of characterization methods to spatially resolved characterization of fiber polarization parameters. The method avails meter-scale polarization characterization, and thus the full visualization of optical field polarization evolution in the fiber. Linear polarization evolution of a monochromatic wave in fibers can be fully characterized if the birefringence vector $\boldsymbol{\beta}$ is known at every spatial point [66]. Provided that the orientation of the principle axis is fixed, a full revolution of the field occurs at a distance equal to the fiber beating length Λ_B. The second parameter, correlation length, describes the spatial orientation statistic of the

vector β. Several methods based on the polarization OTDR technique [71] have been presented to measure the described linear rotation parameters.

The proposed technique utilizes the fact that the strength of the nonlinear amplification strongly depends on the absolute polarization states of the interacting signals. The polarization locking scheme with a Faraday mirror introduced in chapter 6.1 reduces the dependency of the nonlinear gain to a function of a single polarization parameter. In this case, localized gain measured along fiber coordinate provides direct mapping of polarization evolution in optical fiber.

The polarization scanning setup is a simplified version of the dispersion scanner shown in Fig. 54 without a block forming a second pulse and with manual polarization controller replaced the polarization scrambler *PS*. The output probe power (or gain) is measured as a function of the collision coordinate. During the full length scan, the input polarization states of propagated pulses are kept fixed.

It is important to note that the previous experiments on the Brillouin gain of CW signals [68] implied pump and signal co-polarization as a sufficient condition for SBS gain maximization. According to this reasoning, since the interaction is strictly localized and the proposed configuration ensures strict polarization co-alignment, the SBS gain should be equalized gain along the fiber. In order to verify the validity of this statement, the gain at some fixed spatial point was scanned as a function of coordinate on a Poincare sphere. The polarization states were measured using a polarization analyzer.

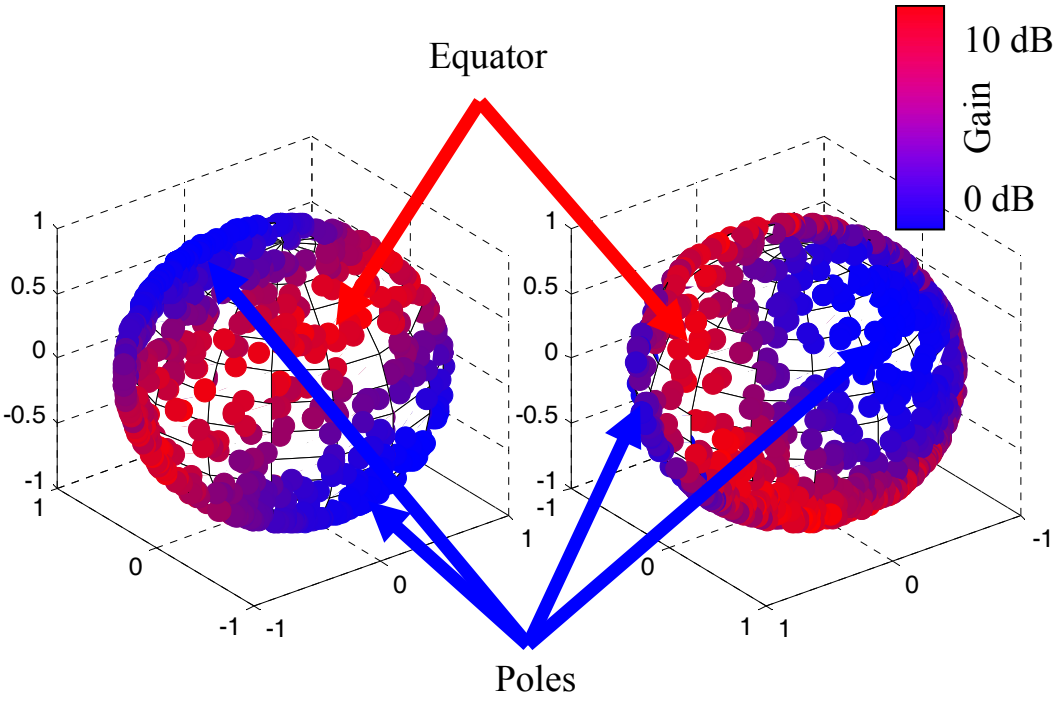

Fig. 57: Measured SBS gain as a function of polarization coordinate on a Poincare sphere (views from both sides). 100 realizations.

The experimental results shown in Fig. 57 clearly exhibit that the maximized gain is achieved for specific polarizations lying in the plane corresponding to the linear polarization whereas the circular polarization state demonstrates the absence of SBS amplification. The typical pulse profiles corresponding to maximum and minimum (zero) gain are shown in Fig. 58.

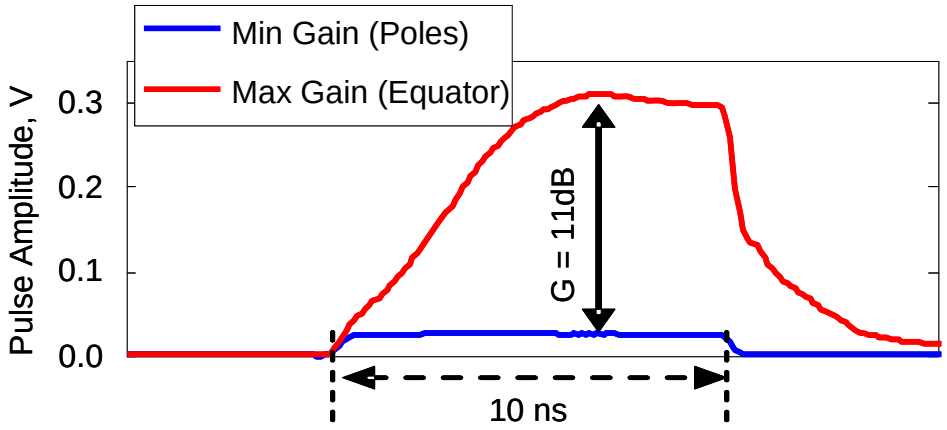

Fig. 58: Pulse waveforms measured at same collision point for polarization states corresponding to maximum and minimum gain.

During the propagation, the polarization of the probing pulse rotates around the local axis of birefringence and the polarization dependent gain mimics the local polarization state. Two distinct cases are possible: if the local PS lies on the equatorial plane or at some nearby point, the probe polarization vector crosses the equatorial plane twice during the scanning interval corresponding to localized polarization beating length. The polarization vector crosses equator twice as shown in Fig. 59*a*, providing two maxima and minima of SBS gain. If the principle state is shifted from equator, the polarization vector could cross equator twice, or does not cross it at all, showing only one pair of extrema (Fig. 59*b*) during the whole rotation period. This limitation imposes difficulties to interpretation of the obtained results. In addition, if the input polarization before some short section is located closely the fiber local principle state (PS), the polarization vector fills some small area on the Poincare sphere around the PS causing the degradation of the measuring gain contrast. This limitation can be overcome by using a second, and if necessary, the third scan for the polarization states rotated by 90° in Stokes space relatively to original input SOP. For fixed spatial coordinate, the trace with the

fastest oscillating spatial frequency has to be selected. The spacing between the nearest minima defines the distance corresponding to a half of the fiber beating length. The spacing between the nearest maxima depends on the orientation of the local PS and is not equidistant in general.

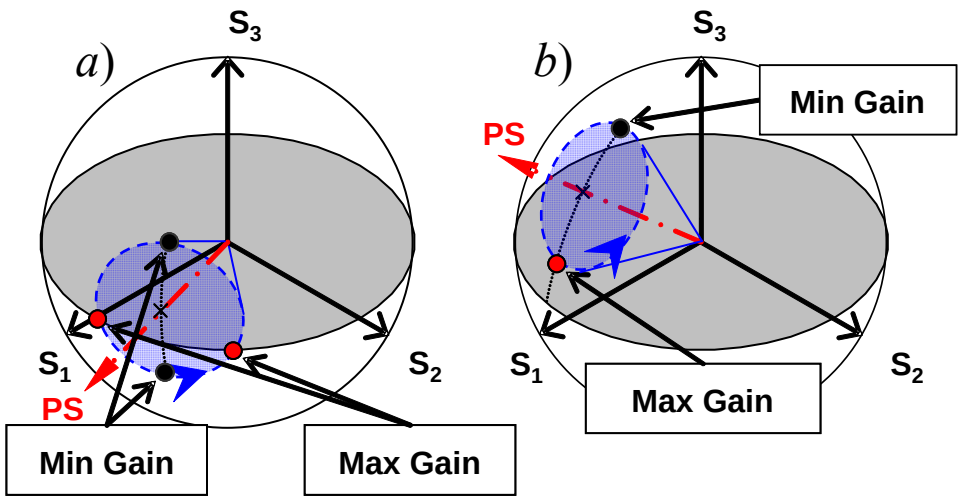

Fig. 59: Representation of the polarization evolution in Stokes space.

Fig. 60 demonstrates the measured power of the scanned probe as a function of collision coordinate for 42 m HNLF sample for 3 different input polarization states: horizontal linear (LHP), 45° rotated linear (L+45°P), and right circular (RCP). It is clearly seen that the spacing between nearest minima varies with the distance. This spacing is different for different input polarization states. For example, at the 0-10 m interval, the fastest rotation corresponds to RCP state (black line) with the spacing between the minima approximately equal to 3 m, or 6 m beating length. Between 15 and 25 m, the red trace demonstrates the fastest rotation with 6 m oscillation period. Although the power of the pump pulse was constant along the link, the maximum gain varied. The maximum gain corresponds to the interval with the slowest polarization rotation. For example, the gain is maximized for the spatial coordinates between 20 and

30 m. Such behavior can be addressed to intra-pulse polarization rotation providing non-constant spatial gain during the collision event.

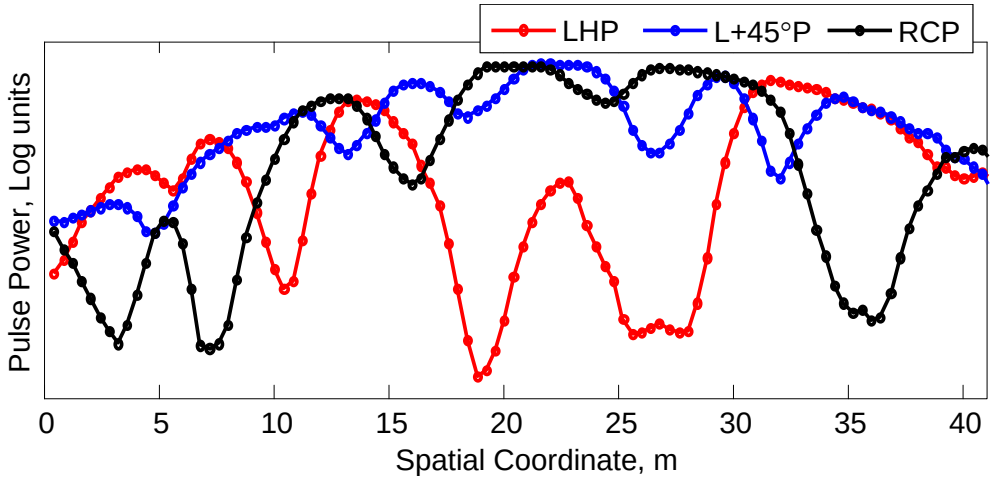

Fig. 60: Measured probe power as a function of collision coordinate for 3 different polarization states orthogonal in Stokes space. First 42-m HNLF sample. Pulse length: 2 m, scanning step: 40 cm.

Fig. 61 shows the scan of the power of the amplified probe for the second 210-m HNLF sample. The beating length 14 m is observed at 0-75 m and 150-210 m intervals but it is nearly doubled at 90-120 m. The degradation of the peak probe power is explained by significant pump pulse depletion in the nonlinear fiber by generation of the Raman spontaneous noise.

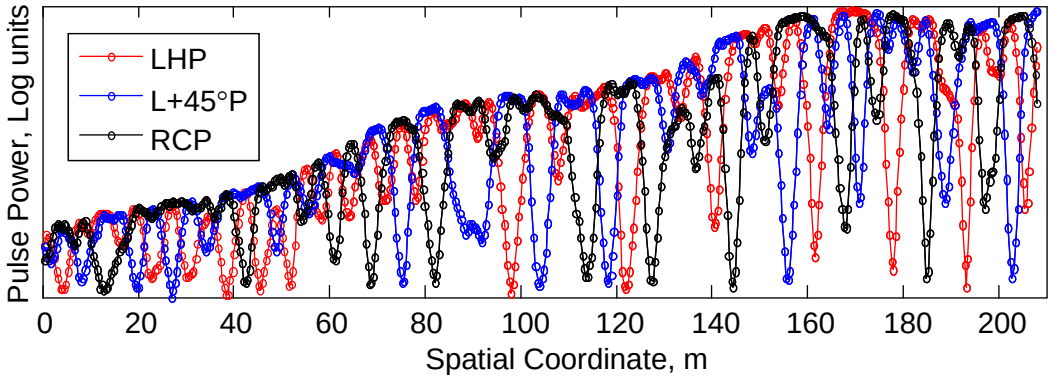

Fig. 61: Measured probe power as a function of collision coordinate for 3 polarization states orthogonal in Stokes space. Second 210-m HNLF sample. Pulse length: 2 m, scanning step: 40 cm.

7.2 Spatially Resolved Measurements of the Brillouin Frequency Shift

Brillouin gain spectrum measurement along an optical fiber is a standard technique for strain monitoring in installed cables [83], distributed temperature sensing [84], as well as the mapping of the Brillouin frequency shift [85]. The counter-colliding Brillouin scanner can be easily adapted to measure a map of the SBS frequency shift by adding a control for CL_1 clock tracking SBS frequency (see Fig. 54). This setup is similar to a scheme presented in [85] but it does not require a polarization alignment because polarization states are locked and randomized. A special attention should be paid to the biasing of the SBS modulator. It was mentioned in chapter 3.2, in order to shift a carrier by a SSB modulator, the upper and lower branches have to be modulated by clocks shifted in phase by a quarter of period. In the experimental setup, the phase shift was implemented using a trombone RF delay line. Unfortunately, the delay line has a significant dispersion so that the delay varied more than a period when the modulation frequency is shifted by 200 MHz. The half-period shift corresponds to a configuration when the optical carrier up-shifted relatively to original frequency violating the initial requirement for SBS amplification. This difficulty can be resolved by (i) disabling one RF port of the SSB modulator with an input delay line and biasing both branches at null working point, or by replacing (ii) SSB modulator by standard AM modulator biased at null point.

The linear dependence of the SBS frequency shift of the applied straining force was experimentally verified using a setup shown in Fig. 9*b*. The fiber was stretched with tension constant across the fiber. The SBS gain spectra was read from RF spectrum

analyzer detecting the beating of the input and back-reflected signal. Fig. 62 shows the spectra corresponding to 0, 20, 40, 50, 63, 75, 90, and 100% of the maximally available tension. It is clearly seen that the peak shifts in linear manner.

Fig. 63 demonstrates the measured SBS frequency map of the 100-m HNLF stretched using stair-like tension. The applied tension varies between zero and 75% of the maximally available tension resulting in the shift of 350 MHz. The shift is at least ten times wider than the width of the Brillouin gain profile.

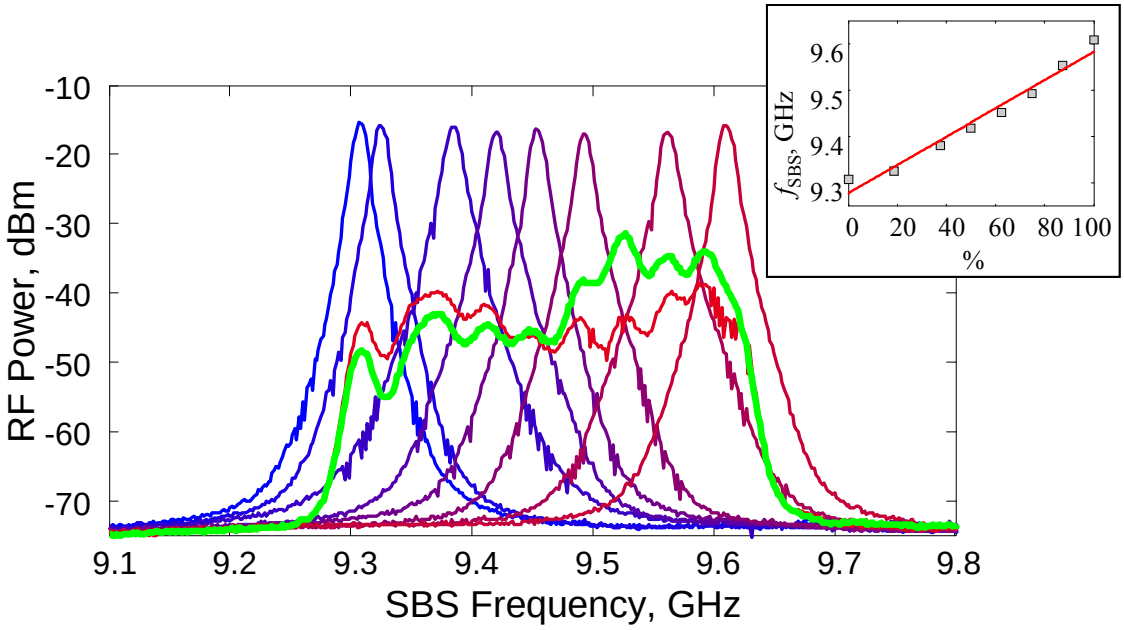

Fig. 62: The RF spectra obtained using a setup Fig. 9*b* for to different tensions. The inset demonstrates the SBS shift as a function of the applied force. A bold green line corresponds to the SBS spectrum of the fiber with monotonic stair-like stretching map shown in Fig. 63.

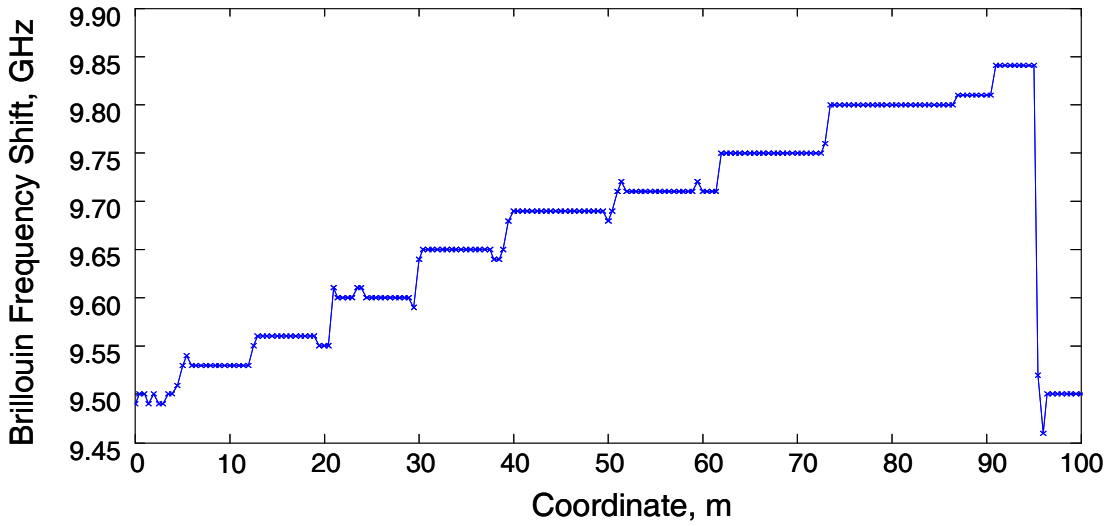

Fig. 63: Brillouin frequency shift of 100-m HNLF sample as a function of fiber coordinate measured at 1537 nm. Scanning step: 50 cm, scanning accuracy: 10 MHz.

7.3 Spatial Dispersion Equalization

A method for wideband parametric synthesis can be devised by taking advantage of longitudinal fiber stretching. It was shown previously that the stimulated Brillouin scattering (SBS) frequency shift is affected by the applied tension. In [82], the SBS frequency was modified along an SMF spool by applying steadily increasing tension to suppress the Brillouin back-scattering of the pump. Conversely, a spatially resolved map of the SBS frequency shift was used to determine the distributed tension as a function of the fiber coordinate [83], [85]. On the other hand, the measurements of the ZDW of such strained fibers showed that their dispersion characteristics are also modified [86]. Combining the above with the localized ZDW mapping, the question naturally arises: can localized tensioning be supported by the exact knowledge of ZDW fluctuation in order to construct superior parametric mixers? This section aims to answer this question by proving that the ZDW fluctuation profile can be equalized by applying spatially controlled tension to effectively invert ZDW variations.

The method relies on precise knowledge of spatial dispersion profile of the HNL fiber. By introducing a longitudinal tension map, inverse with respect to the measured variations, a ZDW profile can be in principle equalized, as illustrated in Fig. 64. Consequently, the ability to synthesize nearly arbitrary dispersion profile is an obvious generalization of this method.

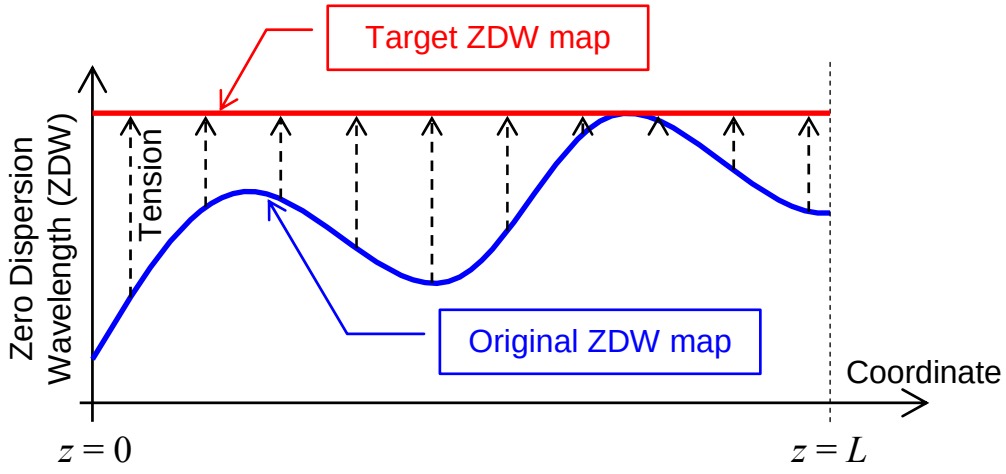

Fig. 64: Concept of the dispersion equalization.

The function that defines the dependence of the global ZDW ($<\lambda_0>$) with respect to applied longitudinal force (F) used to stretch the fiber segment was first calibrated to estimate the range of the method applicability. As an illustration, measured dispersion shown in Fig. 65 indicates a typical case, supporting the assumption of linear dependency that was demonstrated in [86]. This fact significantly simplifies a calibration procedure because it requires measurements of only two scalars (F and $<\lambda_0>$) for unstrained and spatially-constant tension. It is well known that the stimulated Brillouin scattering (SBS) frequency shift is affected by the applied tension as well [85]. Consequently, the measured spatial SBS frequency map can be used to reconstruct the tension map with nearly arbitrary spatial resolution.

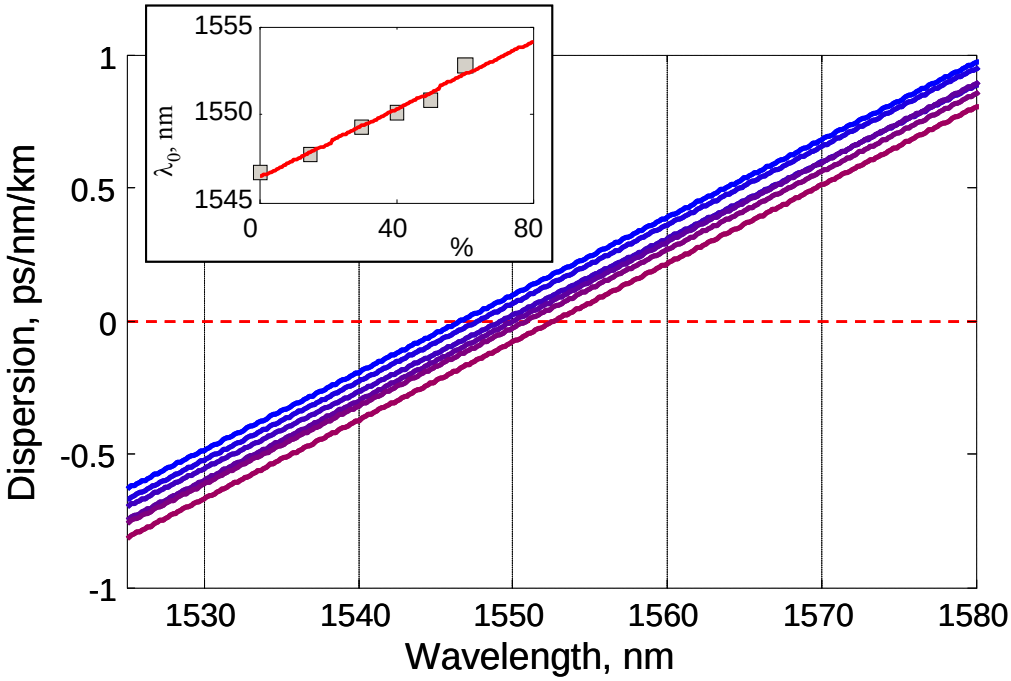

Fig. 65: The HNLF dispersion profile measured for different tensions: The inset shows a dependence of the ZDW of the applied tension measured in percent of the maximum value provided.

Two 205-m-long consecutive sections from a single HNLF spool were selected as it exhibited significant ZDW deviations; these samples are referred to as the fibers under test (FUT), henceforth. The two samples were characterized by mean (global) ZDWs of 1551 nm and 1559 nm and dispersion slope of 0.024 ps/nm2/km, as measured using a commercial dispersion measuring unit (Advantest Q7750). Obtained global $<\lambda_0>$ values were used in order to calibrate the wavelength positions of the interacting pulses to provide 10-m spatial resolution for counter-colliding Brillouin technique with polarization scrambling described in section 6.2. Specifically, in the case of the first sample, the positions of the probe and second pulses were set to 1540 nm and 1590 nm and for a second sample at 1550 nm and 1600 nm, respectively.

In a first step of the procedure, the powers of the FWM product formed by co-propagating pulses were scanned as a function of the spatial coordinate in both FUT directions with a 20-cm spatial step, as illustrated in the upper plots of Fig. 66. The measurement used a master RF clock driving an amplitude modulator to lock the probe carrier relative to the pump to a fixed frequency of 9.3 GHz, matching the global SBS frequency shift of the fiber samples. For the first sample (Fig. 66*a*, upper plot), the observed change FWM oscillations period was from 20 to 10 m between the front and the rear sections of the fiber, indicating that the probe wavelength is 50% closer to the local ZDW at the front section, corresponding to ZDW deviations in excess of 6 nm. For the second sample (Fig. 66*b* upper plot), period of FWM spatial oscillations decreased monotonically from 33 to 10 m within the front 140-m-long section, and corresponds to a ZDW variation between 1553 nm and 1563 nm. The remaining (65-m-long) section resulted in FWM oscillation interval changes from 10 to 22 m. The ZDW profiles of the original samples are shown by red circular marks in Fig. 67. Spatially averaged ZDW values are in agreement with the measured global ZDW $<\lambda_0>$.

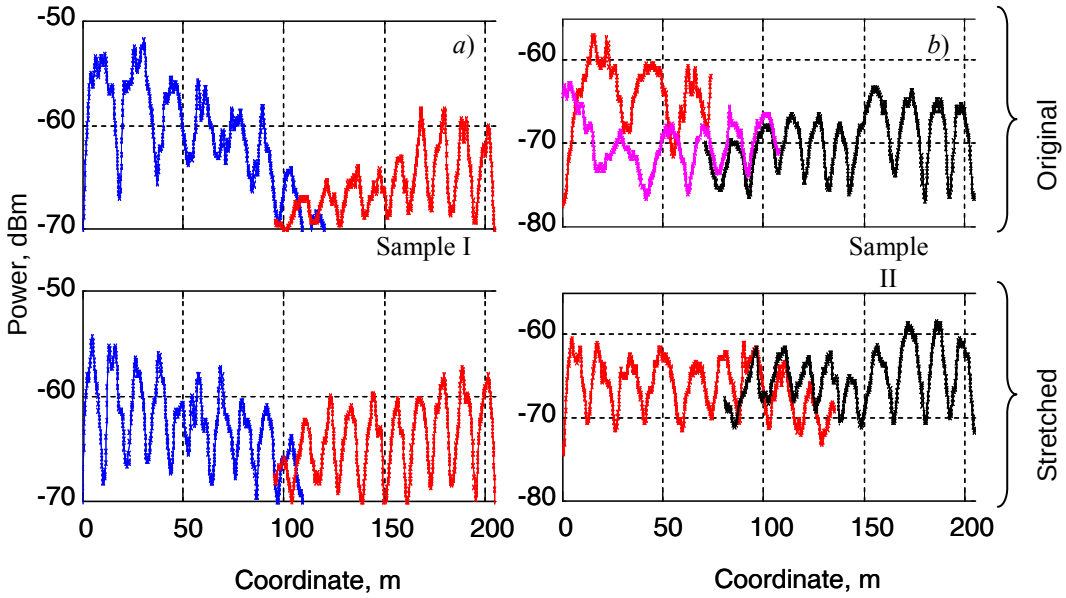

Fig. 66: Powers of the FWM product as a function of the collision coordinate: (upper) original fiber, (lower) stretched fiber. Scanning resolution was 20 cm. *a*) sample I, λ_{Probe}: 1540 nm, $\lambda_{Second\ Pulse}$: 1590 nm; *b*) sample II, λ_{Probe}: 1550 nm, $\lambda_{Second\ Pulse}$: 1600 nm.

In second step of the procedure, the tension-controlling block of a spooler was calibrated by measuring the global ZDW with the fiber stretched using an 80% of the maximal tension obtainable. Two fiber samples were subsequently divided into six and seven sections, correspondingly, with slowly-varying ZDW, and spooled by applying constant tension that is proportional to the difference between the local $\lambda_0(z)$ and maximum ZDW $\lambda_0^{(Max)}$, used as a target reference. The tension maps were subsequently validated using meter-scale resolution using the counter-colliding setup by searching the maximum SBS frequency clock position. The maximum obtained SBS frequency deviations were in excess of quadruple Brillouin linewidth in HNLF (~25 MHz), as shown in Fig. 68.

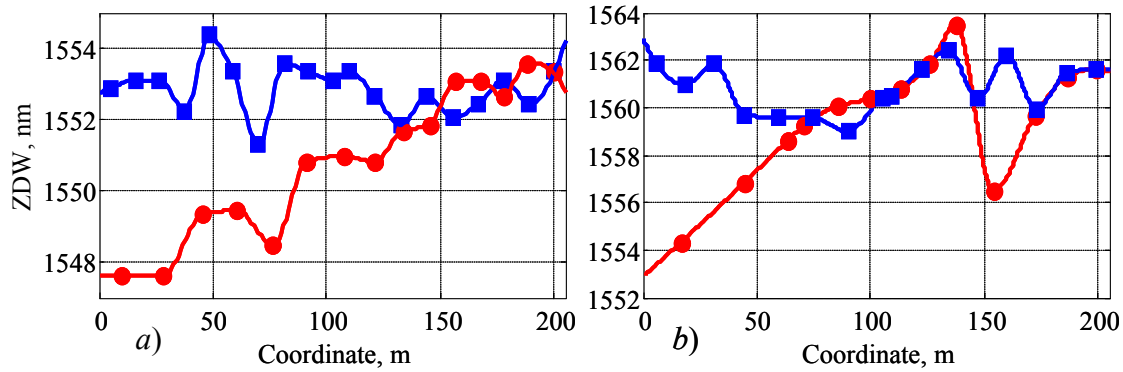

Fig. 67: Measured ZDW maps for the original and stretched sample I (*a*) and sample II (*b*): circle marks – before tension map application; square marks – after tension map application.

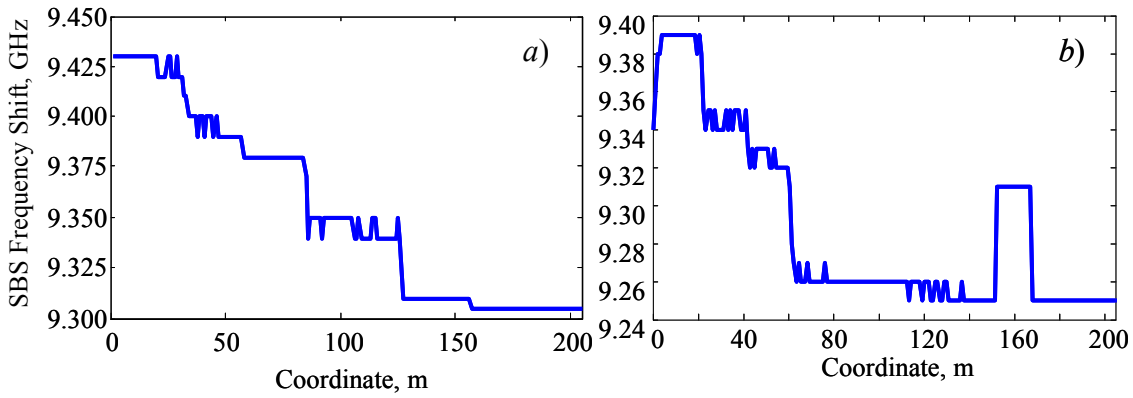

Fig. 68: Measured map of SBS frequency shift mapping tension strength of the sample I (*a*) and sample II (*b*). Scanning step: 1 m. SBS frequency searching step: 10 MHz.

The FWM power profiles of the fiber with applied tension map are shown in lower plots of Fig. 66. It is clearly seen that the oscillation periods corresponding to different sections were equalized across the fiber, indicating a drastic suppression of ZDW fluctuations. The corresponding (flattened) ZDW profile of the first sample centered at 1553 nm is depicted in Fig. 67 by blue square marks, showing a reduction in the ZDW fluctuations by more than 50%. For the second fiber, the resulting flattened ZDW profile was centered at 1561 nm and had peak-to-peak variations that were three times lower than those of the original sample.

Finally, the response of a one-pump parametric amplifier was measured to validate that the dispersion equalization technique resulting in superior mixer performance. A continuous-wave, 1.8 W pump was spectrally positioned to provide a double-sided gain profile with gain of 15 dB. Fig. 69 demonstrates that the 5-dB bandwidth of the amplifier constructed using dispersion equalized fiber was nearly doubled from 75 nm (before HNLF tensioning) to 140 nm (after tension map application). Of equal importance, the gain spectrum exhibited a more symmetrical response relative to the pump wavelength after stretching.

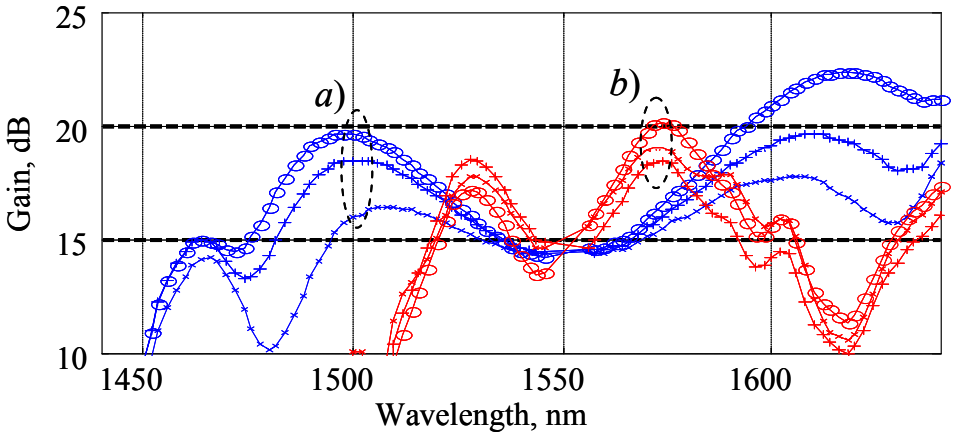

Fig. 69: Sample I: measured gain profiles for *a*) tension map applied and *b*) original HNLF. Pump positions were tuned to illustrate amplifier response for close-to-ZDW positioning: *a*) 1551.15, 1551.20, 1551.25 nm; *b*) 1549.95, 1550.00, 1550.05 nm.

It is important to note that, if the spatial dispersion profile of HNLF with wide ZDW fluctuation is equalized, the Brillouin effect should also be suppressed. From practical point of view, a simple strategy applicable to design requiring spatially flat dispersion and suppressed SBS calls for fiber with monotonically varying dispersion profile and *large* ZDW variations. In this case, the dependence of the applied tension will be a unique and easily inverted function guaranteeing that SBS center frequencies will not be repeated along the fiber and that the Brillouin process will not be seeded by

back-reflected light from other fiber sections. Finally, the modification of the fiber birefringence properties requires separate consideration and is not addressed.

7.4 Strict Localization of Nonlinear Interactions in Optical Fibers by Subsequent Brillouin Amplification and Attenuation

High spatial resolution can be naturally achieved if the nonlinear interaction responsible for the generation of the measured signal is gated locally along the waveguide. This principle was recently applied to the localization of four-photon mixing (FPM) to increase the spatial resolution of dispersive mapping of nearly dispersionless fiber [67]. In the aforementioned approach, the nonlinear interaction is excited at a certain point along the waveguide [4] and is maintained until its end, while the strength of the generated mixing products carries the information about the targeted waveguide section [67]. The longitudinal dispersion variation can be retrieved by sequentially scanning along the waveguide with the point of excitation [67]. Consequently, it is natural to generalize this method to a strict localization approach in which one would be able to abruptly increase and decrease the probe power entering and exiting the target waveguide section. In contrast to the previously reported technique [67], the new method would generate probe-probe mixing products that do not grow outside the target section, thus achieving a higher level of localization.

As has been demonstrated, efficient amplification of the probe in an HNLF-like waveguide can be accomplished with counter-colliding Brillouin pumps [67]. Using this implementation, the blue-shifted pump transfers energy to a weak probe to routinely generate more than 20 dB of optical gain during the pump-probe counter-collision

process. By introducing a red-shifted pump that attenuates the amplified optical probe at a precisely timed delay from the original (blue-shifted) collision, it should be possible, at least in principle, to generate highly localized probe power delivery at an arbitrary point in a waveguide. This letter reports this new localization concept. The abrupt amplification and attenuation process was studied theoretically and experimentally in order to derive its practical limits. We have found that a probe contrast in excess of 20 dB can be achieved by timed amplification and attenuation counter-collisions with Stokes and anti-Stokes Brillouin pumps in standard HNLF fiber.

Optical power localization can be implemented by sending two precisely timed pump pulses to counter-collide with the probe pulse at a designated point in a fiber: a blue-shifted pump is used to amplify, while a red-shifted pump is used to deplete (attenuate) the probe. Between the two counter-collision events, the amplified probe (or probes) possesses sufficient power to generate strong FPM mixing products, allowing indirect measurement of waveguide parameters, such as dispersion and the nonlinear coefficient, in a targeted section. The concatenated counter-collision localization principle is illustrated in Fig. 70.

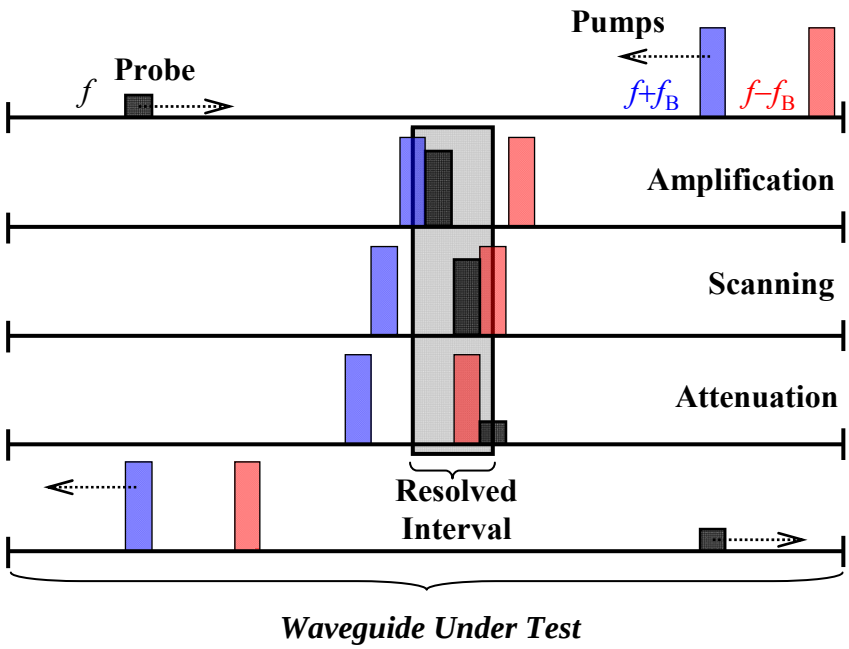

Fig. 70: A principle of spatial localization.

The narrow bandwidth nature of Brillouin amplification imposes a limitation on pump pulse frequencies and their relation to the counter-colliding probe: the probe-pump frequency separation must be controlled within a fraction of the Brillouin bandwidth. The Brillouin linewidth in most fibers of interest is only 25 MHz [67], thus limiting the characteristic time of the amplifying/attenuating event to several nanoseconds. Consequently, the pulse duration is limited by the same time scale, imposing strict limits on inter-pulse timing for the Stokes and anti-Stokes pumps.

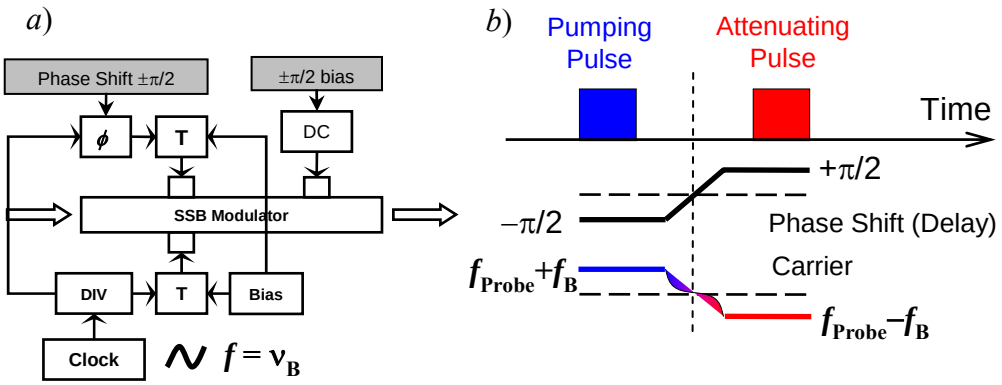

Fig. 71: Subsequent generation of amplifying and attenuating Brillouin pump pulse.

The optical carriers for the probe and the pump wave can be created using a single laser and an optical modulator driven by a harmonic excitation at the Brillouin natural frequency ($f_B \sim 9.3$ GHz) [67]. A null-point-biased amplitude modulator followed by a suppression filter, or, alternatively, a single sideband modulator (SSBM) can be used [67] for this purpose. A single SSBM (rather than using two AM modulators) can generate both the pumping and the de-pumping pulses by controlling the sign of the frequency shift applied to the pump pulse, as illustrated in Fig. 71. In practical terms, this can be accomplished by introducing a π-phase shift to the clock signal applied to the SSBM. Otherwise, the pump can be frequency shifted from f_B to $-f_B$ simply by changing the bias level controlling the phase shift between the two sub Mach-Zehnder interferometers of the SSBM. Measured spectra of the modulated signals corresponding to ±π/2 phase shift are shown in Fig. 72, indicating nearly ideal generation of Stokes and anti-Stokes waves.

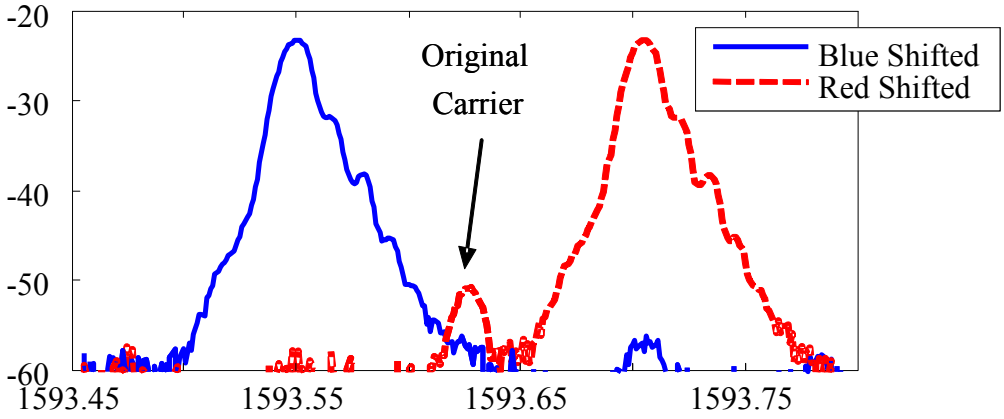

Fig. 72: Amplifying and attenuating pulses' spectra after the SSB modulator, corresponding to $\pm\pi/2$ phase shift.

A set of conventional HNLF segments was tested in order to determine the upper pump level that can be used in the FPM localization scheme. Pump pulses with peak power in excess of 10 W were depleted in HNLF segments longer than 300 m, primarily by spontaneous Raman scattering. The depletion mechanism effectively sets a practical limit that couples pump peak power and the maximum scanned waveguide length. Consequently, longer HNLF sections require lower pump peak powers.

The concatenated collision process was rigorously modeled by a set of scalar Brillouin equations (4.31) describing the evolution of the complex amplitude of the density variation and that of the counter-propagating probe pulse and pump. The model used the following set of parameters: $\alpha = 0.9$ dB/km for fiber attenuation coefficient, $\Delta f_B = 25$ MHz for a SBS gain spectrum full width half maximum (FWHM) width, $A_{eff} = 12$ um^2 for fiber effective area, γ_e electrostrictive constant of 0.902 for silica, ρ_0 material density of 2210 kg/m^3 and $v_A = 5960$ m/s for velocity of the acoustic wave [47].

The simplified experimental setup shown in Fig. 13 was used to demonstrate the proposed concept and to test the validity of the model. A branch generating a second

pulse was switched off. The carrier was shifted by shifting a phase of the clock driving one branch of the SSB modulator by π. Measured and simulated waveforms of the amplified and de-amplified probes are shown in Fig. 73 and Fig. 74. Typical measured gain exceeded 15 dB, and was higher for longer pulse durations. As mentioned in chapter 2.2, a long pulse trailing edge in Fig. 73 corresponds to a decaying refractive index grating whose lifetime is longer than the counter-collision event. The acoustic grating decay time was used to estimate the characteristic linewidth of the Brillouin interaction Δf_B, and agreed to within several MHz with the measured gain spectral width obtained using a heterodyne optical spectrum analyzer.

The attenuation of the probe pulse by the counter-colliding red-shifted pump is illustrated in Fig. 74. The optimal (temporally flat) probe attenuation corresponds to specific pump pulse duration of 6-8 ns; shorter pump duration corresponded to lower attenuation contrast. In the case when a long anti-Stokes pump pulse was used, the probe was well attenuated close to its leading edge, followed by pronounced ringing at its trailing edge.

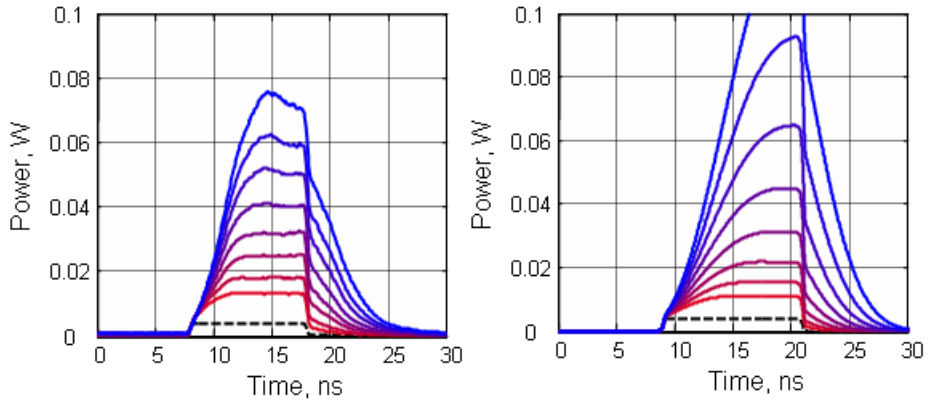

Fig. 73: Measured (left) and simulated (right) waveforms of the amplified 10-ns-probes for different pump pulse durations. The pump pulse length varied from 5 ns (red) to 12 ns (blue) with 1-ns step. Dotted line indicates unamplified probe.

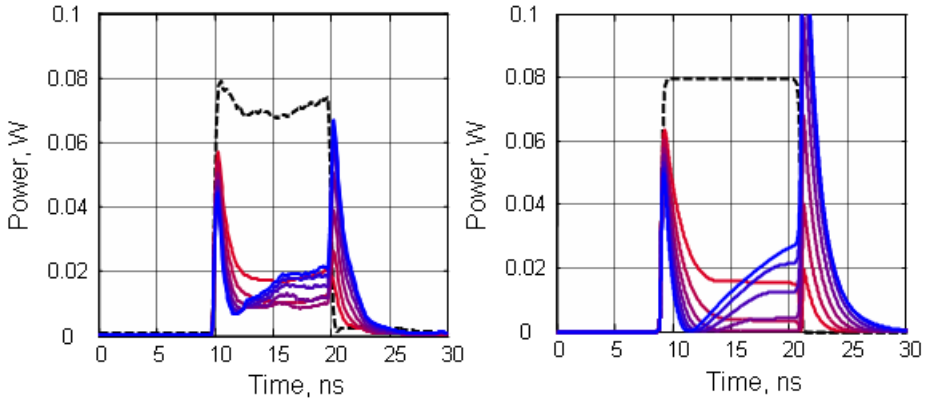

Fig. 74: Measured (left) and simulated (right) waveforms of the attenuated 10ns-probes for different pump pulse durations. The pump pulse length varied from 4 ns (red) to 10 ns (blue) with 1-ns step.

The effect of the pump depletion by the strong probe was investigated numerically by increasing the probe power up to 10 dBm. As seen from the contour plot shown in Fig. 75, the counter-colliding gain does not depend on probe power for the pump peak powers below 40 dBm.

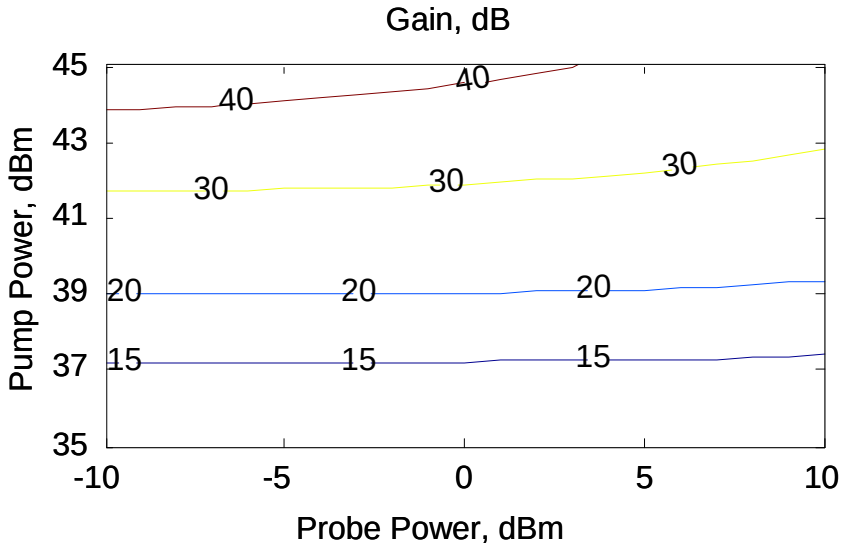

Fig. 75: The simulated map of the gain for 10 ns pulses as a function of probe and pump powers.

The deviation between the measured and simulated traces was attributed to linear intra-pulse polarization rotation. In standard HNLF, a complete polarization rotation

takes place within the interval of several meters and is comparable with the typical pulse duration. This implies that the polarization of the different parts, the counter-propagating probe and pump, are not precisely aligned in polarization, typically reducing the strength of nonlinear interactions by 50%.

The ratio between the probe gain and its attenuation after consecutive blue- and red-shifted counter-collisions was dependent on the probe peak power. This ratio, plotted in Fig. 76 for two different pump pulse durations, qualitatively defines the power localization of the probe. In the case when the attenuating pulse duration is not optimized (Fig. 76*a*), the area of high localization (i.e. the 0-dB contour in Fig. 76) corresponds to pump powers below 36 dBm and low gain ~10 dB (Fig. 75), resulting in insufficiently high FPM levels. For the optimized 6 ns pulse duration (Fig. 76*b*), the area of efficient de-pumping corresponds to gain values in excess of 20 dB.

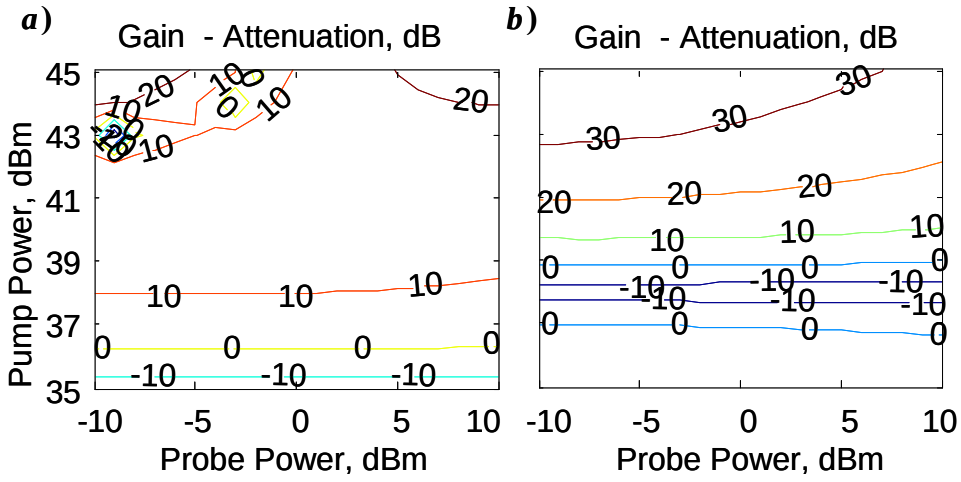

Fig. 76: Simulated map of the gain and attenuation difference in decibel scale for different probe and pump peak powers: *a*) both amplifying and de-amplifying pump pulses are 10 ns; *b*) 10 ns-amplifying pulse and 6-ns de-amplifying pulse. Probe duration is 10 ns in both cases.

8. Conclusions and Future Directions

Last decade, significant attenuation has been paid to fiber-based parametric technology utilizing highly nonlinear fibers as a nonlinear media. Unfortunately, all efforts were not converted to the introduction of effective CW parametric devices available in telecom market. Present activities are still remained in laboratory stage. Originally, the main limiting factor was the objective difficulty to fabricate continuous fiber segments longer than 500 m with constant longitudinal dispersion characteristics and absence of the compact CW high-power (<25 dBm) low-noise lasers. For example, the typical fibers manufactured ten year ago had fluctuations of ZDW up to several nanometers per 100-m length. Current fabrication technology is capable of suppressing these fluctuations below a nanometer. Further improvement of the fabrication tolerance is questionable because of extreme sensitivity of the fiber dispersion characteristics to geometry, requiring unphysical molecular scale geometry control. The efficiency of the nonlinear process is defined by a product of pump power P and effective fiber length L. This means that, for a given power pump, the only way to increase conversion efficiency is to use longer fibers. However, long fibers have second serious drawback – the requirement to suppress parasitic stimulated Brillouin scattering (SBS) depleting pump powers. In laboratories, the suppression can be implemented by placing a phase

modulator broadening the pump spectrum before a booster. Booster necessarily adds broadband noise which has to be blocked before launching pump to a fiber. In addition, the pump phase deviations are mapped directly to the phases of the converted/amplified signals inducing distortions. Such implementation is not acceptable in commercial product dictating different means for (i) the *PL*-product increase and (ii) for the SBS suppression.

The introduced method of the counter collided pulses provides a tool for ZDW characterization to separate fiber segments with low ZDW deviations. These fiber segments can be concatenated using some algorithm optimizing the parametric response. This algorithm requires special consideration and is not a part of this thesis. Even if ZDWs of the separate pieces do not match, they can be equalized using the stretching technique introduced in section 7.3. The experiment showed that the parametric converter shorter than 100 m does not require phase dithering to suppress SBS. If the centers of the SBS gain profiles of the segments do not match, the converter created using short spliced pieces will not require phase dithering as well. This requirement can be partially (or fully) fulfilled because the stretching induces the shift in SBS profile. The obvious generalization of the method is the concatenation of dissimilar samples providing equalized parametric response.

The following improvements in dispersion measuring setup can be considered:

1. The first improvement is referred to a detection scheme. The high spatial resolution requires more than 50 nm the wavelength separation $\Delta\lambda$ between probe and second pulse. However, the nonlinear efficiency drops as squared *sinc*-function with $\Delta\lambda$. The power of the pulses has to be increased in order to be well above the shot-noise

limit. At the same time, high pulse powers dictate the presence of other nonlinear effects, including nonlinear polarization rotation, adding spurious extrema in the processed FPM power trace. Potential candidate for such low noise receiver is an extremely narrow (several GHz) tunable filter followed by a power meter or by lock-in amplifier with dynamically tuned gain.

2. The polarization behavior of the propagating pulses in a fiber needs more investigation. In last realization shown in Fig. 54, a single polarization scrambler randomizes polarization states *a*) of *probe and pump* so that the slow receiver sees only some FWM power averaged over all polarization states; and of *b*) *probe and second pulse* to eliminate effect of linear PMD. Besides linear rotation, there two other mechanisms modifying pulse polarization: SPM-induced self-rotation and polarization-dependent XPM. A simple estimation of the rotation angle induced in 500-m sample by a 500-mW pulse gives $1/6\gamma PL \approx 50°$. The nonlinear PMD correlates polarization states of the co-propagating pumps preventing full polarization randomization.
3. A block forming pulses requires some improvements as well. This block can be made polarization-maintaining to avoid fine polarization alignment before every measurement. The contrast of the measurement degrades significantly (see section 3.5) if the bias of a modulator forming a pump pulse drifts for more than 0.05 V. There are two reasons explaining such behavior. First, the pulses are amplified by EDFA. In a pulsed mode, EDFAs behave as power-clamped amplifier reacting to the average input power. If the bias drifts, the peak pump power degrades because of a low repetition rate, together with the SBS gain. The second reason is

that the pump pulse pedestal starts amplifying pulses. These arguments dictate that the bias has to be dynamically controlled throughout the measurement.

The proposed technique was conformed by measuring HNLF dispersion map with meter-scale resolution for the first time. Such resolution is at least one or two orders higher than that obtained using any existing schemes described in section 1.2. The setup was assembled using standard components provided by telecom manufacturers and does not contain any signal sources and filters tuned in wavelength so that the process can be fully automated, making a scheme potentially attractive for commercial applications.

The concept of the localized FPM by discrete power delivery can be applied to diversified set of new measurement techniques for other nonlinear platforms.

References

1. S. Radic, C.J. McKinstrie, R.M. Jopson, J.C. Centanni, Q. Lin, G.P. Agrawal, "Record performance of a parametric amplifier constructed with highly-nonlinear fiber," Electronic Letters, Vol. 39, pp. 838–839, 2003.

2. S. Radic, C.J. McKinstrie, "Optical Amplification and Signal Processing in Highly Nonlinear Optical Fiber", IEICE Transactions on Electronics, Vol. 5, pp. 859–869, 2005.

3. C.J. McKinstrie, S. Radic, A.R. Chraplyvy, "Parametric amplifiers driven by two pump waves", IEEE Journal of Selected Topics in Quantum Electronics, Vol. 8, No. 3, pp. 538–547, 2002.

4. G.P. Agrawal, "Record performance of parametric amplifier constructed with highly nonlinear fibre", Electronics Letters, Vol. 39, No. 11, pp. 838–839, 2003.

5. T. Torounidis, P.A. Andrekson, B.-E. Olsson, "Fiber-optical parametric amplifier with 70-dB gain", IEEE Photonics Technology Letters, Vol. 18, No. 10, pp. 1194–1196, 2006.

6. K.K.Y. Wong, K. Shimizu, K. Uesaka, G. Kalogerakis, M.E. Marhic, L.G. Kazovsky, "Continuous-wave fiber optical parametric amplifier with 60-dB gain using a novel two-segment design", IEEE Photonics Technology Letters, Vol. 15, No. 12, pp. 1707–1709, 2003.

7. J. Hansryd, P.A. Andrekson, M. Westlund, J. Li, P.O. Hedekvist, "Fiber-based optical parametric amplifiers and their applications," IEEE J. Sel. Top. Quantum Electronics, Vol. 8, No. 3, pp. 506–520, 2002.

8. M.-Ch. Ho, K. Uesaka, M. Marhic, Y. Akasaka, L.G. Kazovsky, "200-nm-bandwidth fiber optical amplifier combining parametric and Raman gain", Journal of Lightwave Technology, Vol. 19, No. 7, pp. 977–981, 2001.

9. J.M. Boggio, S. Moro, E. Myslivets, J.R. Windmiller, N. Alic, S. Radic, "155-nm Continuous-Wave Two-Pump Parametric Amplification", IEEE Photonics Technology Letters, Vol. 21, No. 10, pp. 612–614, 2009.

10. C.-S. Bres, N. Alic, E. Myslivets, S. Radic, “1-to-40 Multicasting and Amplification of 40Gbps Channels in Wideband Parametric Amplifier”, Postdeadline Paper, OFC 2008.

11. S. Radic, R.M. Jopson, C.J. McKinstrie, A.H. Gnauck, S. Chandrasekhar, J.C. Centanni, “Wavelength division multiplexed transmission over standard single mode fiber using polarization insensitive signal conjugation in highly nonlinear optical fiber,” post deadline paper, OFC 2003, PD12, Atlanta USA 2003.

12. N. Alic, E. Myslivets, S. Moro, B.P.-P. Kuo, R.M. Jopson, C.J. McKinstrie, S. Radic, “1.83-μs wavelength-transparent all-optical delay”, OFC 2009, post deadline paper, pp. 1–3.

13. S. Namiki, “Wide-Band and -Range Tunable Dispersion Compensation through Parametric Wavelength Conversion and Dispersive Optical Fibers,” Journal of Lightwave Technology, Vol. 26, No. 1, pp. 28–35, 2008.

14. S. Namiki, T. Kurosu, “17 ns tunable delay for picosecond pulses through simultaneous and independent control of delay and dispersion using cascaded parametric process,” post deadline paper, ECOC 2008, Th. 3, C.3, Brussels Belgium 2008.

15. E. Myslivets, N. Alic, S. Moro, B.P.P Kuo, R.M. Jopson, C.J. McKinstrie, M. Karlsson, S. Radic, “1.56-μs continuously tunable parametric delay line for a 40-Gb/s signal”, Optics Express, Vol. 17, No. 14, pp. 11958–11964, 2009.

16. C.-S. Brès, A. Wiberg, J.B. Coles, S. Radic, “160-Gb/s optical time division multiplexing and multicasting in parametric amplifiers”, Optics Express, Vol. 16, No. 21, pp. 16609–16615, 2008.

17. M. Westlund, P.A. Andrekson, H. Sunnerud, J. Hansryd, J. Li, “High-performance optical-fiber-nonlinearity-based optical waveform monitoring”, Journal of Lightwave Technology, Vol. 23, No. 6, pp. 2012–2022, 2005.

18. P.A. Andrekson, “High resolution optical waveform sampling”, IEEE/LEOS Winter Topical Meeting Series, pp. 187–188, 2009.

19. G.C. Valley, “Photonic analog-to-digital converters”, Optics Express, Vol. 15, No. 5, pp. 1955–1982, 2007.

20. P.L. Voss, R. Tang, P. Kumar, “Measurement of the photon statistics and the noise figure of a fiber-optic parametric amplifier” Optics Letters, Vol. 28, No. 7, pp. 549–551, 2003.

21. M. Marhic, “Fiber Optical Parametric Amplifiers, Oscillators and Related Devices”, Cambridge University Press, 2007.

22. T. Okuno, T. Nakanishi, M. Hirano, and M. Onishi, “Practical Considerations for the Application of Highly Nonlinear Fibers”, Optical Fiber Conference, Paper OTuJ1, 2006.

23. T. Nakanishi, M. Hirano, T. Okuno, M. Onishi, “Silica-based highly nonlinear fiber with $\gamma = 30$ /W/km and its FWM-based conversion efficiency”, Optical Fiber Communication conference, OFC 2006, OTuH7.

24. M. Hirano, T. Nakanishi, T. Okuno, M. Onishi, “Silica-Based Highly Nonlinear Fibers and Their Application”, IEEE Journal of Selected Topics in Quantum Electronics, Vol. 15, No. 1, pp. 103–113, 2009.

25. M. Onishi, T. Okuno, T. Kashiwada, S. Ishikawa, N. Akasaka, M. Nishimura, “Highly Nonlinear Dispersion-Shifted Fibers and Their Application to Broadband Wavelength Converter”, Optical Fiber Technology, No. 4, pp. 204–214, Article No. OF980248, 1998.

26. D. Cotter, “Ultrafast Phenomena V”, Springer Series in Chemical Physics, Springer, January 1987.

27. Corning Single-Mode Optical Fiber, SMF-28 fiber, product information. http://www.corning.com/opticalfiber.

28. M. Karlsson, “Four wave mixing in fibers with randomly varying zero-dispersion wavelength”, J. Opt. Soc. Amer. B, Vol. 15, pp. 2269–2275, 1998.

29. M. Farahmand, M. de Sterke, "Parametric amplification in presence of dispersion fluctuations," Opt. Express, Vol. 12, pp. 136–142, 2004.

30. F. Yaman, Q. Lin, S. Radic, G.P. Agrawal, “Impact of dispersion fluctuations on dual-pump fiber-optic parametric amplifiers”, IEEE Photonics Technology Letters, Vol. 16, No. 5, pp. 1292–1294, 2004.

31. D. Derickson, Fiber Optics. Test and Measurement, Prentice Hall, 1998.

32. J. Gripp, L.F. Mollenauer, "Enhanced range for OTDR-like dispersion map measurements", Optics Letters, Vol. 23, No. 20, 1998.

33. J. Gripp, L. Mollenauer, “Dispersion-map measurements of optical fibers”, US Patent 6067149, May 23, 2000.

34. L.F. Mollenauer, P.V. Mamyshev, M.J. Neubelt, “Method for facile and accurate measurement of optical fiber”, Optics Letters, Vol. 21, No. 21, 1996.

35. I. Brener, P.P. Mitra, D.J. Thomson, "High-resolution zero-dispersion wavelength fluctuation mapping in dispersion-shifted fiber", OFC 1998, ThR5, 1998.

36. I.M. Brener, D.J. Thomson, P.P. Mitra, D.D. Lee, D.L. Philen, “High-resolution zero-dispersion wavelength mapping in single mode fiber”, US Patent 6118523, 2000.

37. M. Eiselt, R.M. Jopson, R.H. Stolen, “Nondestructive Position-Resolved Measurement of the Zero-Dispersion Wavelength in an Optical Fiber”, Journal of Lightwave Technology, Vol. 15, No. 1, 1997.

38. M. González-Herráez, P. Corredera, M.L. Hernanz, J.A. Méndez, "Retrieval of the zero-dispersion wavelength map of an optical fiber from measurement of its continuous-wave four-wave mixing efficiency," Optics Letters, Vol. 27, pp. 1546–1548, 2002.

39. A. Mussot, E. Lantz, A. Durecu-Legrand, C. Simonneau, D. Bayart, T. Sylvestre, H. Maillotte, “Zero-dispersion wavelength mapping in short single-mode optical fibers using parametric amplification”, IEEE Photonics Technology Letters, Vol. 18, No. 1, pp. 22–24, 2006.

40. K. Inoue, “Four-wave mixing in an optical fiber in the zero-dispersion wavelength region”, Journal of Lightwave Technology, Vol. 10, No. 11, pp. 1553–1561, 1992.

41. M.N. Islam, “Raman Amplifiers for Telecommunications”, IEEE Journal of Quantum Electronics, Vol. 8, No. 3, pp. 548–559, 2002.

42. R.G. Smith "Optical Power Handling Capacity of Low Loss Optical Fibers as Determined by Stimulated Raman and Brillouin Scattering", Applied Optics, Vol. 11, No. 11, pp. 2489–2494, 1972.

43. N.R. Newbury, “Pump-wavelength dependence of Raman gain,” OAA 2002, OME9.

44. R.H. Stolen, E.P. Ippen, “Raman gain in glass optical waveguides”, Appl. Phys. Lett., Vol. 22, No. 6, pp. 276–278, 1973.

45. R.H. Stolen, J.P. Gordon, W.J. Tomlinson, H.A. Haus, “Raman response function of silica-core fibers”, J. Opt. Soc. Am. B, Vol. 6, pp. 1159–1166, 1989.

46. N. Bloembergen, “Nonlinear Optics”, World Scientific Publishing; 4th ed., 1996.

47. H. Li, K. Ogusu, "Dynamic Behavior of Stimulated Brillouin Scattering in a Single-Mode Optical Fiber", Jpn. J. Appl. Phys. Vol. 38, pp. 6309–6315, 1999.

48. M. Nikles, L. Thevenaz, P.A. Robert, "Brillouin gain spectrum characterization in single-mode optical fibers", IEEE Journal of Lightwave Technology, Vol. 15, No. 10, pp. 1842–1851, 1997.

49. A. Djupsjöbacka, G. Jacobsen, B. Tromborg, "Dynamic stimulated Brillouin scattering analysis”, Journal of Lightwave Technology, Vol. 18, No. 3, 2000.

50. J.M. Chávez Boggio, H.L. Fragnito, "Simple four-wave-mixing-based method for measuring the ratio between the third- and fourth-order dispersion in optical fibers", J. Opt. Soc. Am. B, Vol. 24, No. 9, pp. 2046–2054, 2007.

51. Y.J. Wen, A. Nirmalathas, D.-S. Lee, “RZ/CSRZ-DPSK and chirped NRZ signal generation using a single-stage dual-electrode Mach-Zehnder modulator”, Vol. 16, No. 11, pp. 2466–2468, 2004.

52. http://www.photonicsinc.com/pdfs/PSI-0303.pdf.

53. A.W. Snyder, J. Love, Optical Waveguide Theory, Springer, 1983.

54. S.A. Akhmanov, V.A. Vysloukh, A.S. Chirkin, “Optics of Femtosecond Laser Pulses”, American Institute of Physics; 1st ed., 1991.

55. G.P. Agrawal, “Nonlinear Fiber Optics”, 3rd ed. Academic Press, 2001.

56. R.W. Boyd, “Nonlinear Optics”, Chapter 13, 3rd ed. Academic Press; 2008.

57. K. Iizuka, “Elements of Photonics”, Vol. 2, Chapter 15, Wiley-Interscience; 1st edition, 2002.

58. K. Inoue, “Four-wave mixing in an optical fiber in the zero-dispersion wavelength region”, IEEE Journal of Lightwave Technology, Vol. 10, No. 11, pp. 1553–1561, 1992.

59. K.J. Blow, D. Wood, “Theoretical description of transient stimulated Raman scattering in optical fibers”, IEEE Journal of Quantum Electronics, Vol. 25, No. 12, pp. 2665–2673, 1989.

60. C. Headley III, G.P. Agrawal, “Noise characteristics and statistics of picosecond Stokes pulses generated in optical fibers through stimulated Raman scattering”, IEEE Journal of Quantum Electronics, Vol. 31, No. 11, 2058–2067, 1995.

61. VPI Photonics documentation, manual for UniversalFiber module.

62. G. Bosco, A. Carena, V. Curri, R. Gaudino, P. Poggiolini, S. Benedetto, “Suppression of spurious tones induced by the split-step method in fiber systems simulation”, IEEE Photonics Technology Letters, Vol. 12, No. 5, 489–491, 2000.

63. R. Stolen, J. Bjorkholm, “Parametric amplification and frequency conversion in optical fibers”, IEEE Journal of Quantum Electronics, Vol. 18, No. 7, pp. 1062–1072, 1982.

64. E. Hairer, C. Lubich, M. Roche, “The Numerical Solution of Differential-Algebraic Systems by Runge-Kutta Methods”, (Lecture Notes in Mathematics), Springer; 1st ed. 2009.

65. S.J. Farlow “Partial Differential Equations for Scientists and Engineers (Dover Books on Advanced Mathematics)”, Dover Publications, 1993.

66. H. Kogelnik, R.M. Jopson, Optical Fiber Telecommunications IV-B, Chapter 15, Academic Press, 2002.

67. E. Myslivets, N. Alic, J.R. Windmiller, S. Radic, "A New Class of High-Resolution Measurements of Arbitrary-Dispersion Fibers: Localization of Four-Photon Mixing Process", Journal of Lightwave Technology, Vol. 27, pp. 364–375, 2009.

68. R. Stolen, “Polarization effects in fiber Raman and Brillouin lasers”, IEEE Journal of Quantum Electronics, Vol. 15, No. 10, pp. 1157–1160, 1979.

69. ITU-T Recommendation G.650, “Definition and test methods for the relevant parameters of single-mode fibres”.

70. A. Zadok, E. Zilka, A. Eyal, L. Thévenaz, M. Tur, “Vector analysis of stimulated Brillouin scattering amplification in standard single-mode fibers”, Optics Express, Vol. 16, No. 26, pp. 21692–21707, 2008.

71. M.E. Froggatt, D.K. Gifford, S. Kreger, M. Wolfe, B.J. Soller, “Characterization of Polarization-Maintaining Fiber Using High-Sensitivity Optical-Frequency-Domain Reflectometry”, Journal of Lightwave Technology, Vol. 24, No. 11, pp. 4149–4154, 2006.

72. W.H. Press, S.A. Teukolsky, W.T. Vetterling, B.P. Flannery, “Numerical Recipes in C+”, Chapter 11.3, Cambridge University Press, 2002.

73. W.H. Press, S.A. Teukolsky, W.T. Vetterling, B.P. Flannery, “Numerical Recipes in C+”, Chapter 11.7, Cambridge University Press, 2002.

74. J.H. Wilkinson, C. Reinsch, “Handbook for Automatic Computation”, Volume II, Linear Algebra, Part 2, Springer Verlag, 1971. Implemented in FIGI2 function in EISPACK library.

75. J. Nocedal, S. Wright, “Numerical Optimization”, Springer 2006.

76. W.H. Press, S.A. Teukolsky, W.T. Vetterling, B.P. Flannery, “Numerical Recipes in C+”, Chapter 10.4, Cambridge University Press, 2002.

77. W.H. Press, S.A. Teukolsky, W.T. Vetterling, B.P. Flannery, “Numerical Recipes in C+”, Chapter 10.5, Cambridge University Press, 2002.

78. W.H. Press, S.A. Teukolsky, W.T. Vetterling, B.P. Flannery, “Numerical Recipes in C+”, Chapter 10.6, Cambridge University Press, 2002.

79. J. Nocedal, S. Wright, “Numerical Optimization”, Springer, 2006.

80. A. Boskovic, S.V. Chernikov, J.R. Taylor, L. Gruner-Nielsen, O.A. Levring, “Direct Continuous-wave measurement of n2 in various types of telecommunication fiber at 1.55 mm”, Optics Letters, Vol. 21, No. 24, pp. 1966–1968, 1996.

81. C. Vinegoni, M. Wegmuller, N. Gisin, “Determination of nonlinear coefficient n2/Aeff using self-aligned interferometer and Faraday mirror”, Electronic Letters, Vol. 36, No. 10, pp. 886–888, 2000.

82. R. Engelbrecht, M. Mueller, B. Schmauss, “SBS shaping and suppression by arbitrary strain distributions realized by a fiber coiling machine”, IEEE/LEOS Winter Topical Meeting, WC1.3, pp. 248−249, 2009.

83. T. Horiguchi, T. Kurashima, M. Tateda, “A technique to measure distributed strain in optical fibers”, IEEE Photonics Technology Letters, Vol. 2, No. 5, pp. 352−354, 1990.

84. X. Bao, D.J. Webb, D.A. Jackson, “32-km distributed temperature sensor based on Brillouin loss in an optical fiber”, Optics Letters, Vol. 18, No 18, pp. 1561−1563, 1993.

85. M. Nikles, L. Thevenaz, P.A. Robert, “Simple distributed fiber sensor based on Brillouin gain spectrum analysis”, Optics Letters, Vol. 21, No. 10, pp. 758−760, 1996.

86. K.C. Byron, M.A. Bedgood, A. Finey, C. McGauran, S. Savory, I. Watson, ”Shifts in zero dispersion wavelength due to pressure, temperature and strain in dispersion shifted single mode fibres”, Electronics Letters, Vol. 28, No. 18, pp. 1712−1714, 1992.

87. E. Lichtman, R.G. Waarts, A.A. Friesem, “Stimulated Brillouin scattering excited by a modulated pump wave in single-mode fibers,” Journal of Lightwave Technology, Vol. 7, No. 1, pp. 171−174, 1989.

88. Y. Aoki, K. Tajima, I. Mito, “Input power limits of single-mode optical fibers due to stimulated Brillouin scattering in optical communication systems”, Journal of Lightwave Technology, Vol. 6, No. 5, 710−719, 1988.

89. Showmark, LLC, http://www.showmarkcorp.com /standard.html.

90. S. Korotky, “Multifrequency lightwave source using phase modulation for suppressing stimulated Brillouin scattering in optical fibers”, US Pattent 5566381, October 15, 1996.

91. S. Korotky, P.B. Hansen, L. Eskildsen, J.J. Veselka, “Efficient Phase Modulation Scheme for Suppressing Stimulated Brillouin Scattering”, Tech. Dig. Int. Conf. Integrated Optics and Optical Fiber Comm., Vol. 1, WD2-1, pp. 110–111, Hong Kong, 1995.